Study of Nanowires Using Molecular Dynamics Simulations

by
Joshua D. Monk

Dissertation submitted to the faculty of the
Virginia Polytechnic Institute and State University
In partial fulfillment of the requirements for the degree of

Doctor of Philosophy
In
Materials Science & Engineering

Dr. Diana Farkas, Chairman

Dr. Yu Wang
Dr. Stephen Kampe
Dr. Ron Kriz
Dr. Bill Reynolds

November 1st, 2007
Blacksburg, Virginia

Keywords: Nanowires, Molecular Dynamics, Grain Growth, Nickel, Silver, Tension-Compression Asymmetry, LAMMPS.

Study of Nanowires using Molecular dynamics Simulations

By
Joshua D. Monk

ABSTRACT

In this dissertation I present computational studies that focus on the unique characteristics of metallic nanowires. We generated virtual nanowires of nanocrystalline nickel (nc-Ni) and single crystalline silver (Ag) in order to investigate particular nanoscale effects. Three-dimensional atomistic molecular dynamics studies were performed for each sample using the super computer System X located at Virginia Tech. Thermal grain growth simulations were performed on 4 nm grain size nc-Ni by observing grain sizes over time for temperatures from 800K to 1450K and we discovered grain growth to be linearly time-dependant, contrary to coarse grained materials with square root dependence. Strain induced grain growth studies consisted of straining the nanostructures in tension at a strain rate of 3.3×10^8 s^{-1}. Grain boundary movement was recorded to quantify grain boundary velocities and grain growth. It was shown that during deformation, there is interplay between dislocation-mediated plasticity and grain boundary accommodation of plasticity through grain boundary sliding. To further understand the effect of stress on nanocrystalline materials we performed tensile tests at different strain rates, varying from 2.22×10^7 s^{-1} to 1.33×10^9 s^{-1} for a 5 nm grain size nc-Ni nanowire with a 5 nm radius. The activation volume was given as $\sim 2b^3$, where b is the Burger's vector and is consistent with a grain boundary dominate deformation mechanism. We expanded our research to 10 nm grain size nc-Ni nanowires with radii from 5 nm to 18 nm. Each wire was deformed 15% in tension or compression at a strain rate of 3.3×10^8 s^{-1}. Asymmetry was observed for all radii, in which larger radii produced higher flow stresses for compression and small radii yielded higher flow stresses in tension. A cross over in the tension-compression asymmetry is found to occur at a radius of ~9 nm. A change in the dominate deformation mechanism in combination with the ease of grain boundary sliding contributes to the phenomena of the asymmetry. In the final chapter we focus on the energetic stability of multi-twinned Ag nanorods at the nanoscale. We used a combination of molecular statics and dynamics to find the local minimum energies for the multi-twinned nanorods and the non-twinned "bulk" materials and concluded that the stability of multi-twinned nanorods is highly influenced by the size of the sample and the existence of the ends. Using an analytical model we found the excess energy of the nanorods with ends and determined the critical aspect ratio below which five-twinned nanorods are stable.

Acknowledgements

I would like to thank the following people for their help and support during my work on this dissertation:

- My advisor Dr. Diana Farkas for allowing me the opportunity to study at Virginia Tech as well as her guidance and patience through these four years. I thank her sharing her knowledge of in material science and life. Her experience as a leader in our field has given me some many occasions to work with other forward thinking scientist and these experiences will be remembered always.

- Dr. Brian Hyde for showing me the ropes when I first arrived and introducing me to the Materials Science Happy Hour group.

- Dr. Douglas Crowson for always being there for questioning about anything and everything.

- Som Mohanty for staying at Virginia Tech to get his masters and introducing life and entertainment to the computational materials science group. I.e ... me.

- Dr. Ben Poquette for his unending knowledge of material science and engineering topics and advice.

- Dr. Stephen Kampe, Dr. Yu Wang, Dr. Ron Kriz, and Dr. Bill Reynolds for taking the time to be on my committee and giving me positive feedback on my qualifier and preliminary exams.

- Dr. Jeff Hoyt , Dr. Eduardo Bring and Dr. Alfredo Caro for their amazing insight in computational material science and for being good role models as material scientist as I joined them at their respective national labs.

- Steve Plimpton for writing such a complete Molecular Dynamic code, LAMMPS, and the continual upkeep that goes along with it.

Thanks should be given to all of my friends I have found over the years past and present. Peege, Matt, Stacy, Mike, and Josh for coming to visit reminding me of home and family. To the hokies I have meet here, Ron, Brad, Graffam, Karen, Eric, Carly, Bartlett and everyone else thank you for making life at Virginia Tech something to remember and cherish.

I would especially like to thank my parents for their support and great genes. With out your love and belief in the Lord and me, I would never have gotten where I am today.

Finally I am happy to thank my love, Melissa, for giving me courage to excel and better myself. I thank you for your support and continual love through the hectic life of a graduate student and most importantly for giving the best advice “No Worries”.

Attribution

Several colleagues and coworkers aided in the writing and research behind several of the chapters of this dissertation. A brief description of their background and their contributions are included here.

Prof. Diana Farkas- Ph.D. (Department of Materials Science and Engineering, Virginia Tech) is the primary Advisor and Committee Chair. Prof. Farkas provided vital contributions and revisions to our publications that were turned into chapters 3, 4, 5, 6, and 7 in this dissertation.

Chapter 3: Linear Grain Growth Kinetics and Rotation in Nanocrystalline Ni **and**
Chapter 4: Driven Grain Boundary Motion in Nanocrystalline Material

Somadatta Mohanty - Masters. (Department of Materials Science and Engineering, Virginia Tech) currently at GE Corporation was a student in the author's group and contributed during his graduate studies to chapters 3 and 4 in terms of discussing fundamental ideas and large amounts of time and work.

Chapter 7: Meta-Stability of Multi-Twinned Ag Nanorods

Prof. Jeffrey Hoyt - Ph.D. (Department of Materials Science Engineering, McMasters University) currently a professor at McMaster University, was a mentor at Sandia National Laboratories, Albuquerque during the author's summer internship. His mentorship and editing aided the author in completing Chapter 7, which has been submitted for publication.

Table of Contents

List of Figures

List of Tables

CHAPTER 1: Introduction

Over the years as computational resources increase and experimental techniques improve it has become a goal for many scientists to bridge the gap between computational studies and experimental results. One research field that allows for collaborations between experimental and computational studies on the same length scale is nanotechnology. Through our research we hope to confirm observations found in experiments and build upon them. In this dissertation I discuss a number of molecular dynamics (MD) simulations completed while attending Virginia Tech under Dr. Diana Farkas' guidance. The multiprocessor softwares LAMMPS and PARADYN were used throughout these studies. These codes were provided by Plimpton et al. (www.lampes.sandia.gov) located at Sandia National Laboratory, New Mexico.

Figure 1.1 shown below exhibits various nanowire structures used in this study. In Figure 1.1 there are two nanocrystalline nickel (nc-Ni) nanowires (A,B) and a twinned and non-twinned silver (Ag) single crystal nanorods. The samples ranged in size from 1 nm to 60 nm lengths with one thousand to 2.5 million atoms. Nickel and silver were selected as the metals due to their large number of EAM potentials available for the multi-processor software LAMMPS and their familiar face-center cubic (FCC) crystalline structure, which has been studied in numerous MD simulations. Nc-Ni nanowires and silver nanorods are good materials for research because similar nanostructures have been grown experimentally allowing us to compare our simulated phenomenon with experiments.

The purpose of my research was to understand nanoscale effects for different metal nanowires and assist experimentalist in understanding the characteristics that are

difficult to observe in experimental studies. In particular we looked at nc-Ni and multi-twinned Ag nanowires and studied different nanoscale characteristics in order optimize the properties of the materials. Our studies concentrated on understanding the mechanisms and kinetics of grain growth, grain boundary mobility, grain rotation, boundary conditions, energetic stability, and deformation mechanisms present at the nanoscale.

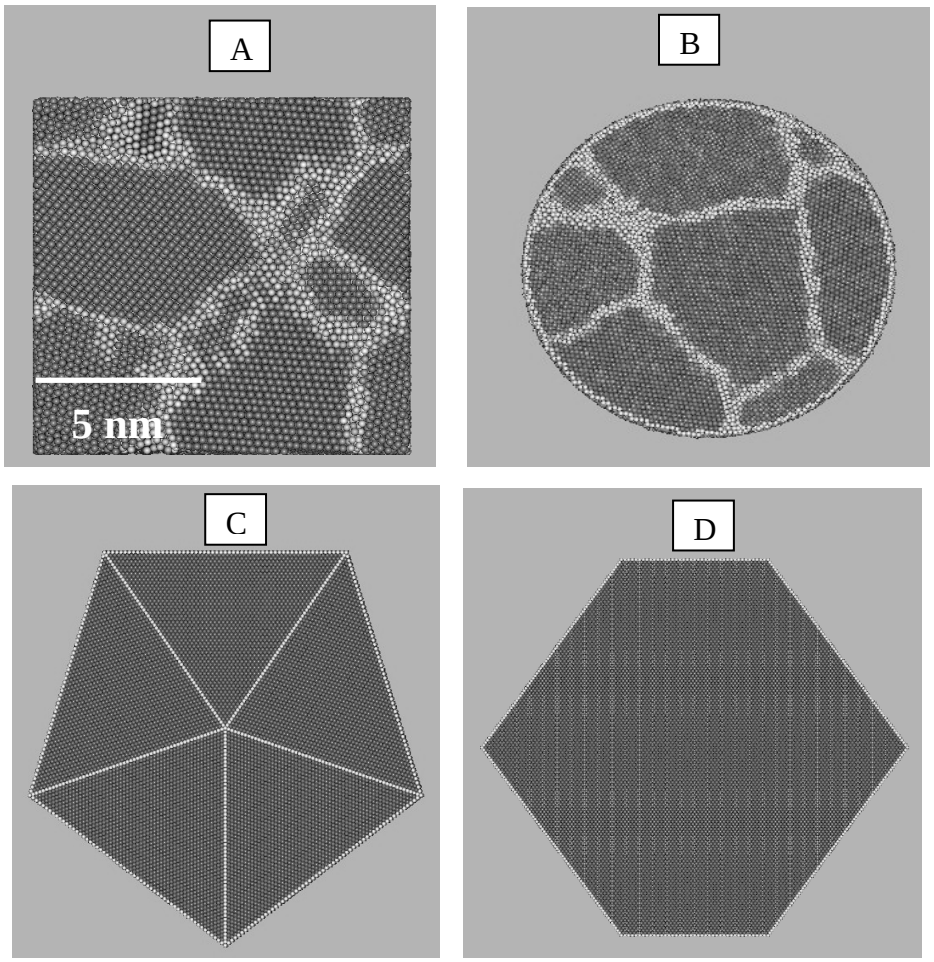

Fig. 1.1 Four nanowires structures, they are all periodic in the axial direction (into the paper). A,B) nickel and C,D) silver. Scale equivalent for all pictures.

CHAPTER 2: Background

2.1 Particular Behavior of Nanocrystalline Materials

Hall [1] and Petch [2] discovered that many properties of nanocrystalline metals have a unique relationship with the grain size of the material. Hall and Petch also recognized that as the grain size of the material decreases the strength increases until a critical grain size, approximately 20 nm. The properties of the nanocystalline materials below this critical grain size are not well understood and are of particular interest to experimental and computational material scientist. Therefore the ability to influence the grain size is an important step forward in optimizing the properties of nanocrystalline materials.

2.1.1 Stability of Nanocrystalline Structures and Grain Growth

Grains are identified as a group of neighboring atoms in the same crystallographic orientation. Grain boundaries are the disordered region between two unique grain orientations. Grain boundaries are less dense than the crystalline grains and store free volume throughout the boundary. Atoms in grain boundaries have higher energies than perfect crystalline atoms therefore are not energetically favorable. The energetic drive of the system is to reduce the excess energy of the structure by displacing atoms to lower energy positions through total grain boundary reduction, resulting in grain growth. It has been shown by Derlet et al. that the excess free energy is released as individual vacancies, which travel to the surfaces or into other grain boundaries [3,4].

Thermal Grain Growth

Classical models of grain growth state that grain size, D, is dependant on temperature, second-phase precipitates, and separation and transport of impurity atoms to grain boundary cores [5]. Coarse grains have exhibited a square root dependence for grain growth as a function of time, but grain growth for nanocrystalline materials (D < 100 nm) is not fully understood. Grain migration in coarse grained materials is driven by boundary-curvature-driven diffusion along the grain boundary cores. Yet in nanocrystalline metals, grain boundary migration is combined with excess volume within the grain boundary cores, triple junction's migration, and grain boundary rotation [6].

The grain growth rate for nanocrystalline materials is defined by Equation 2.1

$$D^n - D_o^n = Kt \qquad \textbf{Equation 2.1}$$

Where D is the grain size, D_o is the initial grain size which is often approximated to be negligible, K is a constant and t is time. Grain growth at nanocrystalline samples with (D > 100 nm) follow the classical growth shown in Equation 2.1, with n = 2 [5]. When Equation 2.1 is solved for D, we see a ½ dependence as a function of time. The square root dependence of time points to a diffusion-driven growth mechanism.

However nanocrystalline materials with grain sizes below 100 nm have been shown to exhibit linear growth rates where n = 1. It has been postulated that the cause for the hindered growth rate is the increase of grain boundaries in the system. More specifically, the growth rate is lower because there is a higher existence of vacancies which are known to increase Gibbs free energy and create a non-equilibrium state. The increased required energy therefore decreases the amount of grain boundary reductions and in turn negatively affects the grain growth.

Strain Induced Growth

At higher temperatures ($> \approx 0.5\ T_m$) thermal grain growth can easily be generated by removing the free energy volume from the grain boundaries. Yet, grain growth can also occur at lower temperatures. Strain induced grain growth has been observed in experiments and confirmed with MD simulations. The process in which the grains grow differs from that of thermal grain growth. During deformation nanocrystalline materials generate dislocations for grain sizes (D > 100 nm) and for the region of interest grain sizes (D < 20 nm) there is an interplay of grain boundary sliding, grain rotation, grain boundary migration, and partial dislocation emission. Through grain boundary sliding coupled with rotation the grain boundaries migrate to the lowest energy positions. As the grains migrate they leave behind the lower energy crystalline grains and grains begin to grow. Simulations of strain-induced grain growth have shown evidence that grains that are initially larger will continue to grow at the expense of the smaller grains which will decrease in size as mentioned by Schiotz [7,8].

2.1.2 (Inverse) Hall-Petch Effect

The Hall-Petch curve predicts materials of high yield strength at small grain sizes [1,2]. Using the equation

$$\sigma = \sigma_0 + kd^{-1/2} \qquad \textbf{Equation 2.2}$$

Where σ is the yield stress, σ_0 is the frictional stress to move an individual dislocation, and k is a material dependent constant (Hall-Petch Slope). This is the Hall-Petch relationship and has been verified by numerous experiments. It is understood that the reason for this increase in yield strength comes from the dislocations inability to

overcome the misorientations of the grain boundaries. As the sample continues to deform, more and more dislocations will emit and will begin to pile up. After some time, stress will build and it will eventually progress to dislocations in other grains. The critical stress needed to proceed has a relationship of $d^{-1/2}$. Though according to Masumura et al. [9] there are actually three regimes to the Hall-Petch Effect, where the yield stress has a different dependence on the grain size. The three regimes can be seen in Figure 2.1 [10,11]

1) The first region is considered the classic Hall-Petch relation with grain sizes a μm or larger and the well known dependence of $d^{-1/2}$.

2) The second region is approximately 1μm to about 20 nm and the exponent nears zero.

3) The third region is what region our nanocrystalline nanowires fall in, in which grain sizes are below <10nm. At this size, there has been experimental support that the strength may actually decrease instead of increase like region 1. This phenomena is considered the Inverse Hall Petch effect relation [12,13].

Zhu et al explain the different regions of the Hall-Petch effect and Hall-Petch inverse effect as the grain size decreases from 500 nm to below 10 nm [14]. Grain size ranges of 100-500 nm deform the samples similar to fine-grained materials; whereas the range of ~50 – 100 nm, dislocations are emitted and absorbed from grain boundaries; for ~20-50 nm, partial dislocations and deformation twinning are observed; and during the region of ~10-20 nm the deformation mechanism transitions from partial dislocation emissions to grain boundary sliding which becomes dominant for grain sizes below ~10 nm [14].

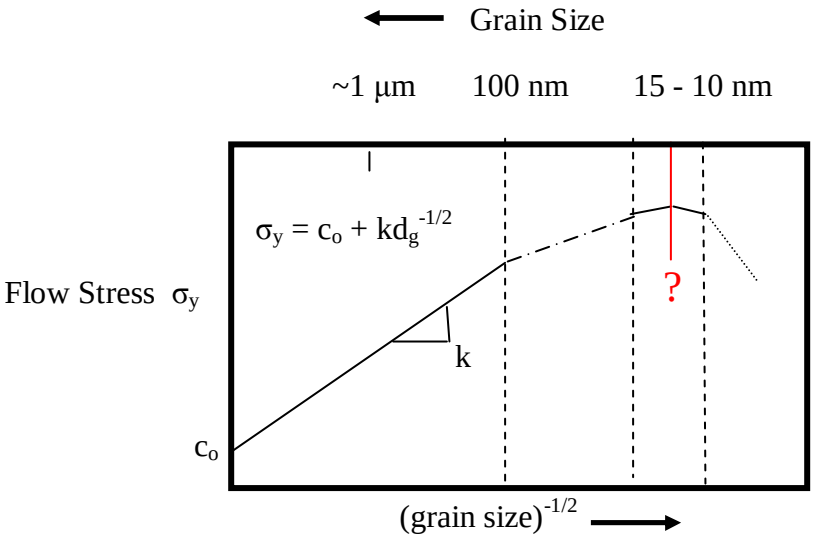

Fig. 2.1 The three regimes of the (Inverse) Hall-Petch effect [10]. The strength peak has been determined to be between 10 and 15 nm grain size [11].

Grain Boundary Sliding

The Hall-Petch effect shows the strength of materials as the grain size decreases, therefore it is important to study what affects the grain size. Grain boundary sliding (GBS) is influential in grain growth mechanism and the grain size for nanocrystalline materials. GBS is a process which incorporates small movements in atoms in order to find the global minimum energy structure. Each time GBS occurs the atoms move to another local energy minimum, the low energy mechanism of GBS does not increase Gibbs free energy and therefore may be energetically favorable to dislocation plastic deformation. An increase in the systems temperature will increase the likelihood of the atoms to move to the next local minimum, resulting in more grain boundary sliding. This assisted movement can also occur during strained deformation.

Primarily grain boundaries were found to be the reason for high strength nanocrystalline materials due to work hardening. Yet for small grain sizes ($D < 20$ nm) the high density of grain boundaries is partially responsible for the reduction in strength. The cause for the reduced strength is a change in the deformation mechanism from dislocation mediated deformation to an interplay between partial dislocation mediated plasticity and grain boundary accommodation of plasticity through grain boundary sliding [15]. Our studies of deformation mechanics for the nanocrystalline Ni nanowires confirm this transition of deformation mechanics, seen visually through the lack of dislocations at very high strains. Figure 2.2 shows a cross section of a Ni nanowire such a sample with 36% strain and less than 15 dislocations.

Fig. 2.2 The figure shows a slice through the wire deformed 36% colored according to the centro symmetry parameter, visualizing stacking faults and twins in the deformed structure.

2.2 Mechanical Behavior in FCC Metals

2.2.1 Dislocation Behavior

Dislocations are a form of plastic deformation observed in experimental studies and computational studies. In order to deform a sample it is energetically favorable for the dislocation to break a series of individual bonds as it travels through the sample, rather than break every bond at once. Dislocation propagation is shown in Figure 2.3 [17]. The path of the dislocation in a perfect crystal will be unimpeded and will continue until it reaches the surface. However for nanocrystalline structures there are numerous grain boundaries which act as barriers for dislocation paths. When dislocations are impeded there is a build up of stacking faults, thus increasing work hardening and yield strength.

Although grain boundaries act as barriers for traveling dislocations, they are also the main source for dislocation emission in nanocrystalline structures. Grain sizes equivalent to ~20-100 nm, contain higher grain boundary densities thus producing more sources for dislocation emission, leading to a dislocation dominated deformation mechanism. For small grain structures (D < 20 nm), dislocation mechanisms are less efficient than grain boundary sliding and are no longer the dominate deformation mechanism.

In nickel it has been shown that both full dislocations and partial dislocations are emitted during deformation [18]. In fact a full edge dislocation with a burgers vector $\frac{1}{2}\left[\bar{1}01\right]$ will glide along a (111) plane, but may also split into two Shockley partials with the Burgers vectors of $\frac{1}{6}\left[\bar{2}11\right]$ and $\frac{1}{6}\left[\bar{1}\bar{1}2\right]$ as seen in Figure 2.4. Dislocations in FCC

structures primarily have slip planes observed as [111]{110} because the [111] planes are densely packed and are likely to create stacking faults [19].

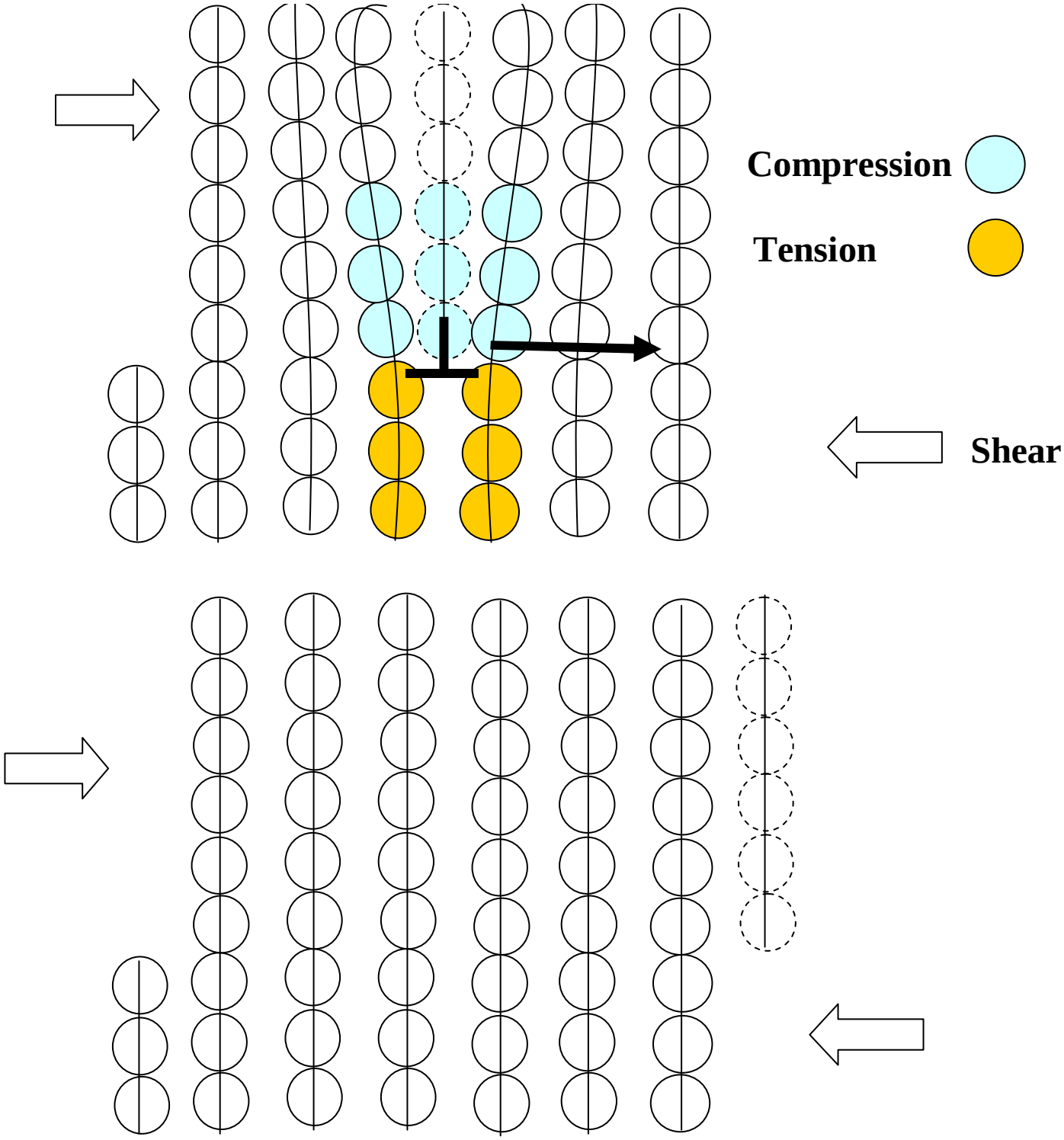

Fig. 2.3 Edge dislocation propagating through a material.

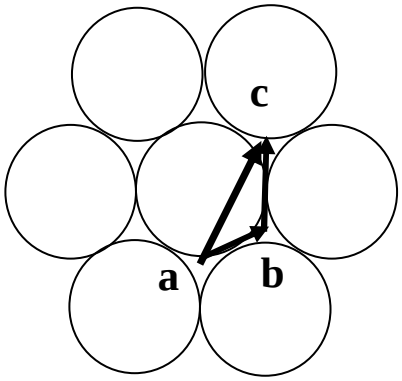

Fig. 2.4 The path of $\frac{1}{2}\left[\bar{1}01\right]$ full dislocation traveling the path (a) to (c) has a higher misfit energy than traveling through (a) to (b) to (c). The Shockley partials are $\frac{1}{6}\left[\bar{2}11\right]$ and $\frac{1}{6}\left[\bar{1}\bar{1}2\right]$ on the (111) glide plane.

Shockley partials have a leading or trailing characteristic and are some times termed as the 'positive' and 'negative' partials. Two partials interact similar to two magnets where like signs repel, Figure 2.5(a,b), and opposite signs attract. If two opposing signed partials come into contact it creates a full dislocation as seen in Figure 2.5(d), this process is also known as annihilation.

A full dislocation does not change the number of first or second neighbors in FCC materials and can be hard to visualize in computational studies. However when a partial dislocation travels through a grain, it leaves behind a stacking fault. Stacking faults have a unique number of neighbors allowing computers to identify them during simulations. Yet if the 'trailing' partial follows the leading partial, the stacking fault will be removed leaving a full dislocation path, leaving little evidence of deformation. Therefore in computational studies of deformation it is important to visualize and quantify the stacking faults over time before they annihilate.

To visualize these stacking faults, Centro symmetry parameter (CSP) is used in combination with atomic visualization softwares, such as AMIRA. Centro symmetry parameter was defined by Kelchner, Plimpton, and Hamilton [20]. CSP has grown in popularity in simulation research due to its easy coloring scheme based on quantifying the distance of neighbors giving specific ranges for different atomic conditions, some of these are stacking faults at the range of $5 < CSP > 7$, $0 < CSP > 4$ is a perfect crystal and $CSP > 10$ is for atoms at the surface.

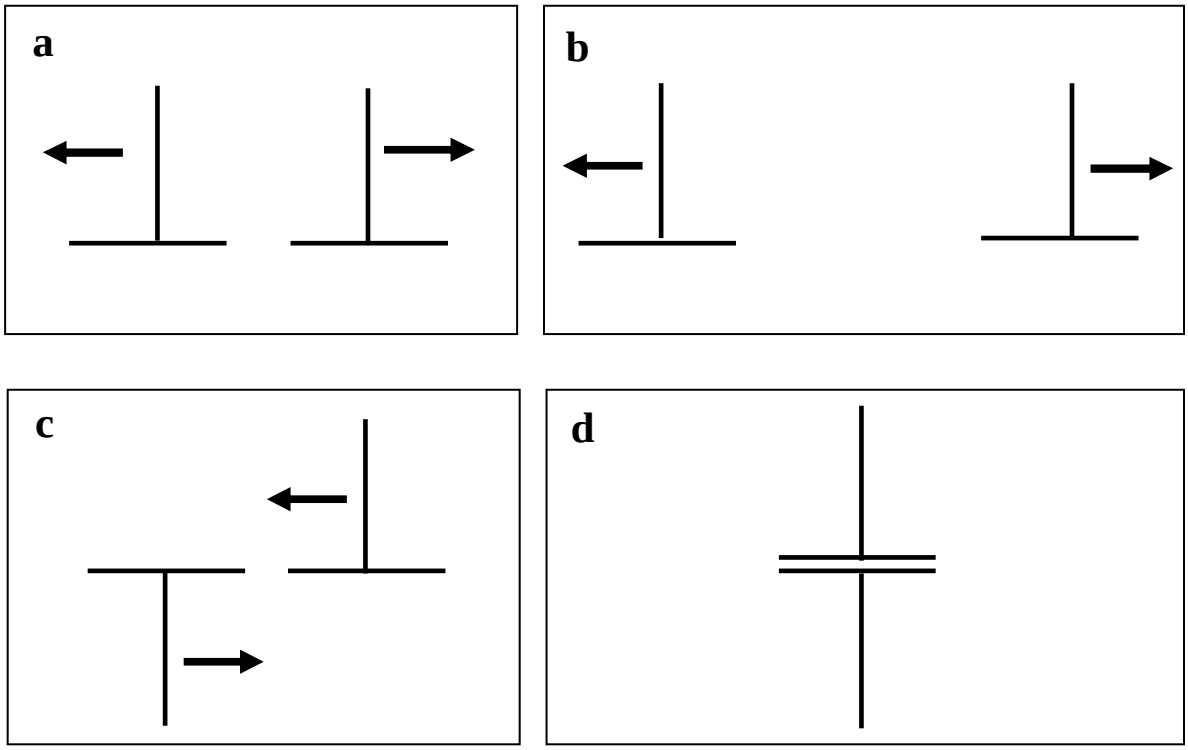

Fig. 2.5 Shows a simple diagram of the interaction between two a,b) like signed partials and c,d) opposite signed partials. d) Creates a full edge dislocation.

2.2.2 Twinning

According to Chen and Hemker, a twin is made up of partial dislocations and is equivalent to a $\sum=3$ grain boundary [21]. Twins are similar to grain boundaries because they also generate work hardening by hindering the motion of dislocations at the twin boundaries. In our studies we focus on two forms of twinning, deformation twinning and growth twinning.

Deformation twinning is common in FCC metals during large deformation or when the system has low stacking fault energies [22]. Deformation twinning or nanotwinning occurs when a number of stacking faults accrue next to one another during deformation; this creates a 70.5° mirror effect at the first stacking fault and one at the last stacking fault as shown in a zoomed in section of the 5 nm grain size nc-Ni during deformation, Figure 2.6. Deformation twinning has also been observed experimentally in aluminum in 2002 by Chen and Hemker [21].

To fully understand the twin's relationship with the deformation mechanisms at the nanoscale, Van Swygenhoven et al. ran simulations with growth twins virtually introduced into the initial structure of nanocrystalline copper, aluminum, and nickel [23]. The findings varied between metals, but it pointed towards the possibility that twins may affect or be in involved in the deformation mechanism.

Growth twins have been studied for many years and are well known in such phenomena as martensitic transformation and shape memory alloys [24-27]. Yet microstructures such as Multi-Twinned Rods (MTR) have only recently grown in interest amongst researchers [28-30]. Therefore microstructures that contain growth twins created by crystal nucleation were studied in this paper. Our interest was focused on the

stability of growth twins found in multi-twinned microstructures in silver. Our microstructures contained five twins which creates a star-like shape or a pentagonal nanorod as shown in Figure 1.1(C).

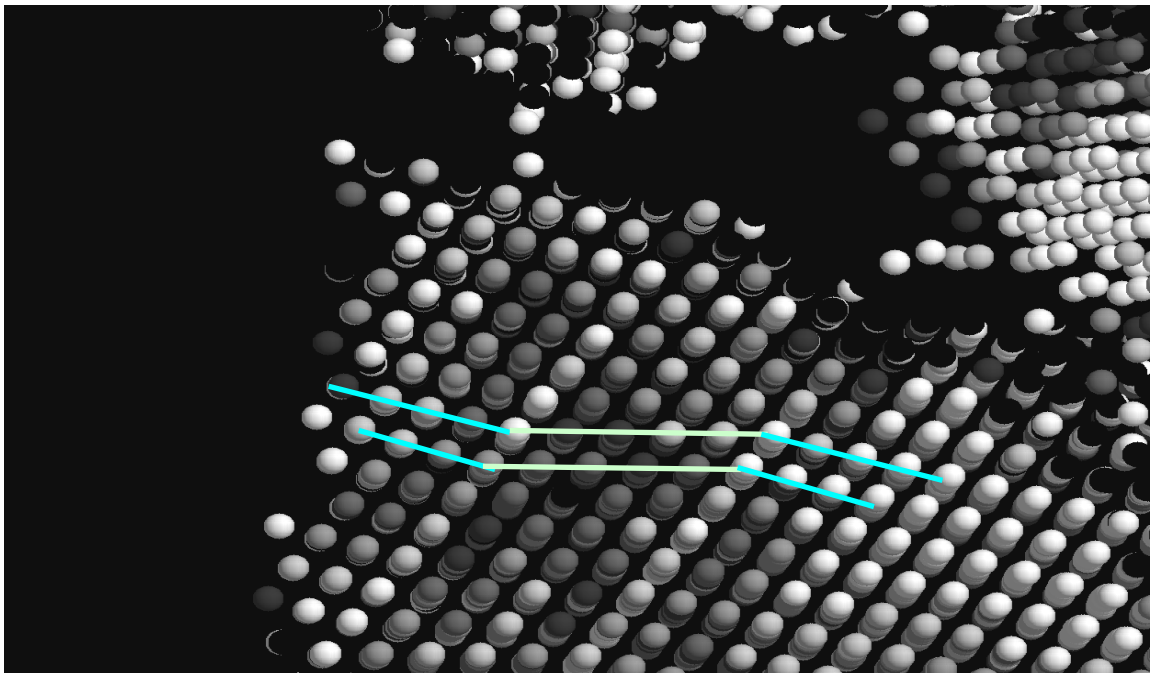

Fig. 2.6 Nanotwinning formed from consecutive stacking faults produced during deformation in a MD nickel simulation. The arrows represent the twin boundaries.

2.2.3 Sliding as a Deformation Mechanism

The nanocrystalline materials used in these studies are grain sizes (≤ 10 nm) and in recent studies it has been shown that the dominate deformation mechanism is grain boundary sliding (GBS) in two dimensional grain growth. In three dimensional studies, it has been found that the deformation mechanism is grain boundary accommodation which is the coupling of grain boundary sliding and grain rotation [3].

GBS is strongly determined by atomic shuffling according to Derlet et al. Atomic shuffling occurs during tensile deformation in a long and short range motion. The short range motion is consistent with individual atoms shifting positions from one grain orientation to another [3]. The long range was considered as stress-assisted free volume migration where groups of atoms move a number of atomics spaces away. The long and short range motions were reported to be the dominate influence on GBS.

2.3 Computational Methods

2.3.1 Molecular Dynamics

Atomic interactions in a metallic virtual material are realistically represented with the use of quantum mechanics through a time-dependent Schrodinger equation. However, due to computational limitations, it has been shown that molecular dynamic simulations based on classical mechanics have been known to reproduce experimental results of deformation mechanisms and atomic movements. Therefore in our studies the atomistic system of our MD simulations will evolve over time as particles are governed by Newton's second law. $F = m\,a$.

In an MD simulation, the position, atom mass and type, and the boundaries are defined. The initial configuration of these samples has an initial velocity dependent on the temperature of the system at time zero. As the environment changes, these velocities determine the relationship between neighbors for each Δt. Note that the timestep for these simulations are defined at 1 fs to allow for simulation motion of the atoms. For each Δt the position, force applied to the atoms, and velocities are incremental as the time is increased $t = t + \Delta t$. This process is repeated until the number of iterations chosen is reached. Due to the femtosecond timesteps required in MD simulations, the strain rates used in virtual deformation test such as tensile and compressive test are on the order of $10^7 - 10^9\ s^{-1}$. It has be shown by Koh and Lee that strain rates above $1 \times 10^{10}\ s^{-1}$ show unreliable results that can not be compared to experiments [31]. Keep in mind that experimental tensile tests are on the order of 10^{-4} to $10^3\ s^{-1}$ which are at a minimum four orders of magnitude slower than the tensile test we show in our studies. Yet by

comparing with experimental results we find similar phenomena, such as grain growth [32,33] and deformation twinning [21,22].

2.3.2 EAM Potentials

When computational studies began, they defined interactions between atoms similar to a classical spring, but as computers grew in capacity, newer more reliable ways have been produced. One such method is the embedded-atom method (EAM), created by Dawes and Baskes which mimics the interaction between atoms in metals and intermetallics [34]. EAM Potentials involve empirical formulas that simulate material characteristics such as the heat of solution, lattice constants, and surface energies. In our studies, we used four EAM potentials when necessary, two nickel potentials created by Voter & Chen [35] and Mishin [36]. In order to simulate silver we used a Voter & Chen potential [37]. These potential were used in all our simulations with the help of multi-processor software such as LAMMPS created by Plimpton [38].

Interactions amongst atoms within an MD system are governed by interatomic potentials. These potentials are created to replicate experimental data as close as possible, to provide practical information concerning atomistic behavior. The majority of the work done for nickel used the Voter & Chen nickel EAM potential, but for part of the research done for Mohanty's master thesis [5], we compared the Mishin & Farkas [36] and Voter & Chen [35] potentials. The Voter and Chen silver EAM potential was used to find the aspect ratio of the growth of multi-twinned rods [37].

The total energy of a monoatomic system is written as:

$$E_{total} = \frac{1}{2}\sum_{ij} V(r_{ij}) + \sum_{i} F(\overline{\rho_i}) \qquad \textbf{Equation 2.3}$$

where $V(r_{ij})$ is a pair potential as a function of the tensor *rij*, which is the distance between atoms *i* and *j*. *F* is the embedding energy that is a function of the host density, $\overline{\rho}_i$ is applied at site *i* by all of the other atoms within the system. The host density is given by

$$\overline{\rho_i} = \sum_{i \neq j} \rho(r_{ij}) \qquad \textbf{Equation 2.4}$$

The EAM potential data for two nickel potentials, Voter-Chen and Mishin-Farkas as well as the Voter-Chen silver potential are shown in Table 2.1. The experimental nickel data shown in Table 2.1 was taken from Mishin et al. and the experimental silver data comes from Garcia-Rodeja et al. [35-37,39].

Table 2.1 EAM potential data for nickel and silver [34-37]

Lattice Properties:	**Experiment Nickel**	**Mishin - Farkas Nickel**	**Voter -Chen Nickel**	**Experiment Silver**	**Voter - Chen Silver**
a_o (A)	3.52	3.52	3.52		
E_o (eV/atom)	-4.45	-4.45	-4.45		
R_d (A)			2.2	2.53	2.47
B (10^{11} Pa)	1.81	1.81	1.81		
c_{11} (10^{11} Pa)	2.47	2.47	2.44	1.24	1.25
c_{12} (10^{11} Pa)	1.47	1.48	1.49	0.934	0.928
c_{44} (10^{11} Pa)	1.25	1.25	1.26	0.461	0.456
Other Structures:					
E(hcp) (eV/atom)	-4.42	-4.43	-4.44		
E(bcc) (eV/atom)	-4.3	-4.3	-4.35		
E(diamond) (eV/atom)	-2.51	-2.5	-2.61		
Vacancy:					
E^{fv} (eV)	1.6	1.6	1.56	1.1	1.1
E^{d} (eV)			2.069	1.65	1.65
F (eV)	1.3	1.29	0.98		
Interstitials:					
E (Oh) (eV)		5.86	4.91		
E ([111]-dumbell) (eV)		5.23	5.37		
E ([110]-dumbell) (eV)		5.8	5.03		
E ([100]-dumbell) (eV)		4.91	4.64		
Plana\r defects:					
γ (mJ/m^2)	125	125	58		
γ_s (mJ/m^2)		366	225		
γ_T (mJ/m^2)	43	63	30		
γ_{GB}(210) (mJ/m^2)		1572	1282		
γ_{GB}(310) (mJ/m^2)		1629	1222		
Surfaces:					
γ (110) (mJ/m^2)	2280	2049	1977		
γ (100) (mJ/m^2)	2280	1878	1754		
γ (111) (mJ/m^2)	2280	1629	1621		

2.4 References

[1] E. O. Hall. Proceedings of the London Physical Society. **64** 747 (1951)
[2] N. J. Petch. J Iron Steel Inst **174** (1953)
[3] P.M. Derlet, A. Hasnaoui, and H. Van Swygenhoven, Scripta Materialia **49**, 629 (2003)
[4] Y. Estrin, G. Gottstein, and L.S. Scvindlerman, Scripta Materialia **50**, 993 (2004)
[5] S. Mohanty, Virginia Tech Master Thesis "Tensile Stress and Thermal Effects on the Grain Boundary Motion in Nanocrystalline Nickel", (Dec. 2005)
[6] C.E. Krill, L. Helfen, D. Michels, H. Natter, A. Fitch, O. Masson, and R. Birringer, Physical Review Letters **86**, 842 (2001)
[7] J. Schiotz, Mater. Sci. Eng., A **375-377**, 975 (2004)
[8]] J. Monk and D. Farkas. Physical Review B **75** 045414 (2007)
[9] R. A. Masumura, P. M. Hazzledine, and C. S. Pande. Acta Materialia, **46** 4527 (1998)
[10] K.S. Kumar, H. Van Swygenhoven, and S. Suresh, Acta Materialia, 51, 5743 (2003)
[11] J. Schiotz and K. Jacobsen, Science **301** 1357 (2003)
[12] A. H. Chokshi, A. Rosen, J. Karch, and H. Gleiter. Scripta Metall. **23** 1679 (1989)
[13] J. Schiotz, F.D. Di Tolla, and K. W. Jacobsen. Nature **391** (1998)
[14] Y.T. Zu and T.G. Langdon, Material Science & Engineering A **409**, 234 (2005)
[15] H. Van Swygenhoven, A. Caro and D. Farkas, Materials Science and Engineering A **309-310** 440 (2001)
[16] J. Schiotz, Nature **391**, 561 (1998)
[17] W.D. Callister, *Materials Science and Engineering: An Introduction*. 2nd ed. 2000, New York: John Wiley & Sons, Inc.
[18] P. M. Derlet and H. Van Swygenhoven, Phil. Mag. A **82**, 1 (2002).
[19] J.P. Hirth and J. Lothe, *Theory of Dislocations.* 2nd Ed. 1992, Florida: John Wiley & Sons, Inc.
[20] C.L. Kelchner, S.J. Plimpton, and J.C. Hamilton, Phys. Rev. B **58**, 11085 (1998)
[21] M. Chen, E. Ma, J. Hemker, H. Sheng, Y. Wang, and X. Cheng, Science **300**, 1275 (2003)
[22] J. Hemker, Science **304**, 221 (2004)
[23] H. Van Swygenhoven, P.M. Derlet, and A.G. Froseth, Nature Materials **3**, 399 (2004)
[24] R.D Lowde, R.T. Harley, G.A. Saunders, M. Sato, R. Scherms, and C. Underhill, Proc. R. Soc. Lond. A **374**, 87 (1981)
[25] M. Sugiyama, R. Oshima, F.E. Fujita, Trans Jpn. Inst. Met. **25**, 585 (1984)
[26] A.G. Kharchaturvan, S.M. Shapino, and S. Semenovskarva, Phys. Rev. B **43**, 10832 (1991)
[27] S. Kajiwara, MSE&A **173-175**, 67 (1999)
[28] L.D. Marks, Phil. Mag. A **49**, 81 (1984)
[29] B. Wu, A. Heidelberg, J.J. Boland, J. Sader, X.Sun, and Y. Li, Nano Letters **6**, 468 (2006)
[30] J. Reyes-Gasga, J.L. Elechiguerra, C. Liu, A. Camacho-Bragado, J.M. Montejano-Carrizales, and M. Jose Yacaman, Journal of Crystal Growth **286**, 162 (2006)
[31] S.J.A. Koh and H.P. Lee, Nanotechnology **17** 3451 (2006)

[32] E. Ma, Science **305,** 623 (2004)
[33] Z. W. Shan, E. A. Stach, J. M. K. Wiezorek, J. A. Knapp, D. M. Follstaedt, and S. X. Mao, Science **305,** 654 (2004)
[34] M.S. Daw and M.I. Baskes, Physical Review B **29,** 6443 (1984)
[35] A.F Voter and S. F. Chen, MRS Symposia Proceedings **82,** 175 (1987)
[36] Y. Mishin, M. Mehl, D. Farkas, and D. Papaconstantopoulos, Phys. Rev. B **59,** 3393 (1999)
[37] AF Voter and SP Chen, edited by RW Seigel, JR Weertmen and R Sinclair. Mater. Res. Soc. Symp. Proc. **82,** 175 (1978)
[38] S. J. Plimpton, J Comp Phys **117** 1 (1995)
[39] J. Garcia-Rodeja, C. Rey, L.J. Gallego, and J.A. Alonso, Phys. Rev. B **49**, 8495 (1994)

CHAPTER 3: Linear Grain Growth Kinetics and Rotation in Nanocrystalline Ni [1]

We report three dimensional atomistic molecular dynamics studies of grain growth kinetics in nanocrystalline Ni. The results show the grain size increasing linearly with time, contrary to square root of time kinetics observed in coarse grained structures. The average grain boundary energy per unit area decreases simultaneously with the decrease in total grain boundary area associated with grain growth. The average mobility of the boundaries increases as the grain size increases. The results can be explained by a model that considers a size effect in the boundary mobility.

3.1 Introduction

The properties of nano-crystalline metals have been investigated using computational methods in recent years [2-9]. Molecular dynamics has been utilized in this kind of simulation, with the limitation of the extremely fast strain rates that are imposed by the computational resources. The applications of nanocrystalline materials are limited by the thermal stability and the kinetics of thermal grain growth are critical for the structural stability of these materials. Both experimental and theoretical studies [10-13] have pointed out that grain growth kinetics in nanocrystalline materials may be different from that in coarse grained materials. The nano-scale effects in the kinetics can arise from a variety of factors, such as the role of triple junctions or grain rotation.

3.2 Simulation Technique

In this letter, we report simulation studies of grain growth kinetics in nanocrystalline Ni carried as a function of temperature. We study the grain growth process by monitoring the evolution of individual grains, the position of individual grain boundaries, and perform a statistical analysis of the overall micro structural evolution. The simulations were performed using a conventional molecular dynamics (MD) algorithm. The interaction between the atoms was modeled using an embedded-atom method (EAM) potential developed by Voter and Chen for nickel [14]. The sample was prepared using a Voronoi construction with an initial average grain size of 4 nm [6,7]. The initial nickel cube contained 15 grains and 100,000 atoms. The code used to run the MD tensile tests is LAMMPS, developed by S. Plimpton [15]. The sample was first equilibrated for 300 ps with periodicity in all directions and a temperature of 300K. This process insured a stable grain boundary structure [16]. After the initial relaxation, heat treatments were performed at temperatures from 900 to 1450 K.

3.3 Results

As the treatment proceeds, snapshots of the sample were created for visualization and analysis of the grain growth process. Figure 3.1 shows the microstructure evolution in a slice of the three dimensional sample after 500 ps, at 1300 K. The various grains are color coded, and individual atoms are not shown for clarity. The position of the grain boundaries in the sample was determined from an analysis of the continuity of the crystallographic orientation. The position of individual boundaries in slices such as that shown in Figure 3.1 was monitored as a function of time. Figure 3.2 shows an example

of the movement of one particular boundary in the sample as a function of time for various temperatures. The results show that the velocity of the grain boundary is maintained mostly constant and the values of the grain boundary velocity for each grain

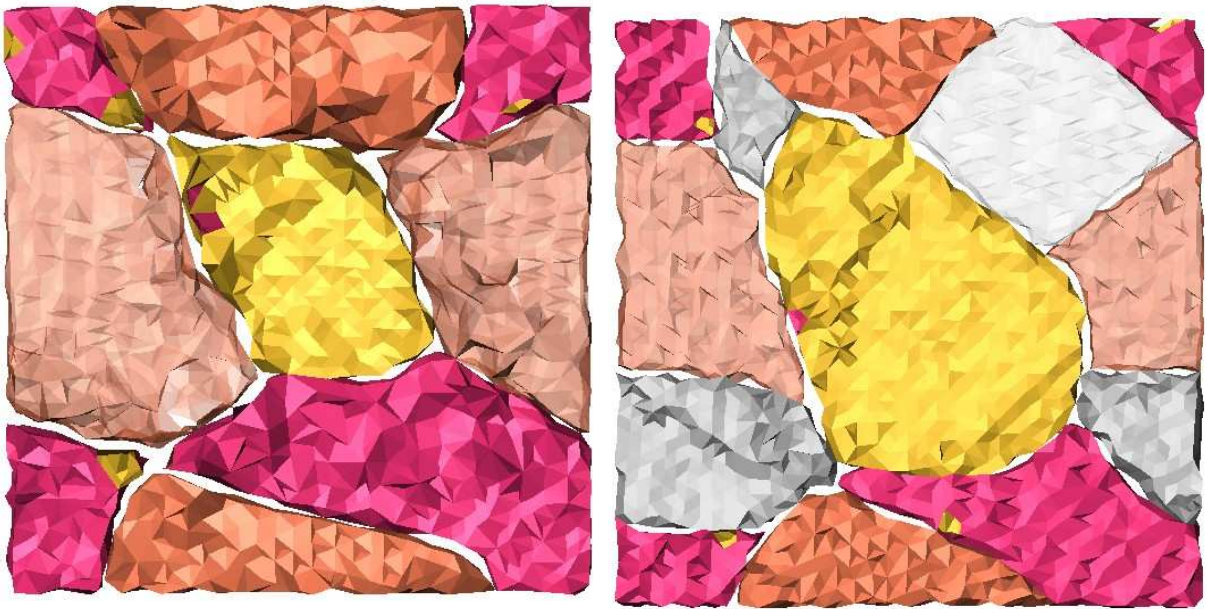

Fig. 3.1 Microstructure evolution after 500 ps at 1300 K. The grains are identified according to the continuity of crystallographic orientation.

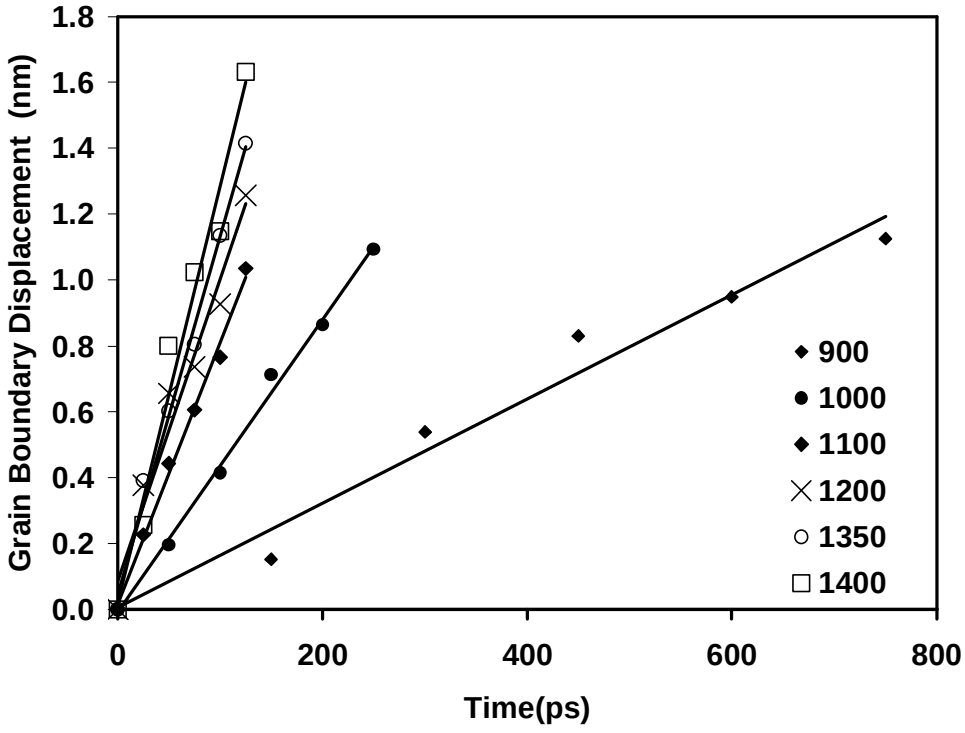

Fig. 3.2 Position of a particular grain boundary as a function of time for various temperatures.

boundary in the sample at each temperature can be extracted from this analysis. We found that the velocity of individual grain boundaries varied widely across the sample. For each temperature, a statistical analysis of the grain boundary velocities was performed. The results for the treatment at 1300K are shown in Figure 3.3. Table 3.1 shows the average grain boundary velocities and corresponding standard deviations obtained for each temperature.

Table 3.1: Average grain boundary velocities and standard deviations for various annealing temperatures.

Temperature (K)	Average velocity (m/s)	Standard deviation (m/s)
900	1.252	0.394
1000	3.610	1.011
1100	8.500	2.041
1200	10.711	2.414
1300	12.639	3.627
1450	21.146	7.992

Typically, the standard deviation observed at each temperature is around 30% of the average velocity. We estimate the error in the average velocities to be 2 to 5%. In addition to monitoring the position of individual boundaries, the average grain size was obtained as a function of time using the standard intersection technique normally used in experimental studies. For this analysis, intersections were counted in a total of 30 sections of the sample including 10 sections perpendicular to each of the spatial

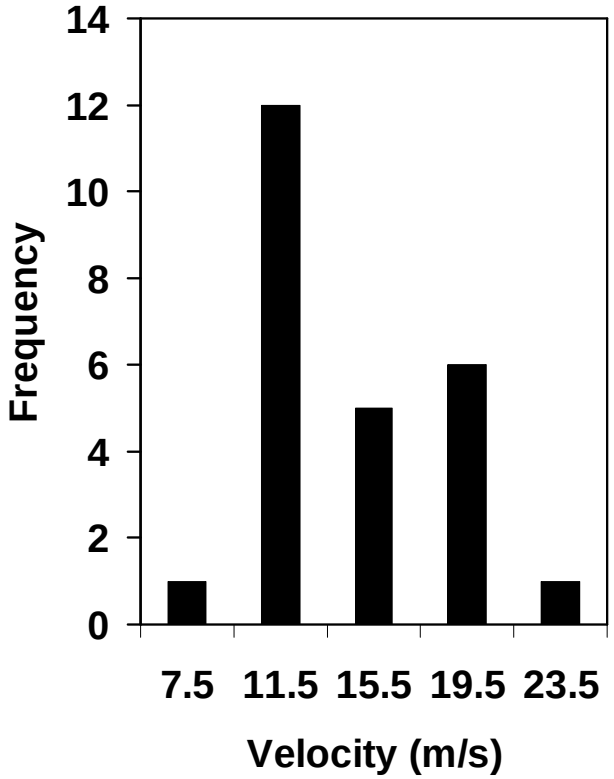

Fig. 3.3 Histogram of grain boundary velocities at 1300 K

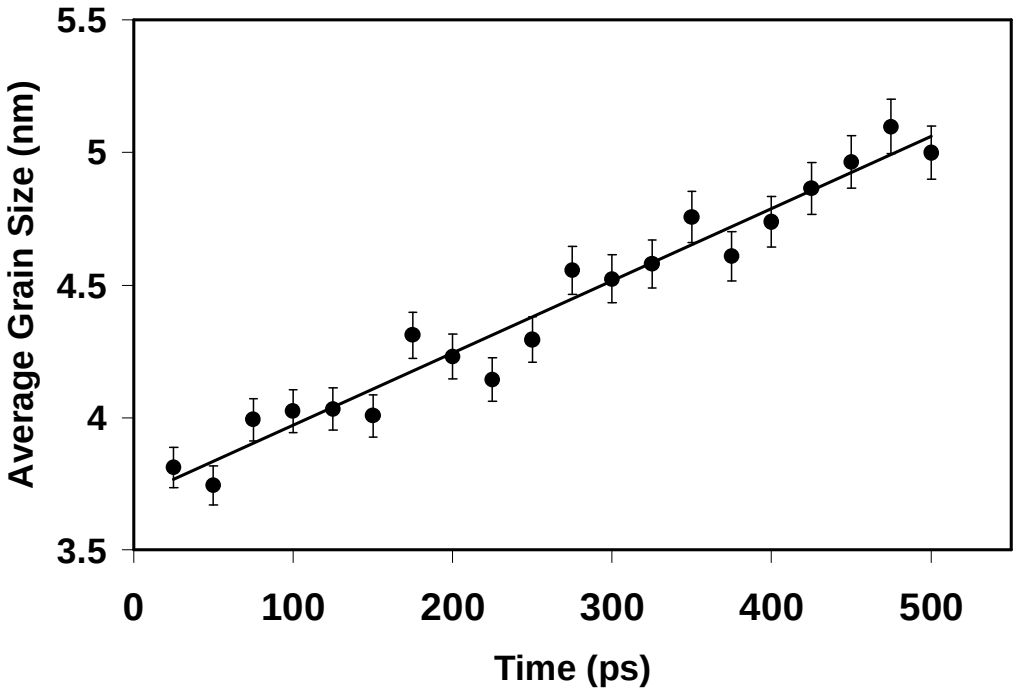

Fig. 3.4 Average grain size as a function of time obtained for 1300K

directions. Using this statistical procedure we obtain average grain sizes with an estimated 2% accuracy. The results are shown in Figure 3.4 for the treatment 1300K. This analysis was repeated for each temperature. In all cases, linear grain growth was obtained. We note that in this process, the number of grains has decreased to about half the original number, and therefore this does not represent an initial transient regime.

To complete the analysis of the observed grain growth process, we followed the energy evolution of the samples as a function of time for various temperatures. As an example, Figure 3.5 shows the results for 1300 K. In this figure the average potential energy per atom in the sample is plotted and we observe that the energy per atom in the sample E decreases as function of time with a square root of time dependence, $E = E_0 - Kt^{1/2}$, where E_0 is the average (temperature dependent) potential energy per atom in the initial equilibrated structure at t=0, and K is a temperature dependent constant. The values of the constant K obtained from this analysis can be plotted in Arrhenius form to obtain the activation energy for the process. Figure 3.6 shows these results together with the Arrhenius behavior of the average grain boundary velocities in Table 3.1. The activation energies obtained for the process using the average velocities and the energy evolution constants are nearly the same, namely 53 and 54 kJ/mol. In a recent study of grain boundary self diffusion using the same potential Mendelev et al. [17] studied a series of grain boundaries of different inclinations. They found that except for a symmetrical tilt boundary (103), the activation energies were 48 to 59 kJ/mol. This excellent agreement suggests that the process observed here is indeed controlled by the same individual atomic mechanisms as grain boundary self diffusion for non-special boundaries. The constant K depends on temperature through the temperature dependence

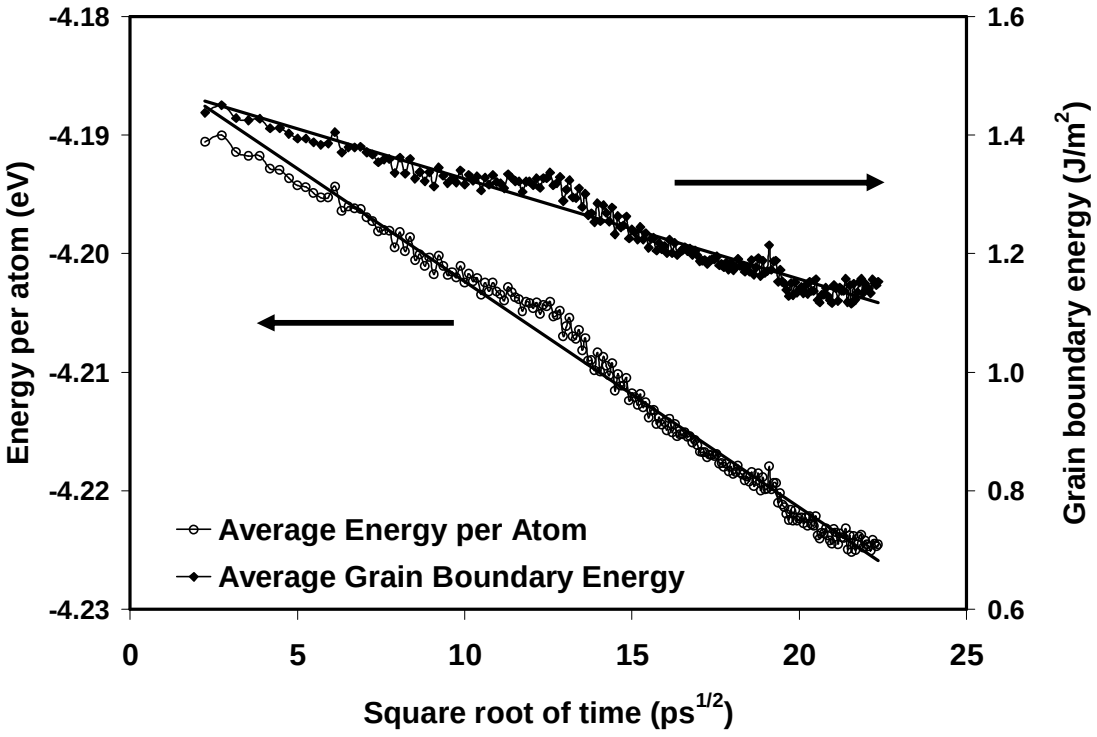

Fig. 3.5 Average block energy per atom and grain boundary energy as a function of time at 1300K

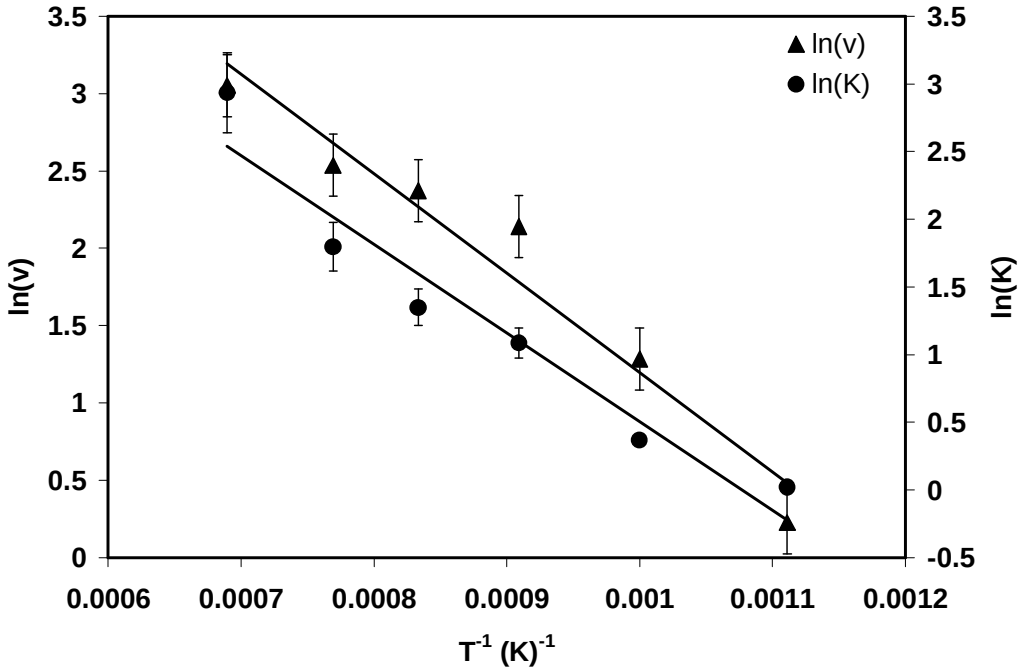

Fig. 3.6 Arrhenius plot of the average grain boundary velocities (v) and parabolic constants in the energy evolution (K) for the treatments at various temperatures.

of grain boundary mobility as well as any changes in the in the average grain boundary energy in the system. Usually, in modeling grain growth the average grain boundary energy is taken as a constant. As described below, we found that is not the case in our simulations, and this means that the relation of the constant K and mobility is not straight forward because there are two processes that contribute to the total energy decrease, namely a decrease in total grain boundary area and a decrease of the average energy per unit area.

From our results, it is possible to obtain the average grain boundary energy per unit area by combining the results obtained for the total energy evolution of the sample and those for grain size increase. For this purpose we have estimated the total grain boundary area in the sample as follows: if the volume of the sample V is constant as the grain growth proceeds, there will be N grains with an average volume $v = V/N$. If the grains are considered cubic in shape this means that the average area of each grain is 6 $[V/N]^{2/3}$. The total area of grain boundary is then $A = 3V^{2/3} N^{1/3}$. In this geometry, $N=V/d^3$, where d is the grain size and the total area is then $A= 3V/d$. Alternatively, if the grains are considered spherical, the area of each grain is $4\pi [3V/4\pi N]^{2/3}$ and the total area is $A = ½3^{2/3}[4\pi]^{1/3}V^{2/3} N^{1/3}$. In this geometry, $N=6V/\pi d^3$ and in terms of d, the total grain boundary area is again $A = 3V/d$. We use this relation to estimate the total grain boundary area for grains of arbitrary shape. Note that this estimate treats the outer boundary of our simulation cell as a grain boundary and in the limit of only one grain in the system it gives the total grain boundary area as one half the outer area of our simulation cube of volume V. The total energy of the grain boundaries contained in the sample was obtained as $E_{gb} = n(E – E_{pl})$, where n is the total number of atoms in the

sample and E_{pl} is the energy of the perfect lattice at the simulation temperature. Finally, the average grain boundary energy per unit area can be calculated as $\gamma = E_{gb}/A$. The results are included in Figure 3.5 for the grain boundary energy evolution during the treatment at 1300K. The initial grain boundary energy obtained at this temperature is 1.4 mJ/m^2 again in excellent agreement with the values obtained by Mendelev et al [16] using the same potential. As the simulation proceeds, the average grain boundary energy per unit area decreases significantly to 1.1 J/m2. During the treatment time (500 ps) the number of grains in the sample decreased from the initial 15 to 6. The average grain size increased from 3.7 to 4.5 nm. The decrease in grain boundary energy per unit area does not occur during the initial transient period, but rather it occurs during the entire process in which the grain size increased by over 20% and the total number of grains decrease to about half the original number. This occurs through a process of simultaneous grain boundary migration and grain rotation.

Table 3.2: Rotation angles around the z and x axis observed for the central grain in the simulation at 1300K.

Annealing time (ps)	25	50	100	250	325	425	500
Rotation around the z axis, (degrees)	1.70	2.77	2.69	5.66	5.48	6.60	3.11
Rotation around the x axis (degrees)	-0.86	-2.23	-3.43	-0.34	0.19	-0.97	-2.12

Table 3.2 shows the rotation angle for the center grain of the sample as a function of the annealing time. The table shows rotation angles around the z and x axis, and values up

to 6 degrees were observed. These results suggest that significant grain rotation accompanies the observed decrease in average grain boundary energy. Based on a simple model employing a stochastic theory, Moldovan et al. [18] investigated the coarsening of a 2-dimensional polycrystalline microstructure due solely to a grain-rotation coalescence mechanism. Their work shows that the growth exponent is critically dependent on the rotation mechanisms. The rate of grain boundary energy decrease with rotations observed in our results is of the same order of magnitude as that reported by Moldovan et al. [18] based on simulations in Pd. We obtain a rate of 2.44 J/m^2 rad^{-1}, which can be compared to their reported value of 4.5 J/m^2 rad^{-1}. Moldovan et al. [19] also present a theory of diffusion-accommodated grain rotation. Applying the equations they derived to our case, we obtain a rate of rotation around the z axis of 1.6×10^8 rad/s. This can be compared with the rotation rate we observe from the data in Table 3.2 which is $2.7\ 10^8$ rad/s.

We now turn to a more detailed analysis of the reasons for the linear kinetics observed. Assuming that the grain boundary curvature induced driving force decreases with increasing grain size, the grain boundary mobility should constantly increase to keep the migration velocity constant. Figure 3.7 shows the calculated grain boundary mobility assuming the standard curvature driven driving force and an average velocity of 12.639 m/s found in our analysis (Table 3.1) for 1300K. The figure shows a linear dependence of the mobility on the inverse grain size. The mobility increase found in our simulations as the grains grow can not be attributed to the fact that the average grain boundary energy decreases, because low energy, low-angle and special boundaries are usually less mobile than high-angle random boundaries. Our result therefore implies a significant size effect,

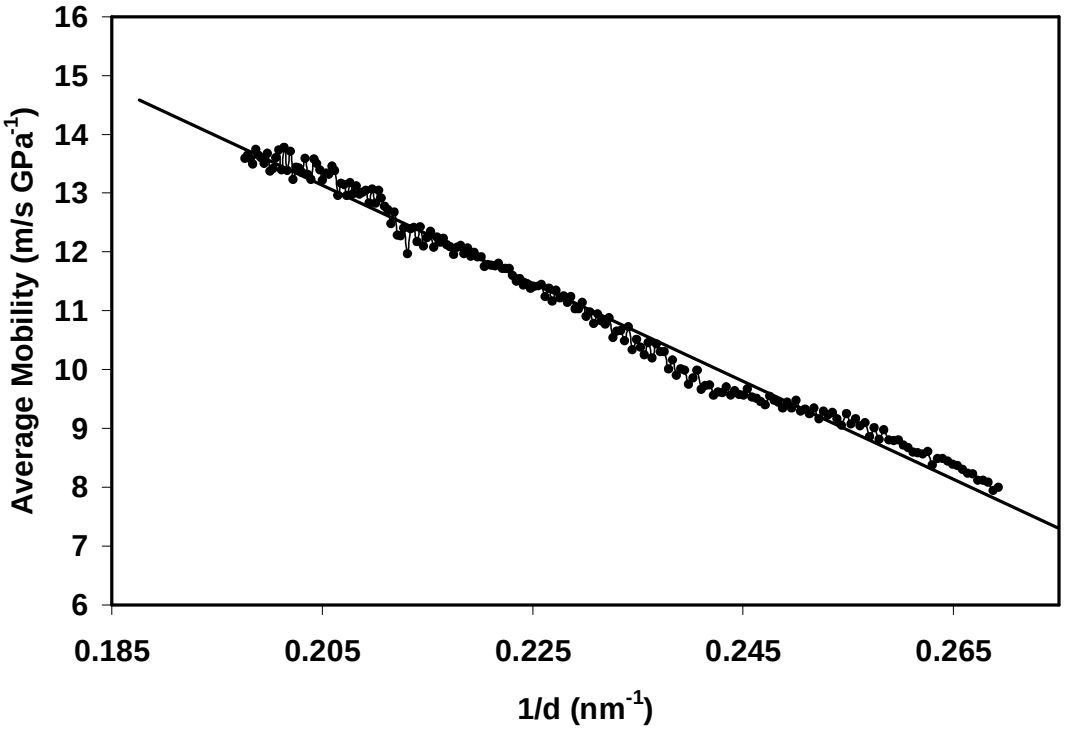

Fig 3.7 Average grain boundary mobility as a function of time for the treatment at 1300K.

with the mobility of boundaries constrained by nanometer grain sizes being lower than that of equivalent boundaries in macroscopic size grains. We postulate that the size effect is due to the fact that the boundary regions near the triple junctions have a decreased mobility. This assumption is similar to that proposed by Zhou, Dang and Srolovitz [20] in a recent study of size effects on grain boundary mobility in thin films. In the thin film geometry, the driving force for migration was maintained constant and the velocity of a single planar boundary was found to increase with film thickness. Zhou, Dang and Srolovitz [20] attribute the mobility decrease for thinner films to the fact that the boundary regions near the surface have a lower mobility. A simple model can be constructed along the same lines, assuming that the mobility of the boundary in regions near the triple junctions is lower. This model predicts that the mobility should follow the form [20] $M = M^{\infty}$ [1-m/d] where d is the grain size and M^{∞} is the grain boundary mobility for macroscopically sized grains. Figure 3.7 shows the results of fitting our data to this equation and we obtain M^{∞} = 30.2 m s^{-1} GPa^{-1} and m = 2.78 nm. Our results are consistent with this simple model for the size effect in the mobility of grain boundaries for nano-sized grains. The value of m obtained represents the range of the effect of triple junctions on grain boundary mobility. For thin films, reference 19 reported a similar dependence of the mobility of a planar asymmetric Σ =5 boundary on film thickness using the same interatomic potentials at 1200 K [19] with values M^{∞} = 135 m s^{-1} GPa^{-1} and m= 1.11 nm.

3.4 Discussion

In summary, our results show that for 4 nm grain size nanocrystals, linear grain growth kinetics are observed, contrary to the well known square root of time kinetics

observed in coarse grained counterparts. The linear grain growth can be attributed to the fact that the mobility of nano-sized grain boundaries are size dependent and significantly increase as the grains grow. The growth process for these very small sizes is accompanied by grain rotation and a decrease in the average grain boundary energy per unit area. The activation energy obtained for the process coincides with that observed for grain boundary self diffusion in general boundaries. The mobility of the grain boundaries increases with grain size and the linear grain growth kinetics is consistent with a simple model for the size effect on the mobility.

3.5 Acknowledgments

This work was supported by NSF, Materials Theory and performed in System X, Virginia Tech's teraflop computing facility. We acknowledge helpful discussions with A. Rollet, E. Holm, M. Mendelev and E. Bringa. Thanks to S. Plimpton for providing LAMMPS.

3.6 References

[1] D. Farkas, S. Mohanty, and J. Monk. Phys. Rev. Letters **98**, 165502 (2007)
[2] J.R.Weertman, D. Farkas, K. Hemker, H. Kung, M. Mayo, R. Mitra, and H. Van Swygenhoven, MRS Bulletin **24**, 44 (1999)
[3] J. Schiotz and K. Jacobsen, Science **301**, 1357 (2003)
[4] J. Schiotz, T. Vegge, F. Tolla, and K. Jacobsen, Phys. Rev. B **60**, 19711 (1999)
[5] J. Schiotz, Scripta Mater. **51**, 837 (2004)
[6] H. Van Swygenhoven, M. Spaczer, A. Caro, and D. Farkas, Physical Review B **60**, 22 (1999)
[7] H. Van Swygenhoven, A. Caro, and D. Farkas, Materials Science and Engineering A **309-310**, 440 (2001)
[8] D. Farkas and W.A. Curtin, Materials Science and Engineering A **412,** 316 (2005)
[9] A.J. Haslam, D. Moldovan, V. Yamakov, D. Wolf, S.R. Phillpot, and H. Gleiter, Acta Materialia **51**, 2097 (2003)
[10] C.S. Pande and R.A. Masumura, Materials Science and Engineering A **409,** 125 (2005)
[11] M. Hourai, P. Holdway, A. Cerezo, and G.D.W. Smith, Materials Science Forum **386-3**, 397 (2002)
[12] A.J. Haslam, S.R. Phillpot, H. Wolf, D. Moldovan, and H. Gleiter, Materials Science and Engineering A **318,** 293-312 (2001)
[13] C. E Krill, L. Heflen, D. Michels, H. Natter, A. Fitch, O. Masson, and R. Birringer, Physical Review Letters **86**, 842 (2001)
[14] A.F Voter and S. F. Chen. MRS Symposia Proceedings **82**, 175 (1987)
[15] S. J. Plimpton, J Comp Phys **117**, 1 (1995)
[16] H. Van Swygenhoven, D. Farkas, and A. Caro, Physical Review B **62**, 831 (2000)
[17] M.I. Mendelev, H. Zhang, and D.J. Srolovitz, Journal of Materials Research, **20**, 1146 (2005)
[18] D. Moldovan, V. Yamakov, D. Wolf, and S. Phillpot , Physical Review Letters **89**, 206101 (2002)
[19] D. Moldovan, D.Wolf, and S. R. Phillpot, Acta Mater. **49**, 3521 (2001).
[20] L. Zhou, H. Dang, and D.J Srolovitz, Acta Mat. **53**, 5273 (2005)

CHAPTER 4: Strain-driven grain boundary motion in nanocrystalline materials [1]

We report fully three dimensional atomistic molecular dynamics studies of strain induced grain boundary mobility in nanocrystalline Ni at room temperature. The position of a statistically significant number of grain boundaries was monitored as a function of the strain level for a strain rate of $3.3\ 10^{8}\ s^{-1}$ for two different interatomic potentials. The results show the grain boundaries migrating with velocities of 2 to 3 m/s, depending on the interatomic potential used. Detailed analysis of the process shows that grain boundary migration is accompanied by grain rotation and in many cases dislocation emission. The results suggest that grain rotation, grain boundary sliding, and grain boundary migration occur simultaneously in nanocrystalline metals as part of the intergranular plasticity mechanism. The effects of free surfaces present in the sample on these related mechanisms of plasticity were investigated in detail and it was found that the presence of free surfaces lowers the flow stress observed for the samples and increases the amount of grain boundary sliding, while actually decreasing the average velocity of grain boundary migration parallel to itself. Finally, we report observations of grain coalescence in the samples with a free surface. The results are discussed in terms of the coupling of grain boundary sliding and migration.

4.1 Introduction

The properties of nanocrystalline metals have been a major focus for computational materials science in recent years [2-9]. Large scale atomic level simulations using massively parallel computers allow the study of deformation behavior of materials with features at the nanoscale. Simulation results can provide improved understanding of the underlying mechanisms of plastic deformation at different strain rates and grain sizes. Molecular dynamics has been utilized extensively in performing this kind of simulation work, with the limitation of the extremely fast strain rates that are imposed by the currently available computational resources. These efforts are now at the point where the largest sizes attainable in simulations using empirical potentials are similar to the smallest used in experimental studies. Nanocrystalline structures are of particular interest because of their increased hardness and because of the appearance of particular phenomena at the nano-scale such as the reversal of the Hall–Petch Effect, typical of the coarse grained counterpart structures [2]. Grain growth is an important limitation to the use of nanocrystalline materials in most applications, since it is well known that grain growth occurs during the thermal annealing of nanocrystalline metals and alloys, even at relatively low annealing temperatures, [10]. In addition, recent experimental work has shown that grain coarsening may occur during indentation or tensile deformation of nanocrystalline metals [11-16]. Grain growth has been observed that appears to be clearly associated with the plastic deformation process and nanograins are seen to grow as they are deformed. These studies constitute significant experimental evidence of grain growth and rotation at room temperature for small grain sizes at high deformation levels. In these experimental studies it is difficult to determine the role of

thermally activated processes in the observed grain growth. Recently, Farkas and van Swygenhoven [17] reported simulation results showing grain boundary motion in nanocrystalline Ni. The digital sample, containing 200 grains of 4 nm average grain size, was deformed to strain levels up to 12% at room temperature using molecular dynamics techniques and an empirical potential. In that framework, thermal contributions are ruled out by the very short times used for the deformation at room temperature. Grain boundary motion for distances up to 2.5 nm, or half the grain size was observed. These results support the notion of purely stress driven grain boundary migration in nanocrystalline materials that could be a part of the deformation mechanism. These molecular dynamics simulations suggest that the grain growth observed at low temperatures during plastic deformation may be purely stress- driven. Several factors can contribute to this phenomenon, including grain boundary migration driven by mechanical energy and curvature-driven grain boundary migration and/or grain rotation-induced grain coalescence.

In this paper, we report detailed simulation studies of grain boundary migration kinetics in nanocrystalline Ni driven by an applied strain at room temperature. We study the grain boundary migration process by monitoring the position of individual grain boundaries and perform a statistical analysis of the migration process. The simulations were performed using a conventional molecular dynamics (MD) algorithm and a Nose-Hoover thermostat. The interaction between the atoms is modeled using two different embedded-atom method (EAM) potentials developed by Voter and Chen for nickel [18] and Mishin et al. [19]. We also study the influence of the presence of free surfaces on the migration process, since the grains near the sample surface can slide and rotate in a

different way. We conclude with an assessment of the effects of free surfaces on the sliding and migration components of the grain boundary response to strain.

4.2 Sample generation and simulation methodology

The sample was prepared using a Voronoi construction with an initial average grain size of 4 nm [6,7]. The initial digital nickel sample contained 15 grains and approximately 100,000 atoms. The code used to run the MD tensile tests is Lammps, developed by S. Plimpton [20]. The sample was first equilibrated for 300 ps with periodicity in all directions and a temperature of 300K using a Nose-Hoover thermostat and barostat. This process insured a stable grain boundary structure, as described in previous work [6]. After the initial relaxation, deformation treatments were performed at a strain rate of 3.3×10^{8} s^{-1} using two different interatomic potentials and two different kinds of boundary conditions. The first set of boundary conditions is periodic in all three directions, representing a sample with no free surfaces. In the second set of boundary conditions periodicity is used only along the tensile axis and free surfaces are present in the other two spatial directions. As the treatment proceeds, snapshots of the sample were created for visualization and analysis of the grain boundary mobility process. Two different treatments were performed using the two sets of boundary conditions for each interatomic potential. The strain was applied by increasing the sample dimensions along the tensile axis. We used a Nose-Hoover barostat to maintain zero pressure in the other two spatial directions for the first set of boundary conditions. The second treatment was performed using periodic boundary conditions only in the direction of the tensile axis and

free surface boundary conditions in the other two directions. The temperature was maintained at 300K for all simulations.

For all cases, the stress on the sample was obtained as a function of the applied strain, allowing the generation of stress strain curves. The simulations therefore represent virtual tensile tests. In the case of periodicity used in all directions they represent tensile tests of thick specimens, whereas in the case where free surfaces are present the simulations mimic tensile tests of samples of small overall dimensions. This allows for the study of the effects of the free surfaces on the plastic deformation mechanisms. For these small grain sizes, the main plastic deformation mechanisms are expected to be intergranular, dominated by grain boundary plasticity. Dislocation mediated intragranular plasticity starts to be important for grain sizes over 10 nm [2-8]. Our results therefore will address the various components of grain boundary plasticity, in a situation were dislocation mediated plasticity is not dominant.

4.3 Results

Stress strain behavior

Figure 4.1 shows the stress-strain curves obtained as the digital samples were deformed. The deformation process was performed under strain controlled conditions and the corresponding stress developed in the sample was plotted as a function of strain to obtain the curves shown in Figure 4.1. The results show that the sample with no free surfaces has a flow stress of around 2.5 GPa in the simulation with the Voter and Chen [18] interatomic potential and 4.3 GPa if the Mishin et al. [19] potential is used. This result points out to the fact that in a quantitative sense, plasticity depends on the detailed

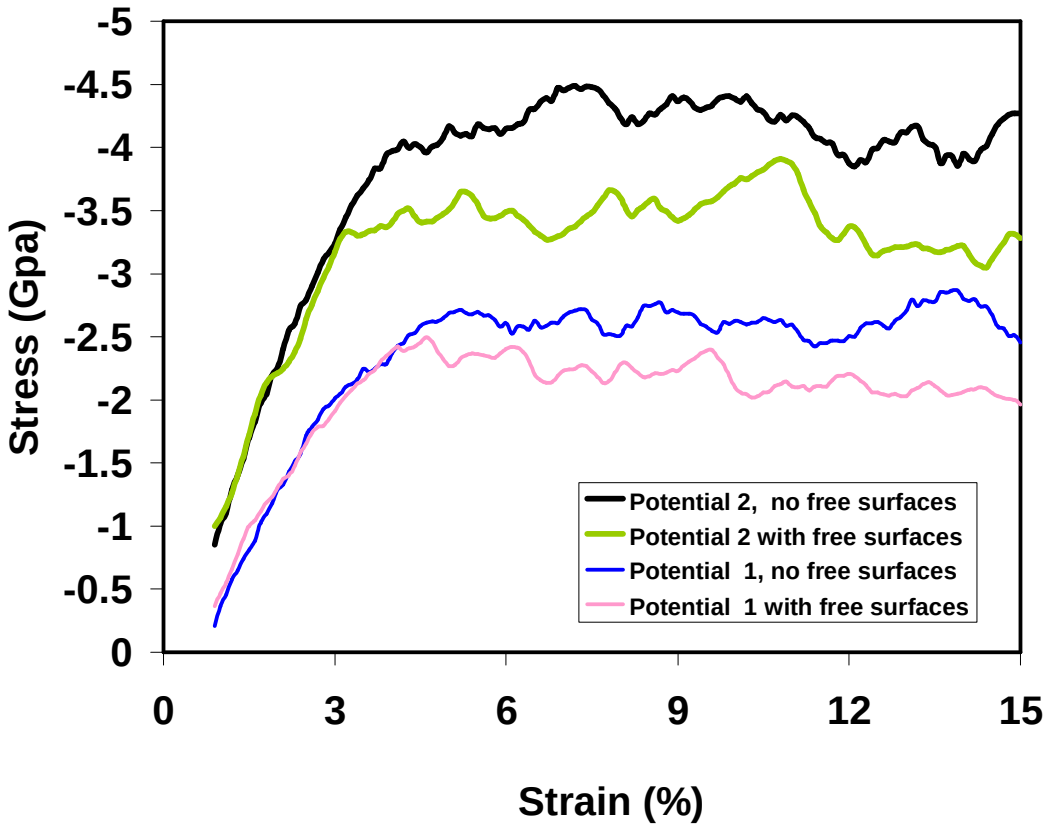

Fig. 4.1 Stress strain curves obtained for the nanocrystalline samples using two different interatomic potentials and both wit and without free surfaces. Potential 1 [18] and Potential 2 [19].

characteristics of the interatomic potential used. The reason for this is that the actual values of flow stresses are related to highly non-equilibrium atomic configurations, not usually considered in the fitting of potentials that relies more on the equilibrium lattice properties. The potential of Mishin et al. [19] was developed based on first principle calculations of metastable phases, including bcc, hcp and simple cubic, and is therefore expected to have a better transferability. However, experimental comparison of properties directly related to flow stresses is difficult and therefore we can not say which of the potentials is more quantitatively reliable for the actual values of the flow stress. Our results show that the values obtained here for flow stresses are significantly dependent on the potential used. The potential by Mishin et al. [19] depicts a material much harder to deform than that of Voter et al. [18].

Despite these very significant quantitative differences the trends observed in the effects of the free surfaces are the same for both potentials, namely that the presence of the free surfaces decreases the flow stress by 20 to 25%. This means that tensile tests of small nanocrystalline samples of the dimensions tested here yield noticeable softer results than those of thicker samples. For both potentials, our results indicate that introducing free surfaces in the sample aids plastic flow. Most of the deformation for these small grain sizes occurs through the grain boundaries and grain boundary plasticity mechanisms control the values of the flow stress. The decrease of the flow stress can therefore be associated with increased grain boundary plasticity in the sample with free surfaces. In the following section we analyze the details of grain boundary sliding, rotation and migration for samples with and without free surfaces.

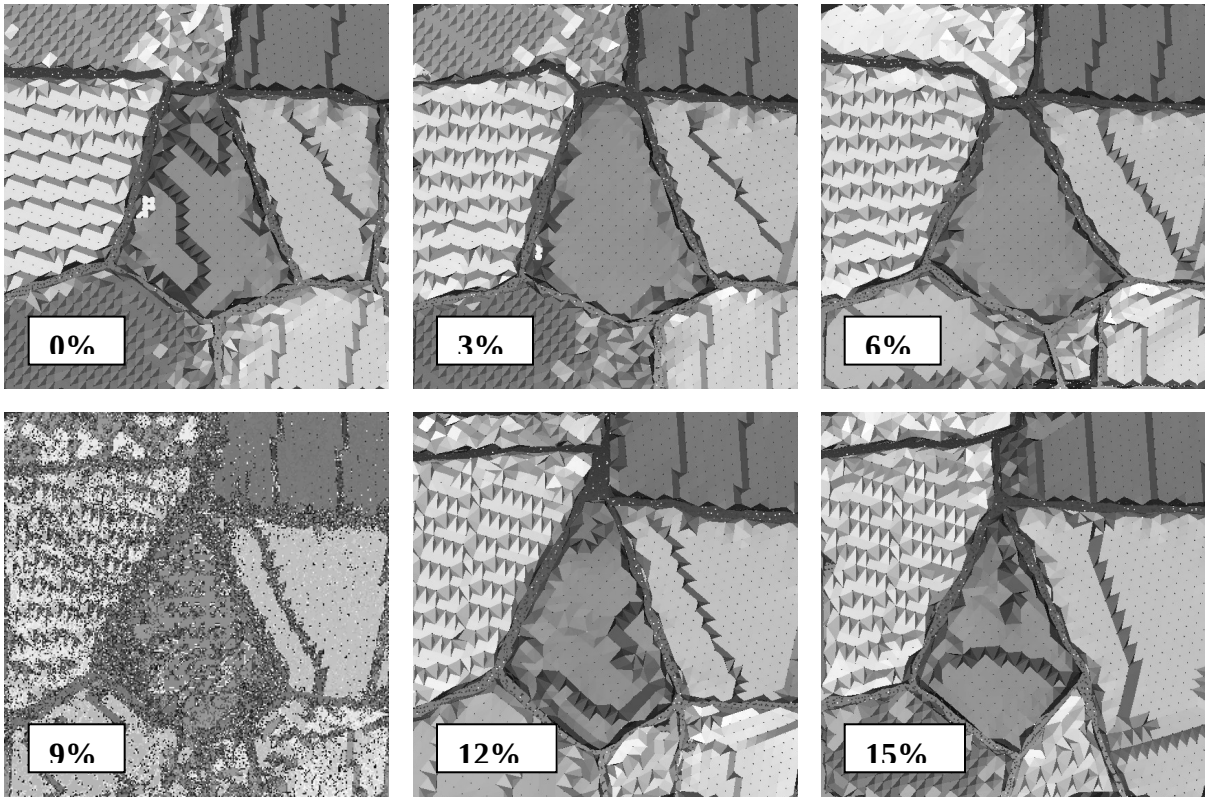

Fig. 4.2 Micro structural evolution during the tensile test process for a sample with free surfaces and interatomic potential 1 [18]. Visualization according to the continuity of crystalline orientation. The sections shown are perpendicular to the tensile axis.

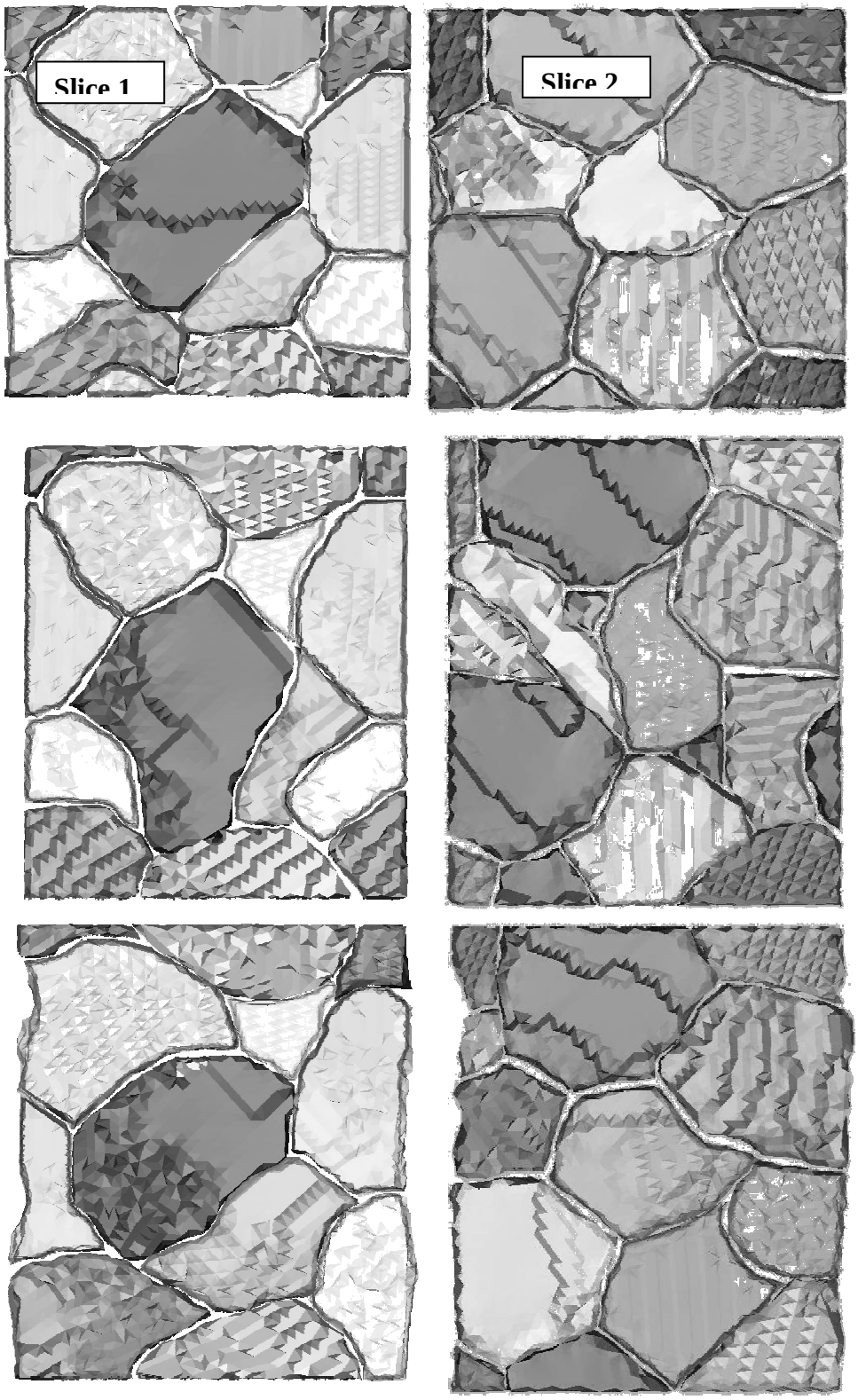

Fig. 4.3 Two slices of the sample in the initial relaxed state (top) and deformed 15% with (bottom) and without free surfaces (center) Visualization performed according to the continuity of crystalline orientation. The tensile axis is vertical. Interatomic potential 1 [18].

Microstructural evolution

Figure 4.2 shows the microstructure evolution in a slice of the three dimensional sample containing free surfaces. Significant microstructural changes are seen to occur as the deformation process proceeds and for this particular sample and slice the disappearance of a grain can be seen in the lower left corner. Most boundaries are observed to migrate during the process. To quantify this migration in a statistically relevant manner, the position of the grain boundaries in each sample was determined as a function of time from an analysis of the continuity of the crystallographic orientation. In Figure 4.2, the various grains are color coded, and individual atoms are not shown for clarity.

Figure 4.3 shows a comparison of the microstructural changes occurring in the sample after 15% deformation with and without free surfaces. Significant microstructural changes occur in both cases, as can be seen in the two slices of the three dimensional sample shown in this figure as examples. Figure 4.4 shows a similar comparison in a slice where the atomic positions are indicated. The atomic symbols in this case are colored according to the local hydrostatic pressure calculated for each atom. Figure 4.5 shows further detail of a particular boundary in this slice, showing grain boundary migration accompanied by the emission of a dislocation into the left grain. The grain boundary is significantly deviated from its initial position in both cases.

In a more quantitative sense, Figure 4.6 shows an example of the position of an individual boundary measured in slices such as that shown in Figure 4.5, monitored as a function of time, for the samples with and without fee surfaces. The results show that for both cases the velocity of the grain boundary is maintained mostly constant and the values of the grain boundary velocity can be extracted from this analysis. This procedure

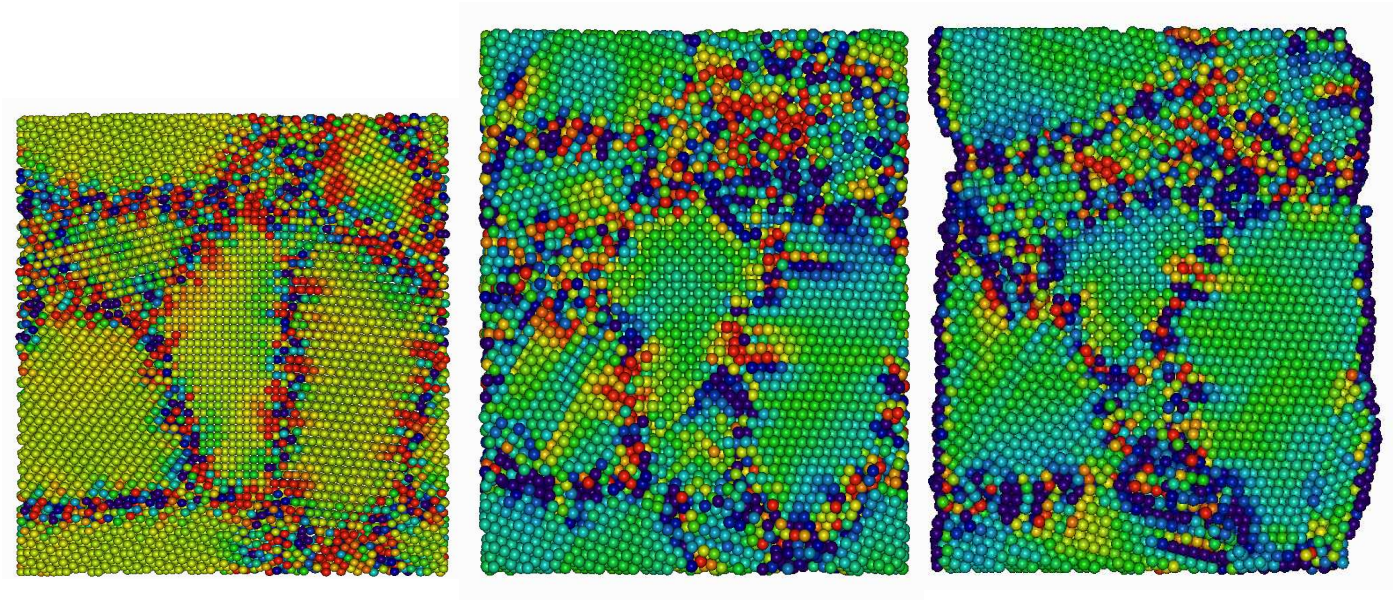

Fig. 4.4 A slice of the sample in the initial relaxed state (left) and deformed 15% with (right) and without free surfaces (center). Visualization performed according to the local hydrostatic stress state of each atom. The tensile axis is vertical. Interatomic potential 1 [18].

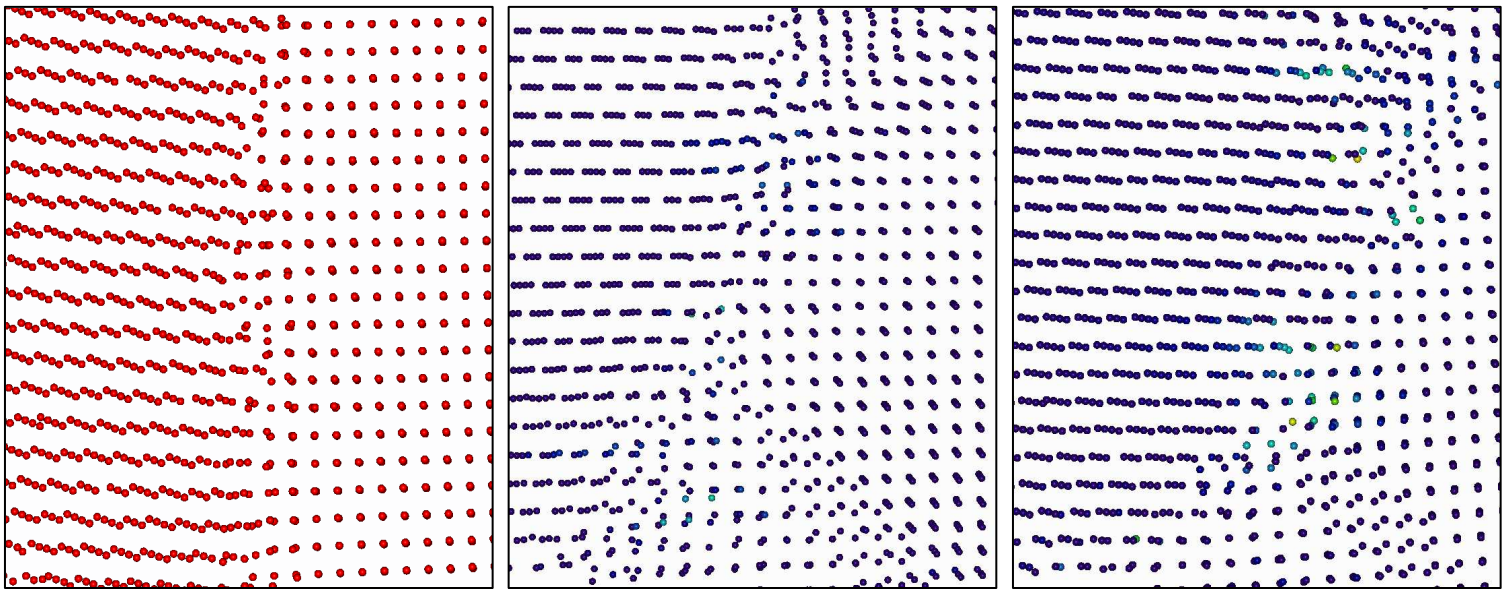

Fig. 4.5 Detailed region of a particular grain boundary motion, occurring with (right) and without (center) free surfaces in the sample. Note the simultaneous emission of a partial dislocation from this boundary, indicated by the stacking fault in the lower right part of the region shown. Interatomic potential 1 [18].

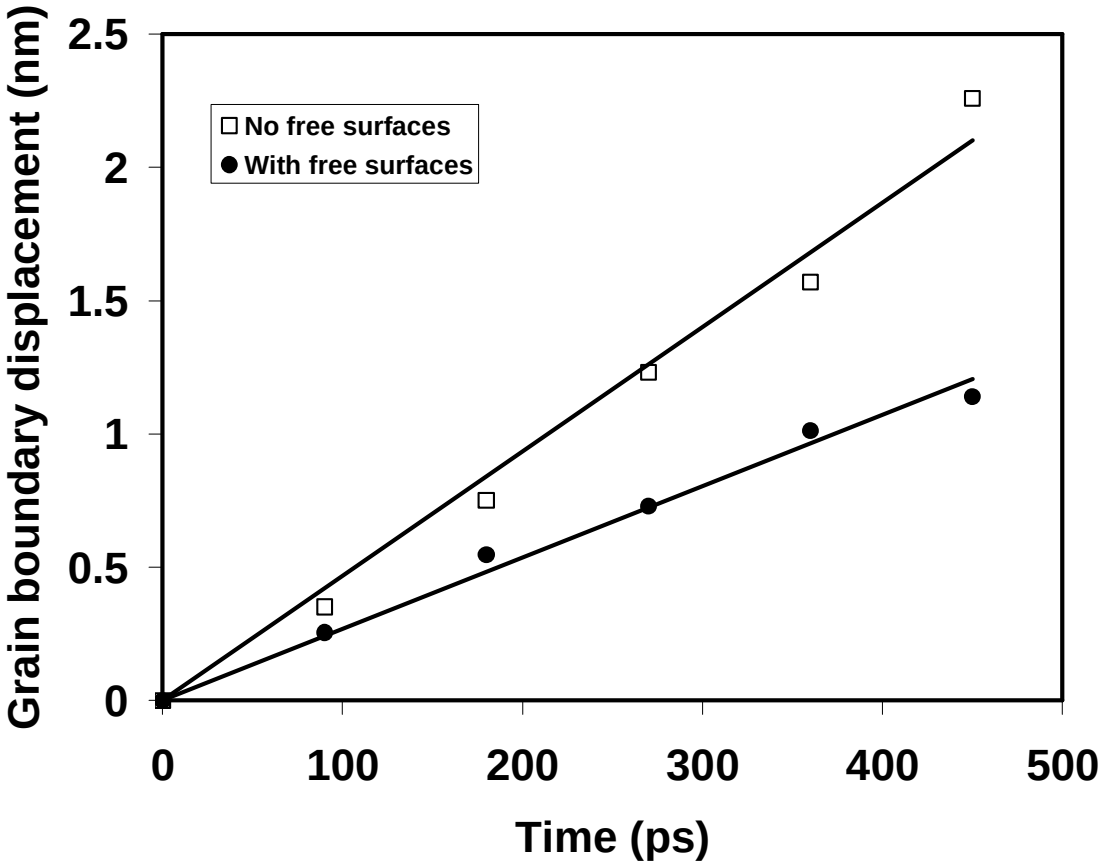

Fig. 4.6 Position of an individual boundary followed as the tensile test proceeds, with and without free surfaces for potential 1 [18]. The slopes of these curves allow the determination of the grain boundary velocity.

was repeated for sample slices taken both perpendicular and parallel to the tensile axis, with the aim of obtaining a statistically meaningful analysis of overall grain boundary migration in the samples.

Statistical analysis of grain boundary migration

Table 4.1: Average strain driven grain boundary velocities and corresponding standard deviations at room temperature

Sample conditions	Average Velocity (m/s),	Standard Deviation (m/s)
Potential 1 [18] no free surfaces	3.63	0.84
Potential 1 [18] with free surfaces	2.98	0.67
Potential 2 [19] no free surfaces	2.85	0.66
Potential 2 [19] with free surfaces	1.93	0.32

We found that the velocity of individual grain boundaries varied widely across the sample. For each tensile test and interatomic potential a statistical analysis of the grain boundary velocities was performed. The results are shown in Figure 4.7 in the form of histograms for the velocities of 25 boundaries monitored as a function of time for samples with and without free surfaces. Table 4.1 shows the average grain boundary velocities and corresponding standard deviations obtained for each case. Typically, the standard deviation observed is around 30% of the average velocity. The velocities observed in the simulation using the Voter potential [18] show higher values than those obtained using the Mishin potential [19]. This is consistent with a model where grain boundary migration is an integral part of the plasticity mechanism and the fact that the tests using

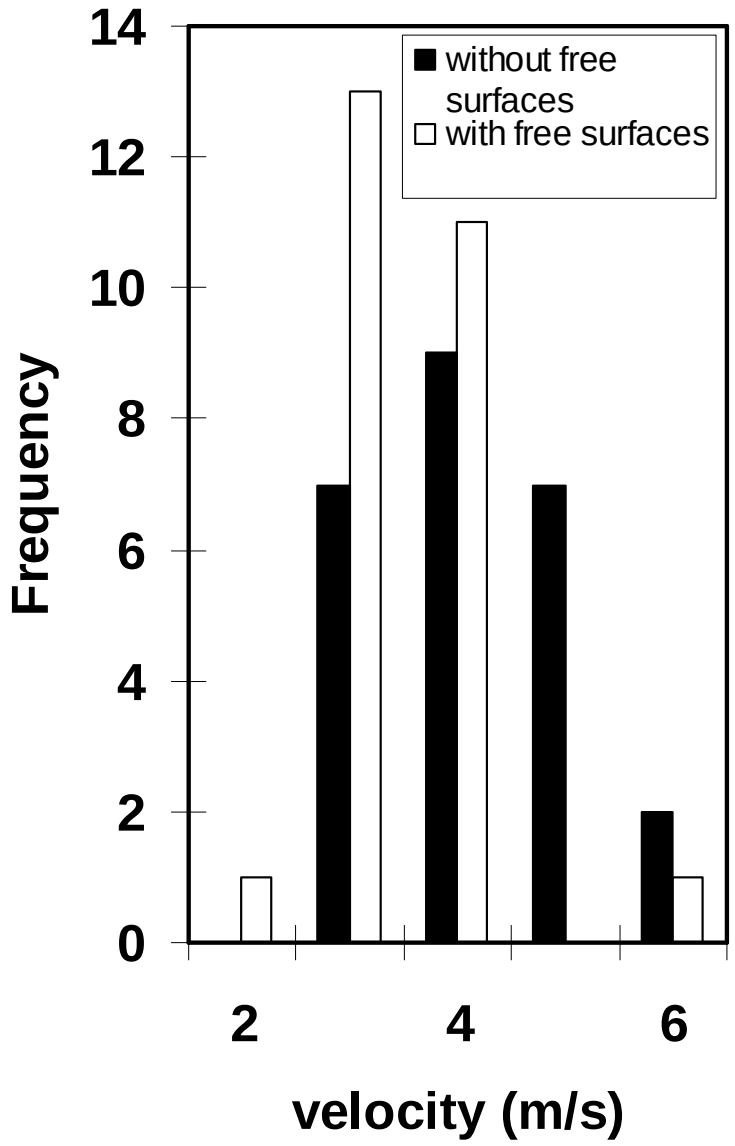

Fig. 4.7 Statistical analysis of the grain boundary velocities obtained for samples with and without free surfaces. Interatomic potential 1 [18].

the Voter-Chen potential 1 [18] show lower flow stresses than those run using the Mishin et al potential 2 [19].

The other essential result of our statistical analysis is that the samples containing free surfaces showed a lower average grain boundary velocity than the samples with no free surfaces. This trend is confirmed with both interatomic potentials used here. This is a surprising result since the presence of the free surfaces is expected to increase overall grain boundary plasticity, based on our results for flow stress observed in the stress strain curves. In previous simulation work [21] the presence of a free surface was found to increase grain boundary sliding, consistent with our flow stress results. The fact that grain boundary migration velocity is actually decreased by the presence of free surfaces is an unexpected result, and it points out to the need to separate grain boundary response in relative movement of the grains parallel to the grain boundary (sliding) and boundary movement perpendicular to itself (migration). Overall, grain boundary plasticity includes movement of the grains parallel to the boundary as well as grain boundary migration. The grain boundary velocities studied here and reported in Figure 4.7 and Table 4.1 refers to motion of the boundary mostly perpendicular to itself. The average velocity observed for this motion is decreased by the presence of the free surfaces. This is therefore not contradictory with increased grain boundary sliding in the samples with free surfaces, as will be shown below. Another important point is that the effects of the surface are expected to be most significant in the grains that are located at the edges of the sample and not to those in the center. The velocities reported in Table 4.1 refer to average velocities taken all across the sample. The sample studied here is large enough for overall

sample statistics but the total number of boundaries studied (25) is not enough to be divided into near surface and internal boundaries and still produce meaningful statistics.

Table 4.2: Average thermally driven grain boundary velocities and corresponding standard deviations, at various temperatures for potential 1[18].

Temperature (K)	Average Velocity (m/s),	Standard Deviation (m/s)
900	1.25	0.39
1000	3.61	1.01
1100	8.50	2.04
1200	10.71	2.41
1300	12.639	3.627
1450	21.146	7.992

For the strain rates studied here, the velocities obtained are of the order of m/s. These are high velocities for room temperature. For comparison of these results with purely thermal grain growth, we performed annealing treatments of the same sample at various temperatures and measured average grain boundary velocities as a function of temperature. Table 4.2 shows the results of this similar statistical analysis performed for grain boundary motion induced only by high temperature, under no applied strain or stress. The high temperature annealing treatments under no strain were performed using the Voter potential [18] and comparison of the results with the room temperature results under applied strain using the same potential show that a temperature in the range of 900 to 1000 K is necessary to induce velocities similar to those observed here under strain at

room temperature. This quantitative comparison further reinforces the point that the grain boundary mobility observed is indeed driven by the applied strain.

Grain boundary sliding

We analyzed grain boundary sliding occurring in the sample as a result of the deformation process. In particular this analysis was geared towards understanding the relationship between grain boundary sliding and migration. Two different techniques were used to visualize grain boundary sliding. In the first technique a small section of the initial undeformed sample is selected containing the grain boundary in question and in the shape that is rectangular in each of its two dimensional projections. The same atoms are then visualized in the deformed samples. Grain boundary sliding can be clearly observed as a step in the initially rectangular shape, located at the grain boundary. Figure 4.8 shows grain boundary sliding observed in this way for one particular boundary with and without free surfaces in the sample. The initial block of atoms selected for visualization, with no step in the boundary region is shown at left. After the 15% tensile deformation a step develops indicating grain boundary sliding, both with (center) and without (right) free surfaces in the sample. For most boundaries, we found that the sample containing the free surfaces resulted in more grain boundary sliding than the sample without free surfaces, as shown in the example of Figure 4.8. This technique gives a detailed picture of sliding for an individual boundary.

To obtain a picture of sliding in the entire sample, in the second visualization technique we constructed arrow plots of the plastic deformation of the overall sample.

This construction is obtained by plotting the differential displacement of each atom from the final deformed sample with respect to the initial sample that was deformed elastically

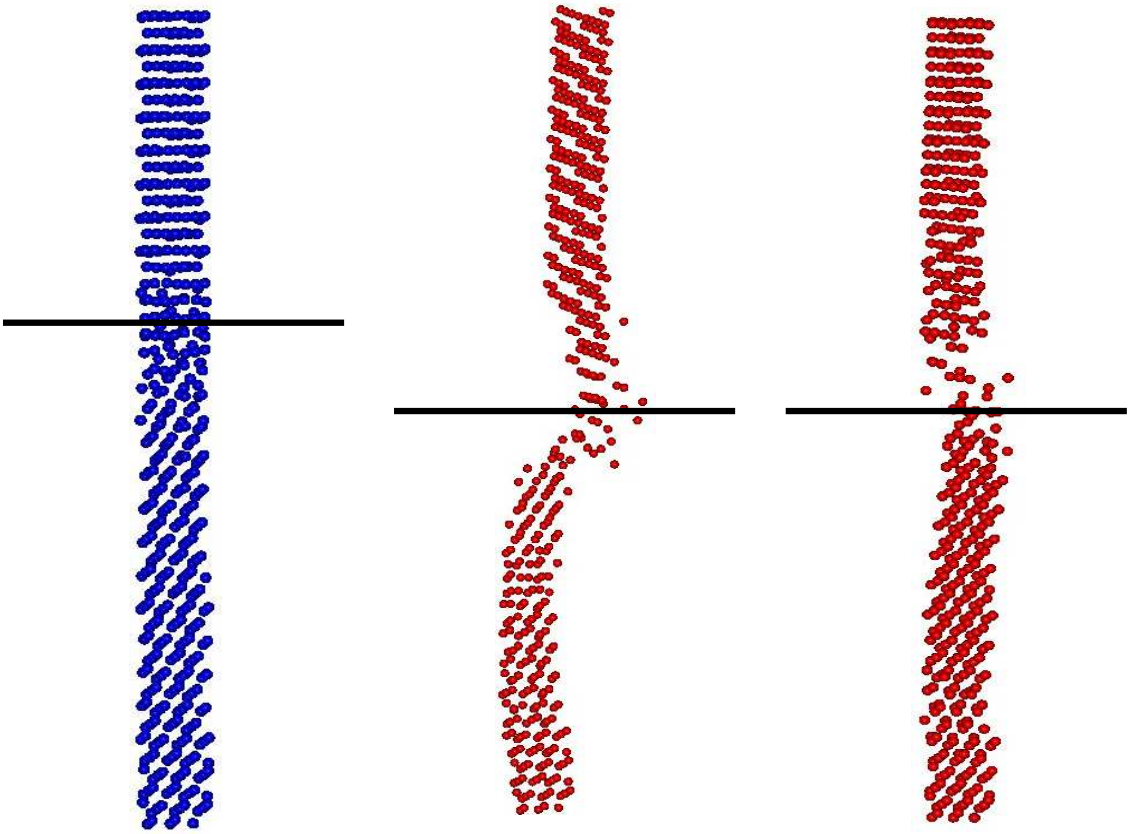

Fig. 4.8 Grain boundary sliding observed in one particular boundary with and without free surfaces in the sample. The initial block of atoms selected for visualization, with no step in the boundary region is shown at left. After the tensile deformation a step develops indicating grain boundary sliding, both with (center) and without (right) free surfaces in the sample. Interatomic potential 1 [18].

to the same dimensions of the deformed one. These differential displacements are a plot of the plastic events occurring in the sample. Dislocation mechanisms are seen as displacements inside the grains clearly occurring along slip planes, and are not common for the 5 nm grain size tested here, where most of the deformation occurs through grain boundary mechanisms. Figure 4.9 depicts an overall view of plasticity in the samples with and without free surfaces. The arrows depict the plastic displacement of each atom and the differential plots clearly show the extent of grain boundary sliding. This analysis again shows increased grain boundary plasticity for the sample with free surfaces. These results are consistent with what was found previously using stress controlled simulations, also in nanocrystalline Ni [21]. Increased grain boundary sliding due to the presence of free surfaces implies increased plasticity for samples with free surfaces, and is expected to result in lower flow stress. Indeed, the stress strain curves of Figure 4.1 indicate that for both interatomic potentials used here, the presence of the free surfaces lowers the flow stress. Our results suggest that grain boundary sliding is the most important grain boundary mechanism controlling the flow stress. Sliding is aided by the presence of free surfaces, but as mentioned above the free surfaces do not result in increased migration of the boundaries. On the contrary, grain boundary migration is reduced by the presence of free surfaces, even though sliding is increased.

Grain rotation and coalescence

We have found that the process of grain boundary sliding and migration is also accompanied by grain rotation and grain coalescence. Figure 4.10 shows the rotational

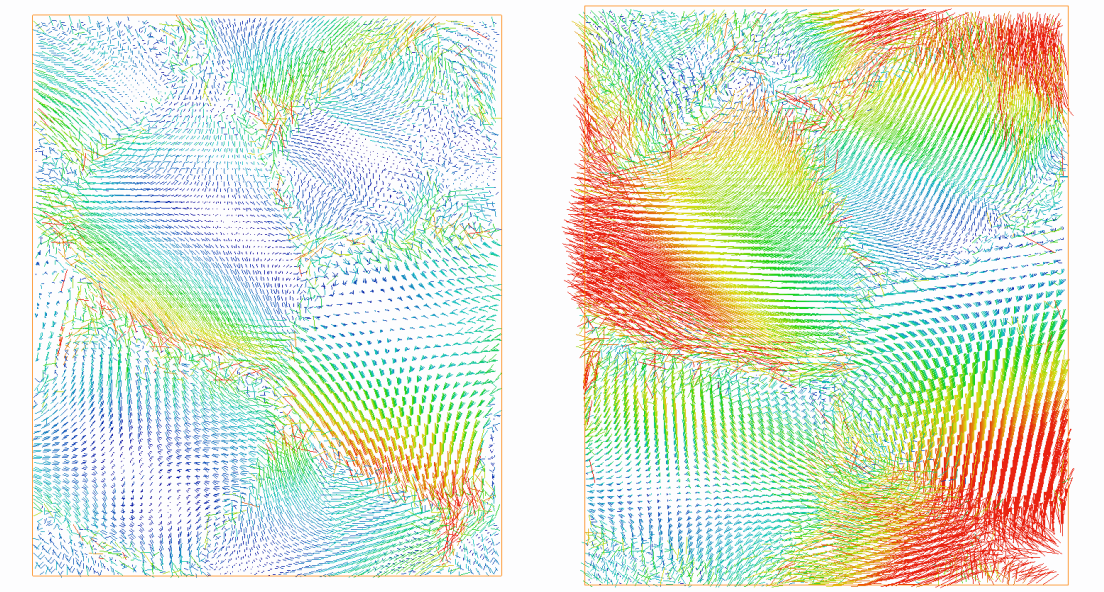

Fig. 4.9 Overall view of plasticity in the samples with and without free surfaces. The Arrows depict the plastic displacement of each atom. Note increased grain boundary plasticity for the sample with free surfaces. Interatomic potential 1 [18] and the tensile axis is vertical.

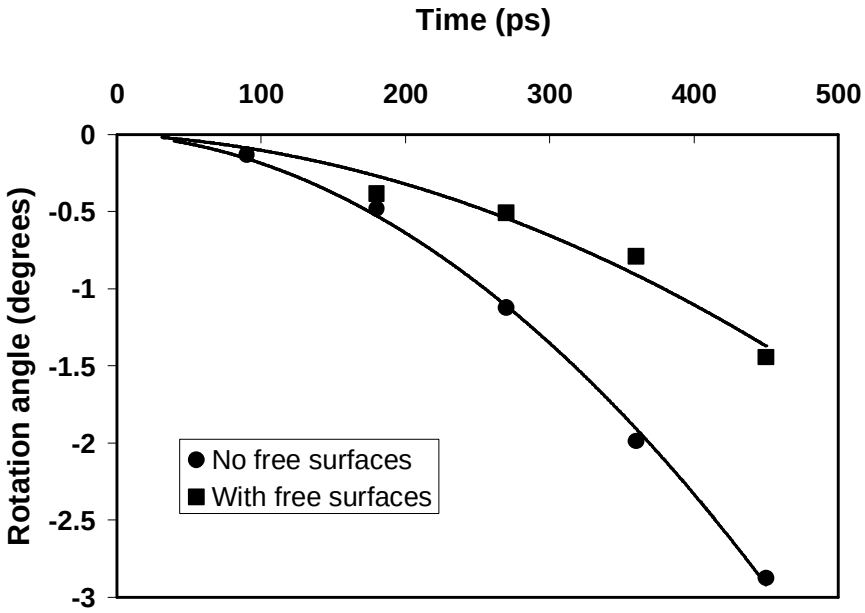

Fig. 4.10 Rotation of the central grain of the samples observed with and without free surfaces. Interatomic potential 1 [18].

changes of the central grain of the samples observed with and without free surfaces. For this central grain the rotation observed is decreased in the samples with free surfaces. We have also found that the grains can coalesce, a phenomenon that we observed qualitatively to occur more in the sample with free surfaces. An example is depicted in Figure 4.11 for a particular boundary of the sample with fee surfaces. The lines indicate the orientation of compact (111) planes in both grains. As the tensile deformation proceeds, the grains rotate and coalesce. Qualitative observation of this phenomenon indicates that it occurred preferentially in grains neighboring the free surfaces.

4.4 Discussion and Conclusions

The evolution of polycrystalline microstructures under no applied stress occurs in a thermally activated process and is commonly described in terms of grain boundary migration. These microstructures can also evolve by grain rotation because the excess energy of a polycrystalline body is the product of the grain boundary area and the grain boundary energy. This means that either motion of the boundary to reduce its total area or grain rotation to reduce the boundary energy per unit area can reduce the energy of the system. One can therefore understand that under annealing conditions, microstructures will evolve by a combination of grain boundary migration and grain rotation.

Stress-assisted microstructural evolution can not be explained by these traditional driving forces and other possible mechanisms need to be considered. It is expected that the grain boundary response to applied stress will primarily be grain boundary sliding or

movement of the grains as a rigid body in directions parallel to the grain boundary. For example, in the case of low-angle boundaries that can be described in terms of dislocation

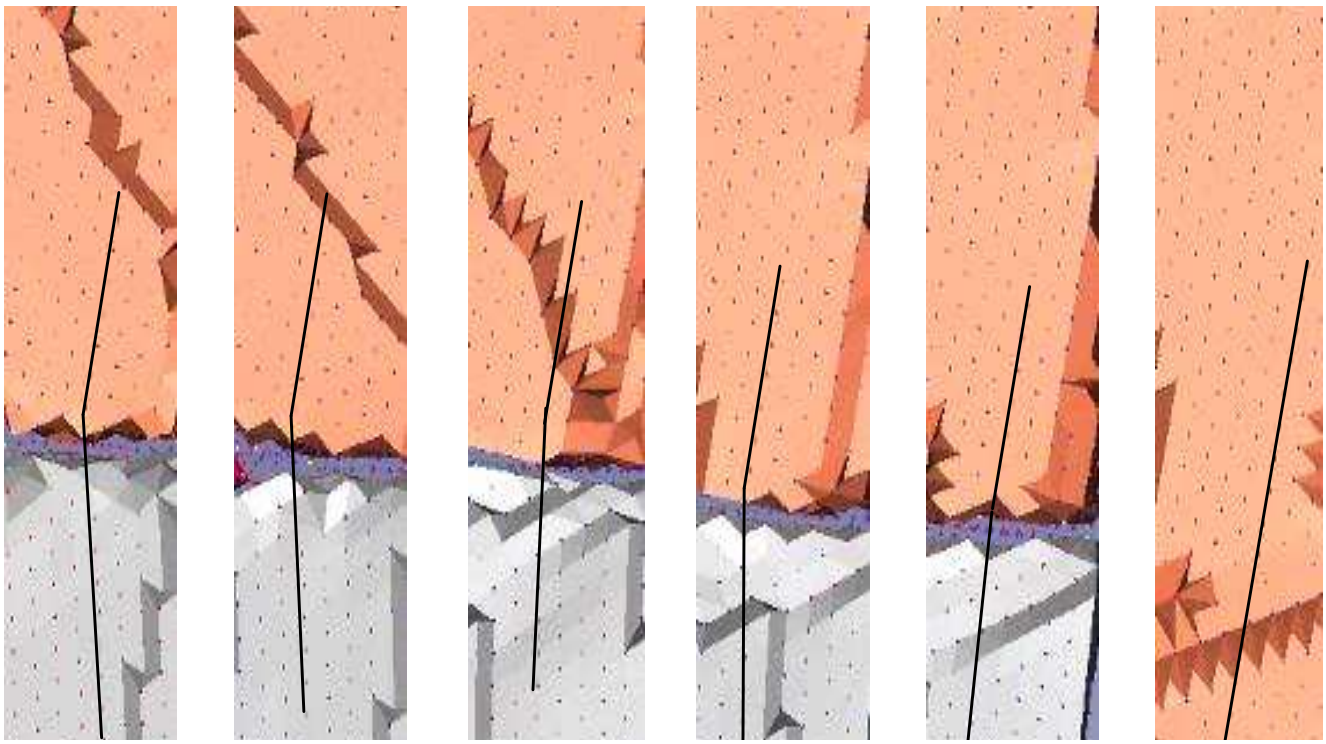

Fig 4.11 Observed grain coalescence in a particular boundary of the sample with fee surfaces, The lines indicate the orientation of compact (111) panes in both grains. As the tensile deformation proceeds, the grains rotate and coalesce.

arrays, the shear stresses influence these boundaries by acting on the individual dislocations in these arrays. In the case of high-angle grain boundaries that can be described in terms of coincident site lattices, the sliding mechanisms act through the motion of secondary grain boundary dislocations present in the structure or nucleated due to the applied stress. In this case, the sliding of the boundary produces a simultaneous coupled motion of the boundary perpendicular to itself. Cahn and Taylor [22] developed a unified approach to grain boundary motion pointing out that normal motion of a grain boundary can result from a shear stress applied tangential to it. In other words, grain boundary sliding and grain boundary migration are coupled phenomena. Cahn and Taylor [22] postulate that almost any motion of an interface between two crystals can produce a coupled tangential motion of the two crystals relative to each other which is proportional to the normal motion of the interface. Such translations can also produce grain rotations. Normal motion of a grain boundary resulting from a shear stress applied tangential to it which results in tangential motion and its converse. We postulate that the stress-assisted grain boundary mobility observed in the present study is in part due to this mechanical coupling. The magnitude of the grain boundary migration velocities observed in this study indicates how significant this coupling can be in producing microstructure evolution during deformation.

Grain boundary sliding, migration and rotation occur simultaneously as a response to the applied strain. The absolute values of the rotation, sliding and migration rates depend on the particular boundary, giving a distribution of migration velocities, as shown in our results. Grain boundary sliding appears to be the primary mechanism controlling the flow stress and grain boundary migration can be interpreted as result of

the mechanical coupling of the sliding and migration components. Our results also show that the relative importance of these effects is significantly affected by the presence of free surfaces. The presence of free surfaces increases grain boundary sliding but decreases the coupling coefficient between sliding and migration, resulting in lower migration velocities. It is also possible to hypothesize that there are two different mechanisms in which grain boundaries can slide; one is through grain boundary dislocations that produces a coupled migration of the boundary and one that is controlled by the migration of free volume available in the boundary, not involving coupled migration. The latter mechanism is described in detail in reference 20 and can be expected to be significantly enhanced by the presence of free surfaces because the intersection of the boundaries with the free surfaces can provide a source of free volume. The former mechanism is described in references 23 and 24 and implies coupling between sliding and migration.

Finally, we note that recent molecular dynamics simulations of a circular grain embedded in an otherwise single-crystal matrix have also shown that grain boundary migration and grain rotation occur simultaneously. In this case, it was found that the rate of rotation decreases with increasing grain size. A picture emerged where, for nanocrystalline materials under large strains, grain boundary sliding, grain boundary migration, grain rotation and coalescence can all occur simultaneously.

4.5 Acknowledgments

This work was supported by NSF, Materials Theory. We acknowledge helpful discussions with Helena van Swygenhoven and Julia Weertman. The simulations were performed using System X, Virginia Tech's supercomputer.

4.6 References

[1] D. Farkas, S. Mohanty, and J. Monk. MSE&A, Accepted May 2007.
[2] J.R. Weertman, D. Farkas, K. Hemker, H. Kung, M. Mayo, R. Mitra, H. Van Swygenhoven, MRS Bulletin 24 (1999) 44
[3] J. Schiotz and K. Jacobsen, Science 301 (2003) 1357
[4] J. Schiotz, T. Vegge, F. Tolla, K. Jacobsen, Physical Review B 60 (1999) 19711
[5] J. Schiotz, Scripta Mater. 51 (2004) 837
[6] H. Van Swygenhoven, M. Spaczer, A. Caro, et al. Physical Review B 60 (1999) 22
[7] H. Van Swygenhoven, A. Caro, D. Farkas, Mater. Sci. and Eng. A309-310 (2001) 440
[8] D. Farkas and W.A. Curtin, Mater. Sci. and Eng. A412 (2005) 316
[9] A.J. Haslam, D. Moldovan, V. Yamakov, D. Wolf, S.R. Phillpot, H. Gleiter, Acta Mater. 51 (2003) 2097
[10] A.J. Haslam, S.R. Phillpot, H. Wolf, et al. Mater. Sci. and Eng. A318 (1-2) (2001) 293-312
[11] Z.W. Shan, E.A. Stach, J.M.K. Wiezorek, J.A. Knapp, D.M. Follstaedt, S.X. Mao, Science 305 (2004) 654.
[12] K. Zhang, J.R. Weertman, J.A. Eastman, Appl. Phys. Lett. 85 (2004) 5197
[13] M. Jin, A.M. Minor, E.A. Stach, J.W. Morris, Acta Mater. 52 (2004) 5381
[14] K. Zhang, J.R. Weertman, J.A. Eastman, Appl. Phys. Lett. 87 (2004) 061921
[15] J. Schiotz, Mater. Sci. Eng. A375-377 (2004) 975
[16] H.Q. Li , Advanced Engineering Materials 7 (2005) 1109-1110
[17] D. Farkas, S. van Petegem, H. Van Swygenhoven, Scripta Mat. 55 (2006) 695
[18] A.F Voter and S. F. Chen, MRS Symposia Proceedings 82 (1987) 175
[19] Y. Mishin, M. Mehl, D. Farkas, D. Papaconstantopoulos, Phys. Rev. B 59 (1999) 3393
[20] S. J. Plimpton, J. Comp. Phys. 117 (1995) 1
[21] P. Derlet and H. van Swygenhoven, Phil. Mag. A 82 (2002) 1-15
[22] J. W. Cahn, Y. Mishin, A. Suzuki, Phil. Mag. A 86 (2006) 3965–3980
[23] B. Hyde, D. Farkas, M.J. Caturla, Phil. Mag. 85 (2005) 3795-3807
[24] J.W. Cahn and J.E. Taylor, Acta Mater. 52 (2004) 4887-4898
[25] M. Upmanyu, D.J. Srolovitz, A.E. Lobkovsky, et al. Acta Mater. 54 (2006) 1707-1719

CHAPTER 5: Strain-induced grain growth and rotation in Nickel nanowires [1]

Virtual tensile tests of nanocrystalline nickel wires of initial 5 nm grain size were simulated at strain rates varying from 3 x10^{7} s^{-1} to 1 x 10^{9} s^{-1} at 300 K, reaching deformation levels up to 36%. The virtual tensile tests allowed the study of the strain rate sensitivity of these nanowires, yielding an activation volume of ~2*b*3, where *b* is the Burger's vector, consistent with grain boundary mechanisms of plasticity. Most importantly, after 3% deformation the grain size increased significantly during the deformation, with larger grains growing at the expense of the smaller ones as the deformation levels increase. The volume of each grain was monitored as a function of time and stress level. The results clearly indicate that the observed grain growth is stress driven, with grain size versus stress behavior being only weakly dependent on the strain rate and simulation time. Grain growth is also accompanied by grain rotation. The observations are interpreted in terms of the coupling of the relative motion of the grains parallel to the boundary and the motion of the boundary in the direction perpendicular to itself. Our results are consistent with a model where the deformation is accommodated by grain boundary sliding which in turn is coupled with grain boundary migration and rotation, producing grain growth.

5.1 Introduction

The properties of nanocrystalline metals have been a focus for computational materials scientists in recent years [2–9]. The capabilities of massively parallel computers have allowed large scale atomic level simulations of deformation behavior of materials with features at the nanoscale. Simulation work is critical in understanding the underlying

mechanisms of plastic deformation at different strain rates, grain sizes, and structures. Molecular dynamics has been utilized in this kind of simulation, with the limitation of the small sizes and extremely fast strain rates that are imposed by the computational resources. Nanocrystalline structures are of particular interest because of their increased hardness and because of the appearance of particular phenomena at the nanoscale such as the reversal of the Hall-Petch effect [2].

One particular observation in the deformation behavior of nanocrystalline materials has been the fact that nanograins are experimentally seen to grow as they are deformed. Several investigators have found experimental evidence of significant grain growth and rotation at room temperature for these small grain sizes at high deformations [10,13]. In the experimental studies, it is difficult to determine the role of thermally activated processes in the observed grain growth, since there may be questions regarding the actual local temperature of the sample and whether there is actually enough time for thermally activated growth to occur. Stress enhanced grain boundary mobility was also observed in simulations [9,14].

In this work, we report simulation studies of the deformation of polycrystalline Ni nanowires carried out at different strain rates and controlled room temperature. Under these conditions we can study the grain growth process by monitoring the evolution of the volume of individual grains. This process, repeated for various strain rates allows us to separate stress driven growth from any time-dependent contribution.

Analysis of the simulation results show that the growth process is fundamentally driven by the stress.

5.2 Simulation Technique

The virtual tensile tests simulations were performed using a conventional molecular dynamics (MD) algorithm to rescale the coordinates along the *z* direction. The interaction between the atoms is modeled using an embedded-atom method (EAM) potential developed by Voter and Chen for nickel [15]

The sample was prepared in two steps. Initially a cubic sample of 22 nm side was prepared using a Voronoi construction with an average grain size of 8 nm [6,7]. A cylindrical shape with dimensions of 22 nm long and a five nm radius was then cut from the initial cube. The initial nickel cube had a grain size of ~8 nm, but the five nanometer radius cut from the cube resulted in a 170 000 atom sample with ~5 nm average grain size. To allow a meaningful comparison of the results obtained at different strain rates, all mechanical tests were performed using the same virtual nanowire sample, with the same grain structure.

The code used to run the MD tensile tests is LAMMPS and was developed by Plimpton [16] The technique uses a Nose-Hoover thermostat and barostat to control the temperature and pressure. The sample was first equilibrated for 450 ps with periodicity along the wire axis and free surfaces parallel to the wire axis, with the temperature set at 300 K. After the initial relaxation, the periodicity along the *z* axis was increased at various rates to simulate an increasingly strained wire. The value of the stress in the direction of the wire axis was monitored to obtain the stress-strain behavior at various strain rates. As the deformation proceeds, snapshots of the sample were created for visualization.

5.3 Results

Figure 5.1 shows the nanowires after 0, 90, and 270 ps, deformation (0, 12, and 36% strain, respectively) for a strain rate of 1.33×10^9 s^{-1}. The various grains are color coded, showing significant grain growth, as the deformation proceeds. For the largest deformation, the figure also shows a slice through the center of the wire color coded according to the Centro symmetry parameter [17], visualizing stacking faults and twins in the deformed structure. Very few of these defects are seen, even at the large strain of 36%, indicating that the main deformation mechanisms are grain boundary mediated. Most importantly, significant grain boundary motion is clearly seen, as the deformation proceeds. The corresponding stress strain curve is shown in Figure 5.2, together with the results of tests at various other strain rates. Figure 5.2 shows the strain stress curves up to 5% deformation, a region that includes plastic deformation but not the higher deformation levels where the sample develops necking.

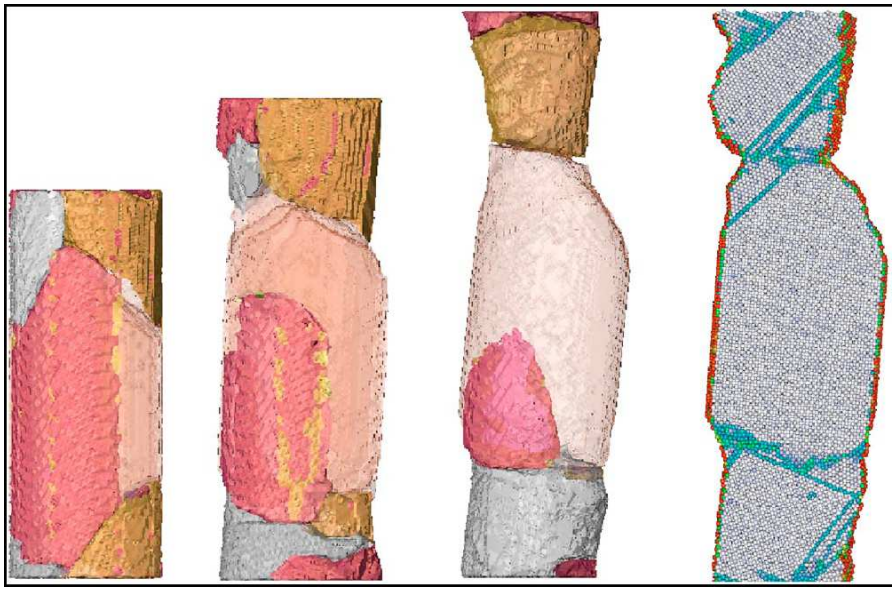

Fig. 5.1 Virtual tensile test of a multigrained nickel nanowire. Snapshots at 0, 12, and 36% strain, colored according to grains. The strain rate is 1.33 x 10^9 s^{-1}. The figure at right shows a slice through the wire deformed 36% colored according to the Centro symmetry parameter, visualizing stacking faults and twins in the deformed structure.

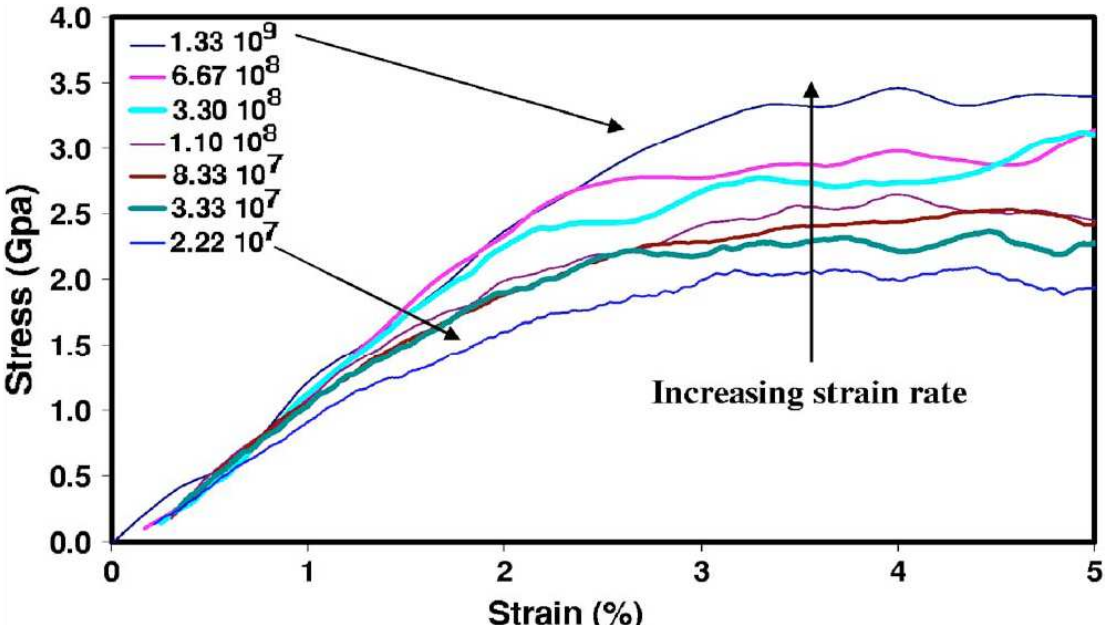

Fig. 5.2 Stress strain curves for varying strain rates from 1.33 x 10^9 s^{-1} to 2.22 x10^7 s^{-1} at 300 K.

The stress strain curves show flow after deformation of about 3%, with the flow stress decreasing for slower strain rates. To quantify the dependence of the flow stress on the strain rate, the strain rate sensitivity exponent was calculated by plotting the average flow stress over the strains of 3% to 5% as a function of the strain rate. The results are shown in Fig. 5.3 giving the strain rate sensitivity exponent of 0.121 for the ~5 nm grain sized nanowire. The activation volume for the deformation process [18–21] can be calculated from this exponent, as follows:

$$\nu^* = \frac{\sqrt{3}kT}{n\sigma} \qquad \textbf{Equation 5.1}$$

where n is the stress sensitivity exponent, k is Boltzmann's constant, T is the temperature, and σ is the flow stress. Using a flow stress value of 2.0 GPa and the temperature of 300 K we obtain 0.029 nm^3 or $1.878b^3$, where b is the Burger's vector value of 0.25 nm [14,16]. A value of $1–2b^3$ for a grain size of ~5 nm suggests that the deformation mechanisms involves only a few atoms motion at a time, as expected in grain boundary accommodation mechanisms. Indeed, grain boundary mechanisms of plasticity have been postulated for grain sizes smaller than 20 nm, based on extensive simulation work[2–7]. In recent experimental work [18–21] the apparent activation volume was found to be $20b^3$ for nickel with a grain size of 30 nm, indicating dislocation mediated plasticity. Our result for the activation volume is consistent with the expected relation between activation volumes and grain sizes [18–21].

For additional confirmation of a grain boundary sliding mechanism operating, we studied the detailed atomistic structure of the deformed samples to observe dislocations at a strain rate of 1.33×10^9 s^{-1}. It was found that the number of dislocations emitted was small, less than 15 total dislocations at 15% strain confirming that localized

accommodation in the grain boundaries is the main mechanism of plasticity at these small grain sizes.

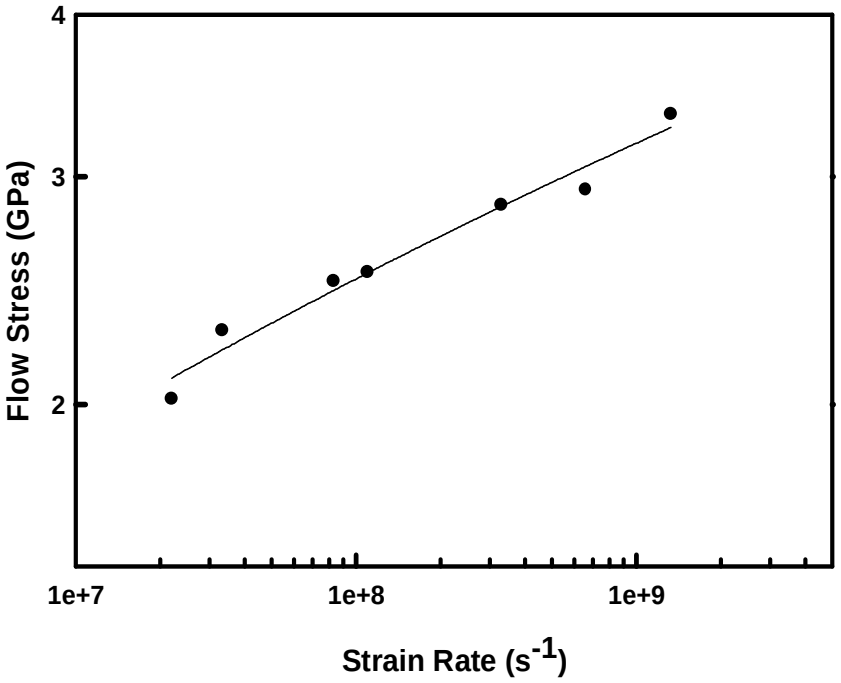

Fig. 5.3 The flow stress, defined from 3% to 5% strain, for strain rates varying from 2.22 x 10^7 s^{-1} to 1.33 x10^9 s^{-1}. **Both scales are logarithmic**.

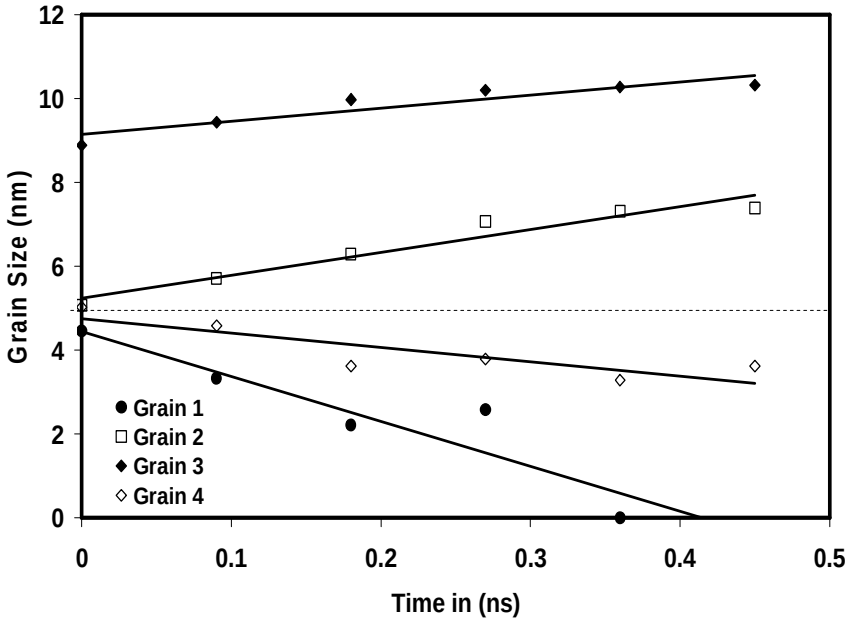

Fig. 5.4 Size of four individual grains, followed as a function of time for a strain rate of 1.33 x10^9 s^{-1}. The dotted line is the initial average grain size and the sizes indicated are measured as the cubic root of the grain volume.

To study the observed grain growth process, we measured the volumes of the individual grains as the deformation preceded at different strain rates. As an example, Fig. 5.4 shows grain size versus time for four representative grains deformed at a strain rate of $1.33 \times 10^{9}\ s^{-1}$. In this and subsequent figures the cubic root of the volume is used as a measure of grain size. The larger grains are seen to grow at the expense of the smaller ones, a trend that was also observed for other strain rates. The initially larger grains continue to grow at the expense of smaller grains which reduce and often disappear [13]. As a result of grain growth the average grain size for all grains grew as a function of time for each of the strain rates. This is shown in Fig. 5.5(a), which shows the average grain size, linearly increasing over time for each strain rate. The growth rate observed for the different strain rates is very different, indicating that the growth process is controlled by the strain level, more than the time of the simulation. Figure 5.5(b) shows the data obtained for various strain rates, plotted as a function of strain. This figure also shows that the growth process is strongly correlated with the overall strain of the sample. The comparison of the plots of grain growth as a function of time and strain suggests that the growth process is not a thermally activated process, but rather an integral part of the mechanism of grain boundary plasticity in nanocrystalline materials. In this way the present simulations help address the controversy surrounding some experimental observations [11].

Although grain growth is well recorded for increasing temperature, only recently has grain growth been experimentally observed at room temperature and postulated as due to strain [10–14]. In simulation work, Schiotz *et al* [14] used a 5 nm diameter copper sample with a 10% to −10% strained cyclic deformation and observed grain coarsening

that was induced by strain. That work was performed under cyclic loading as opposed to tensile conditions. The present results, obtained at various strain rates clearly show that grain coarsening operates as part of the basic plasticity mechanism in nanocrystalline materials. We have also analyzed the virtual tensile test for evidence of grain rotation and have found significant grain rotation during the deformation process. Grain rotation for the central grain in the wire was quantified for the various strain rates tested. Figure 5.6 shows the values observed for the rotation for this particular grain in the plane perpendicular to the tensile axis as a function of time. The data show that the grain rotation speed varies significantly with strain rate, indicating again that it is not a time controlled thermal process and is mostly driven by the strain itself.

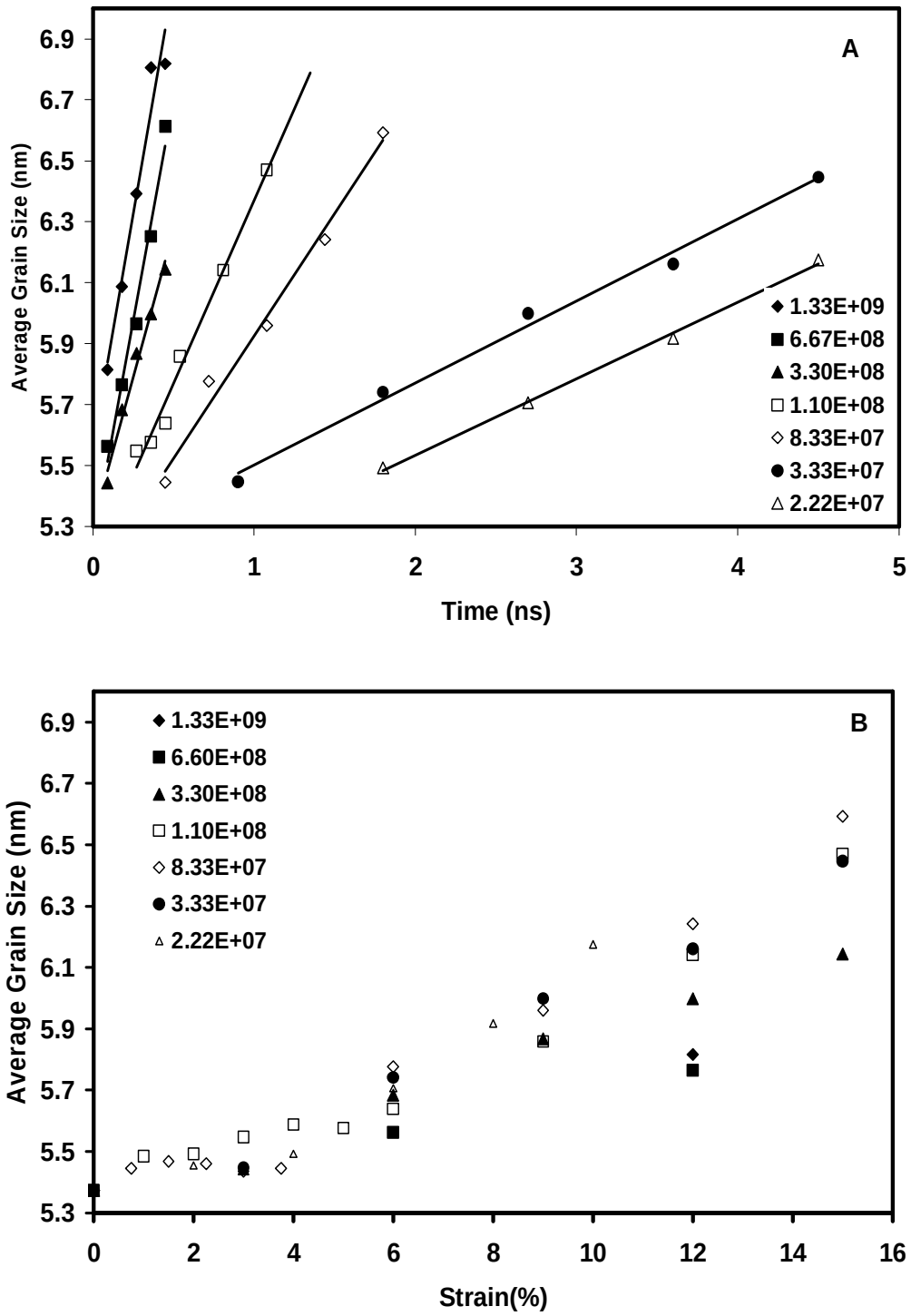

Fig. 5.5 (a) Average grain size as a function of time for different strain rates. (b) Average grain size as a function of strain for different strain rates. Average grain sizes are measured as the cubic root of the average grain volume and the strain rates are indicated in s^{-1}.

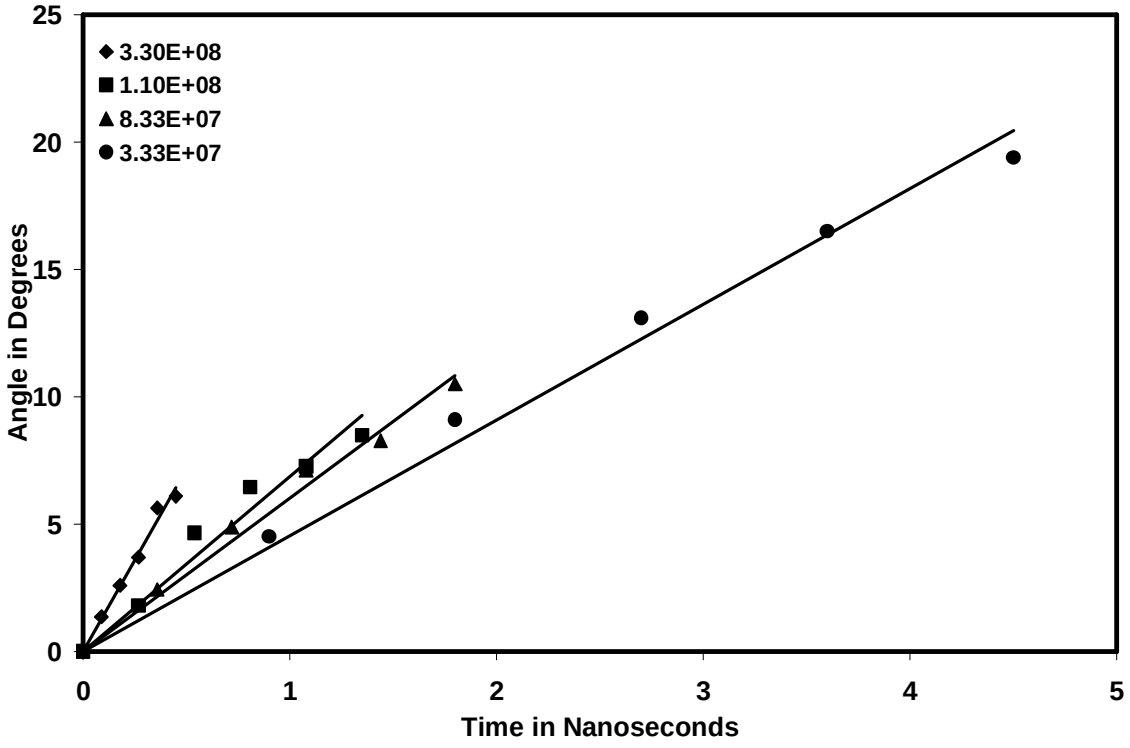

Fig. 5.6 Rotation angle of a sample grain in the center of the wire as a function of time for different strain rates, indicated in s^{-1}.

5.4 Discussion

Our simulations show that grain boundary motion and rotation are present as basic deformation mechanisms in these nanowires, as have been observed in several experimental studies of the mechanical response of nanocrystalline metallic materials. The most likely mechanism responsible for the strain-driven grain growth in our simulations arises from the GB sliding that accommodates the strain. The present results can be interpreted as due to the coupling between the parallel and perpendicular motions of the grain boundary, as described by Bishop *et al* [22]. More recently, Hyde, Farkas, and Caturla [23] analyzed the motion of a particular $\sum$=5 grain boundary subject to shear in Fe and found that the boundary moved through the nucleation and motion of displacement shift complete (DSC) lattice dislocations. This produced not only relative motion of the grains parallel to the boundary but also motion of the boundary in the direction perpendicular to itself, as a result of the same unique process. Cahn, Mishin, and Suzuki [24] analyzed the atomic mechanisms of grain boundary motion for a large number of boundaries and similarly found a coupling of the motion parallel and perpendicular to the boundary when the boundary is subject to stress. In that work, they analyzed a series of boundaries and studied the values for the coupling coefficient $\beta = s/m$ where s is the relative movement of the grains parallel to the boundary (sliding) and m is the movement of the boundary in the direction perpendicular to itself (migration). They found values for β that range from 0.3 to 1.5.

For the interpretation of the present results, a simple model can be constructed assuming that:

(i) A tensile strain _ is the result of a shear strain of $\varepsilon/\cos(45°)$ for each grain.
(ii) The deformation is accommodated by sliding of the boundaries, denoted by *S*.

(iii) This movement *S* produces a coupled migration of the boundary denoted by *m*.
(iv) Sliding in opposite directions for opposite sides of a grain also results in coupled grain rotation.

Using these assumptions (Figure 5.7) the average sliding for each boundary can be calculated as the average grain radius times the average shear deformation of each grain or:

$$S = R\sqrt{2}\varepsilon \qquad \textbf{Equation 5.2}$$

where *R* is the average radius of a grain. Using this equation we obtain an average displacement of the boundary parallel to itself of (4.2ε) in nm. Analysis of the data in Fig. 5.5(b) yields an average grain growth of (6ε) in nm, or an average movement of the boundary perpendicular to itself *m* of half that value, (3ε) in nm. This means that our results imply a coupling factor $\beta = s/m$ of 1.3 consistent with the values reported by Cahn, Mishin, and Suzuki [24]. In addition, if opposite sides of a grain slide in different directions, a net grain rotation will result which we can estimate in radians as

$$\theta = \frac{S}{R} \qquad \textbf{Equation 5.3}$$

Substitution of *S* from Eq. 5.2 gives a grain rotation of 1.41ε in radians, or about 12° for a 15% deformation. This value can be compared to our observed values for 15% deformation which range from 7 to 18°.

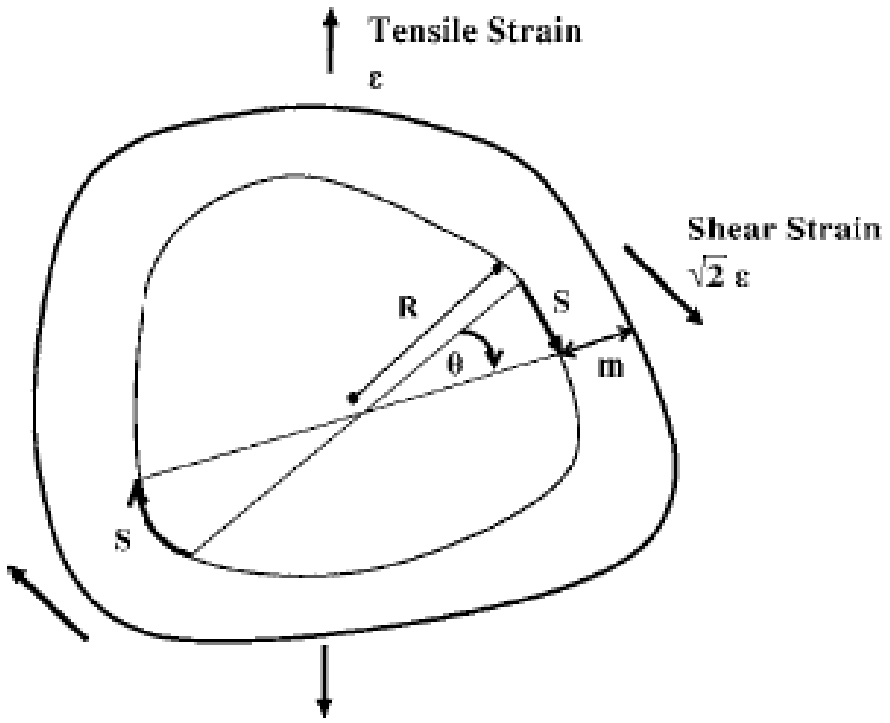

Fig. 5.7 Schematics of coupled sliding, migration, and rotation for an average grain in the sample.

Therefore, the present results for grain growth can be consistently interpreted as resulting from the coupled motion of the grain boundaries. The observed grain rotation is also consistent with a picture where deformation occurs through grain boundary sliding, occurring through the motion of grain boundary dislocations, which in turn results in grain rotation and grain growth. Figure 5.7 shows a schematic of the process, depicted for an average growing grain. This process can have general validity as long as the grain boundary migration of each grain satisfies compatibility conditions. The compatibility conditions can be easily satisfied for small nanowire configurations such as the one studied here but can impose additional constrains in a different configuration. In addition, the effects of the free surfaces in the nanowire can be significant. For example, Derlet and Van Swygenhoven [25] have shown that the presence of the free surface increases grain boundary sliding. One should also bear in mind that the present results were obtained for only one nanowire diameter and grain structure. These effects may change the magnitude of the observed grain growth but the basic nature of the coupling effects discussed here is expected to be of more general validity and possibly extend to polycrystalline materials with grain sizes in the nanometer range. Indeed, grain boundary migration driven by the strain was found in simulations performed for nanocrystalline Ni of 5 nm grain size without free surfaces. These results are reported in a recent paper,[26] where significant growth of particular grains at the expense of others is shown.

5.5 Acknowledgements

This work was supported by NSF, Materials Theory. We acknowledge helpful discussions with H. Van Swygenhoven and Y. Mishin. This work was performed using Virginia Tech's System X supercomputing facility.

5.6 References

[1] J. Monk and D. Farkas. Physical Review B **75** 045414 (2007)
[2] J. R. Weertman, D. Farkas, K. Hemker, H. Kung, M. Mayo, R. Mitra, and H. Van Swygenhoven, MRS Bull. **24**, 44 (1999)
[3] J. Schiotz and K. Jacobsen, Science **301**, 1357 (2003)
[4] J. Schiotz, T. Vegge, F. Tolla, and K. Jacobsen, Phys. Rev. B **60**,11971 (1999)
[5] J. Schiotz, Scr. Mater. **51**, 837 (2004)
[6] H. Van Swygenhoven, M. Spaczer, A. Caro, and D. Farkas, Phys.Rev. B **60**, 22 (1999)
[7] H. Van Swygenhoven, A. Caro, and D. Farkas, Mater. Sci. Eng.,A **309**, 440 (2001)
[8] D. Farkas and X. Curtin, Mater. Sci. Eng., A **412**, 316 (2005)
[9] A. J. Haslam, D. Moldovan, V. Yamakov, D. Wolf, S. R. Phillpot,and H. Gleiter, Acta Mater. **51**, 2097 (2003)
[10] E. Ma, Science **305**, 623-624 (2004)
[11] Z. W. Shan, E. A. Stach, J. M. K. Wiezorek, J. A. Knapp, D. M. Follstaedt, and S. X. Mao, Science **305**, 654 (2004); see also M.W. Chen and X. Yan, *ibid.* **308**, 356 (2005); Z. W. Shan, E. A.Stach, J. M. K. Wiezorek, J. A. Knapp, D. M. Follstaedt, and S.X. Mao, Science **308**, 5720 (2005)
[12] Kai Zhang, J. R. Weertman, and J. A. Eastman, Appl. Phys. Lett. **85**, 5197 (2004)
[13] Kai Zhang, J. R. Weertman, and J. A. Eastman, Appl. Phys. Lett.**87**, 061921 (2005)
[14] J. Schiotz, Mater. Sci. Eng., A **375-377**, 975 (2004)
[15] A. F Voter and S. F. Chen, Mater. Res. Soc. Symp. Proc. **82**, 175 (1987)
[16] S. J. Plimpton, J. Comput. Phys. **117**, 1 (1995)
[17] C. L. Kelchner, S. J. Plimpton, and J. C. Hamilton, Phys. Rev. B **58**, 11085 (1998)
[18] R. J. Asaro and S. Suresh, Acta Mater. **53**, 3369 (2005)
[19] L. Lu, R. Schwaiger, Z. W. Shan, M. Dao, K. Lu, and S. Suresh, Acta Mater. **53**, 2169 (2005)
[20] Y. M. Wang and E. Ma, Mater. Sci. Eng., A **375**, 46 (2004)
[21] Y. M. Wang, A. V. Hamza, and E. Ma, Appl. Phys. Lett. **86**,241917 (2005)
[22] G. H. Bishop Jr., R. Harrison, T. Kwok, and S. Yip, J. Appl. Phys.**53**, 5596 (1982)
[23] B. Hyde, D. Farkas, and M. J. Caturla, Philos. Mag. **85**, 3795 (2005)
[24] J. W. Cahn, Y. Mishin, and A. Suzuki, Philos. Mag. **86**, 25 (2006)
[25] P. M. Derlet and H. Van Swygenhoven, Philos. Mag. A **82**, 1 (2002)
[26] D. Farkas, A. Froseth, and H. Van Swygenhoven, Scr. Mater. **55**,695 (2006)

CHAPTER 6: Tension-compression asymmetry and size effects in nanocrystalline Ni nanowires [1]

We investigate size-effects in nanocrystalline nickel nanowires using molecular dynamics and an EAM potential. Both compressive and tensile deformation tests were performed for nanowires with radii ranging from 5 to 18 nm and a grain size of 10 nm. The wires contained up to four million atoms and were tested using a strain rate of 3.33×10^8 s^{-1}. The results are compared with similar tests for a periodic system, which models a bulk macroscopic sample size of the same nanocrystalline material. The importance of dislocation mediated plasticity decreases as the wire diameter is decreased and is more relevant under compression than under tension. A significant tension-compression asymmetry was observed, which is strongly dependent on the wire size. For the bulk nanocrystalline samples and larger wire radii the flow stresses are higher under compression than under tension. This effect decreases as the wire radius decreases and is reversed for the smallest wires tested. Our results can be explained by the interplay of nano-scale effects in the grain sizes and in the wire radii.

6.1 Introduction

The capabilities of massively parallel computers have allowed large scale atomic level simulations of deformation behavior of materials with features at the nanoscale. As part of this effort, atomistic molecular dynamics (MD) simulations of nanowires have been utilized extensively to study the mechanical behavior and deformation mechanisms of single crystal metallic nanowires . Specifically, MD simulations have been performed to analyze the tensile response and failure mechanisms in metal nanowires

[2-9]. Most of these studies have been performed in single crystal wires of various orientations. Although these studies have been carried out largely under tensile test conditions, Diao et al. found a yield strength tension/compression asymmetry in gold nanowires, with the wires having higher strengths in tension than in compression [10, 11]. The tension-compression asymmetry observed in the single crystal metallic nanowires has been attributed to the effects of the surface stress.

In parallel efforts, the properties of nano-crystalline metals have been another important focus for computational materials research in recent years [12-18]. Simulation work provided understanding for the underlying mechanisms of plastic deformation in these materials and the appearance of particular phenomena at the nano-scale such as the reversal of the Hall–Petch Effect [12]. In these materials, significant tension-compression asymmetry has also been observed, with the strengths being higher under compression than under tension [19,20].

In the present work we explore the issue of tension/compression asymmetry in nanocrystalline nanowires and analyze the deformation mechanisms for nanocrystalline wires of different radii. The wires studied here have nano-scale features both in their grain sizes and in their radii and it is of great interest to study the interplay of the effects introduced by these two length scales present at the nano level.

We begin the paper by discussing the simulation methods used in the work. Next, we present the results of the numerical simulations concentrating on the different deformation modes observed in tension and compression tests. The analysis of our results is divided in two regions. First, we discuss the fundamental mechanisms controlling the deformation in these nanowires for deformations up to 4.5 % (Region 1)

before necking and bulging are observed. Finally, we discuss the necking and bulging behavior observed for deformations in the range from 4.5 to 15% (Region 2).

6.2 Simulation Techniques

The nanocrystalline nanowires were created in two steps. First, a digital cubic sample with a side of 39 nm and 10 nm average size was built using the Voronoi method and random orientations. A grain size of 10 nm was chosen for its hardness properties, since this size lies before the grain sizes that are affected by the Inverse Hall-Petch effect [16]. These grain sizes are near the values that give the maximum hardness as a function of grain size in nanocrystalline materials. This initial cube contained over 6 million atoms and 125 grains.

In the second step, the nickel nanowires were cut from the initial cubic sample with the wire axis parallel to the Z axis of the cube and the axis passing through the center of the cube. This procedure was used to cut seven different nanowire samples with radii from 5 to 18 nm. Because all the wires were cut from the same initial cubic sample the grain boundary structure in the center was the same for all radii. The nanowires created in this way contain up to 4.6 million atoms.

The tensile and compressive simulations performed here use a molecular dynamics (MD) algorithm with the interaction between the atoms modeled using an embedded-atom method (EAM) potential developed by Voter and Chen for nickel [21]. The simulation code used to run the MD mechanical tests was LAMMPS, created by S. Plimpton [21]. An initial relaxation of the initial cubic sample with periodicity in all

directions was performed for 450 ps using a Nose-Hoover thermostat. The nanowires were relaxed using a Nose Hoover thermostat and barostat in the direction of the wire axis. Free surfaces were allowed in the directions perpendicular to the wire axis.

The strain was applied by changing the periodicity distance along the tensile/compressive axis. This periodicity was increased (for tension) or decreased (for compression) from equilibrium to a 15% deviation from the equilibrium value at a rate of 3.33×10^{8} s^{-1}. Although this strain rate is extremely fast compared with those used experimentally, it is typical for MD simulations. For example, in simulations of nanowire deformation Koh and Lee [8] used strain rates up to 10^{10} $s^{-1.}$.

All the nanowire samples were deformed 15% at the strain rate of 3.33×10^{8} s^{-1}. The boundary conditions were kept periodic along the wire axis and free in the other two directions. To simulate the response of a bulk nanocrystalline sample, the initial cube with periodicity in all directions was also deformed at the same strain rate. This procedure allowed the comparison of the behavior of the nanocrystalline nanowires with bulk nanocrystalline configurations.

6.3 Results

6.3.1 Deformation Mechanisms

In recent studies, it has been shown that the deformation mechanism at small grain sizes (<15 nm) is actually an interplay between dislocation mediated plasticity and grain boundary accommodation of plasticity through grain boundary sliding [23]. It was

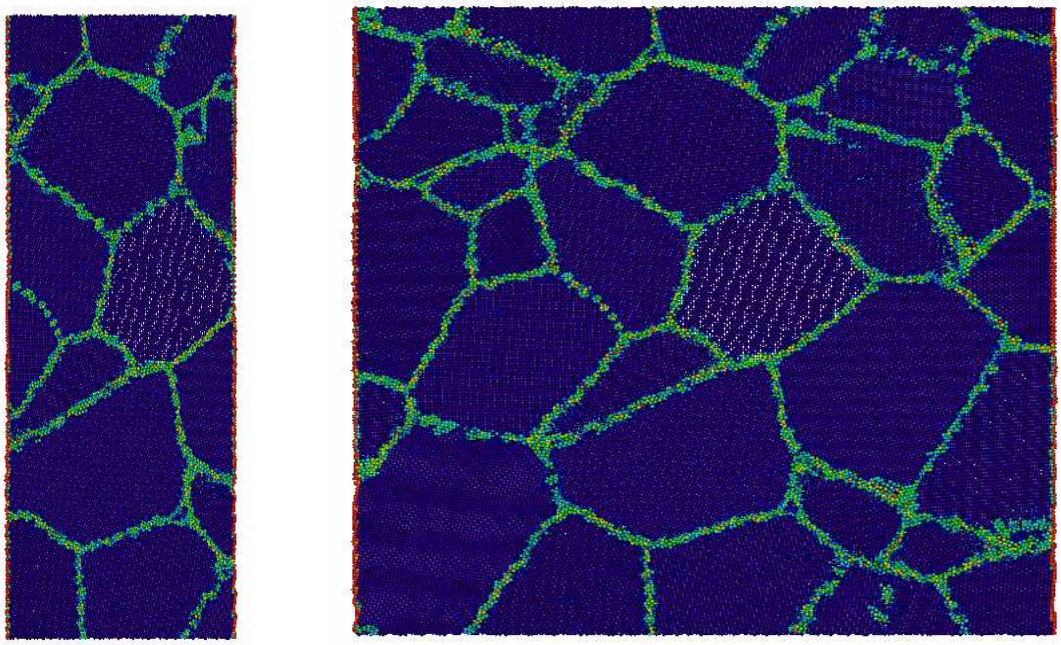

Fig. 6.1 Cross section of the initial structure of the wires of 8 and 18 nm radii. Visualization according to the Centro symmetry parameter.

therefore of interest to find what deformation mechanism was dominating in our studies. To do so we began by looking at cross sections of the nanocrystalline virtual samples.

Figure 6.1 shows a cross section of the initial structure of the wires of 8 and 18 nm radii. The visualization, performed according to the Centro symmetry [24] parameter allows the clear identification of the grain boundaries. Figure 6.2 shows a cross section of the structure of the wires of 8 and 18 nm radii deformed 15% under both tension and compression. The visualization according to the Centro symmetry parameter shows the grain boundaries as well as any dislocation activity resulting from the deformation in these samples.

During the visualization of the tensile samples in Figure 6.2(A,B), it was observed that the dislocation density in the 8 nm is much less than the 18 nm cross section. The difference between these two samples is the surface to volume ratio, indicating that the presence of free surfaces enhances grain boundary sliding, with a lower fraction of the deformation being carried by dislocations,

When Figure 6.2A (tension) and 6.2C (compression) are compared, the results show an increase in the number of dislocations under compression. Therefore the compressive strain is seen to inhibit the deformation of the wires through grain boundary sliding and produces a higher dislocation density.

6.3.2 Stress strain behavior

Figure 6.3 shows the stress-strain behavior under tension (A) and compression (B) for wires of four different radii. The results of the simulation that is periodic in all

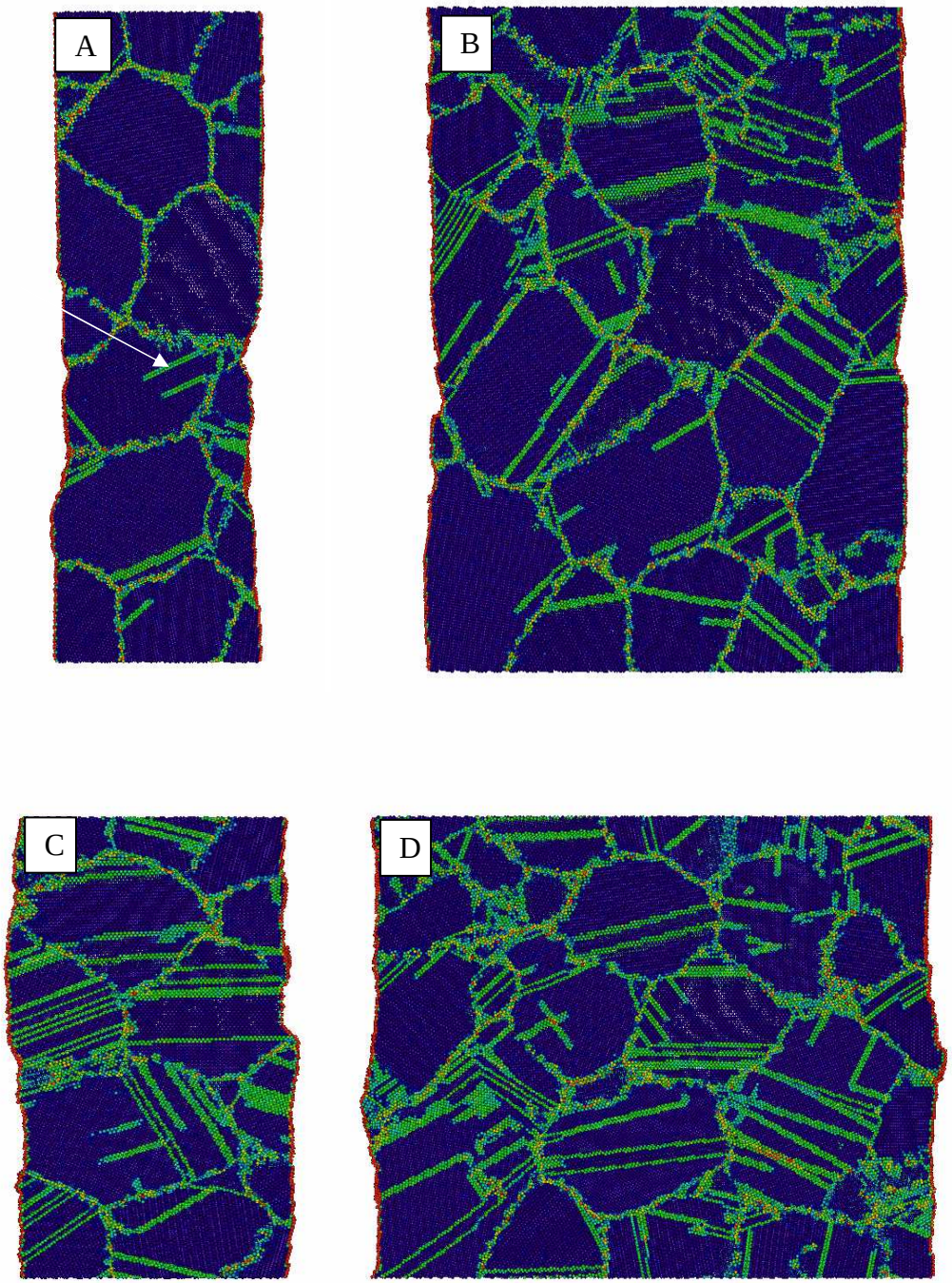

Fig. 6.2 Cross section of the structure of the wires of 8 (A,C) and 18 (B,D) nm radii deformed 15% under both tension (A,B) and compression (C,D). Visualization according to the Centro symmetry parameter. An arrow shows the existence of a dislocation.

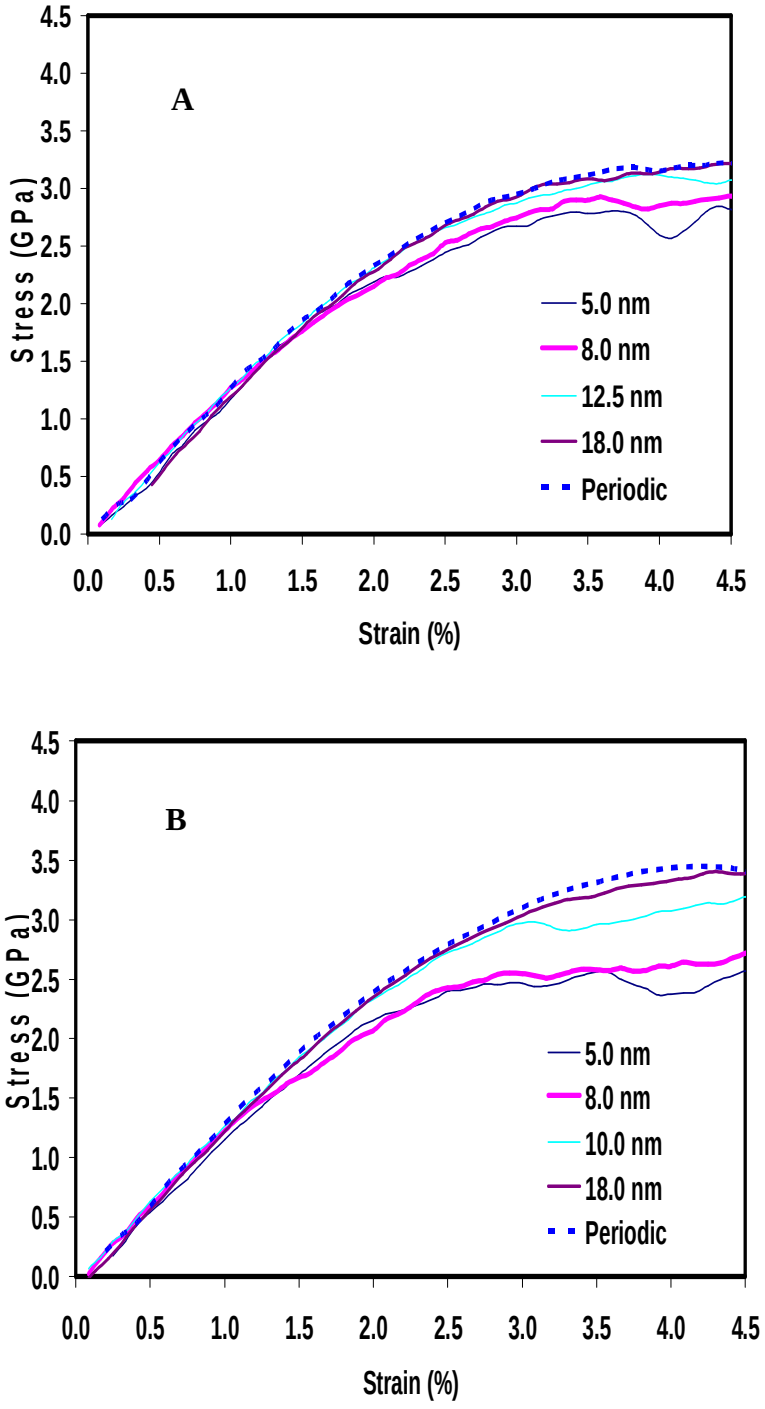

Fig. 6.3 Stress strain behavior under A) tension and B) compression for wires deformed up to 4.5%, before any noticeable necking behavior develops. The results of a periodic simulation, representative of very thick samples are included for comparison

directions, representative of very thick samples are included for comparison. The stress-strain behavior in Region 2, after necking/bulging develops is analyzed in later sections of the paper.

For both, tension and compression tests, the stress-strain curves show that the nanocrystalline nanowires are softer as the wire diameter decreases, with this dependence being more pronounced in the compression tests. This general trend can be interpreted as due to the fact that increased grain boundary sliding is promoted by the presence of the surface, as proposed by Van Swygenhoven et al. [25]. These results present significant tension/compression asymmetries that depend on the wire radius. These effects are addressed below.

Size effects in the tension-compression asymmetry behavior

For the periodic sample we find a tension-compression asymmetry flow stress ratio of 1.06, with the compression flow stress being higher than tension flow stress. This value is in excellent agreement with recent experiments by Schuster et al [26]. This tension-compression asymmetry can be explained by the fact that grain boundary sliding is easier under tension. Grain boundary sliding that is more difficult under compression implies that more dislocation activity is expected under compression for equal deformation levels, in agreement with the observations shown in Figure 6.2.

Figure 6.4 shows the average stress necessary to deform the wires 4.0 to 4.5 % as a function of wire radii, plotted for tension and compression cases. The results of a periodic simulation, representative of very thick samples are shown as dotted lines for comparison. We have chosen the values between 4.0 and 4.5 % deformation for this

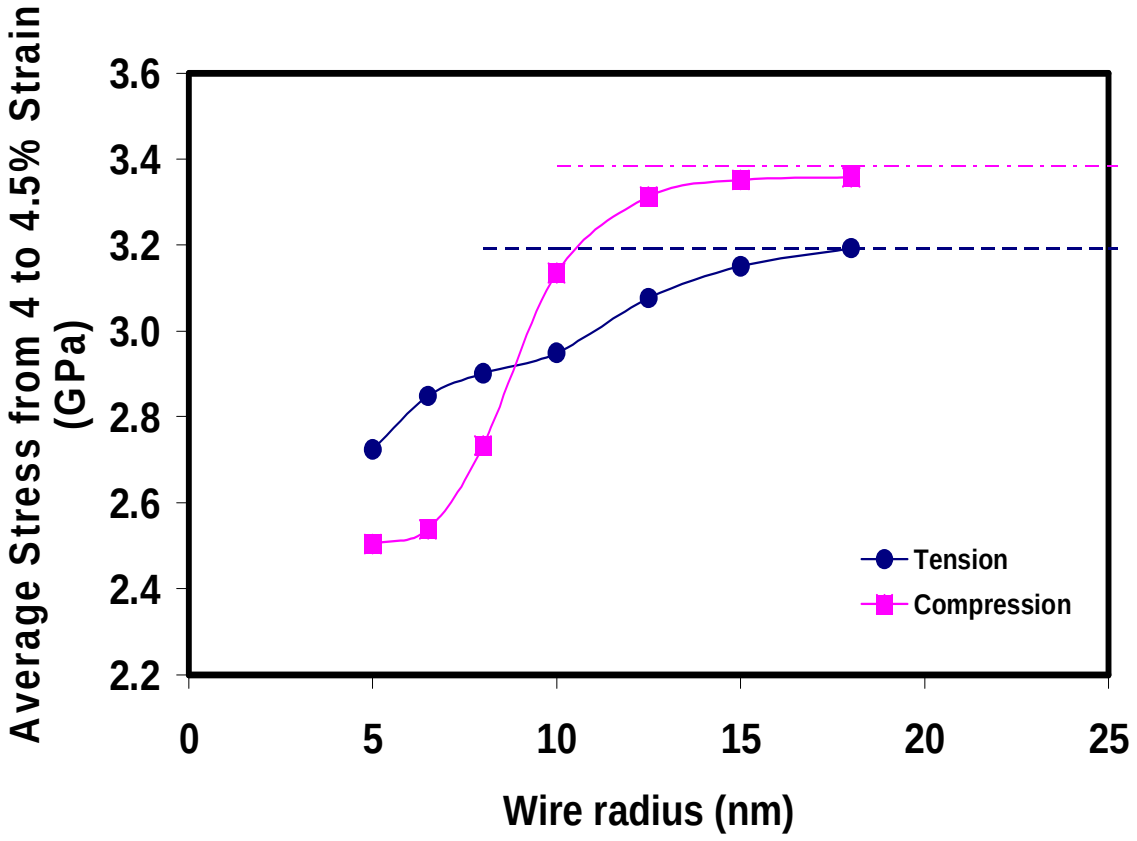

Fig. 6.4 The average stress necessary to deform the wires 4 to 4.5 % as a function of wire radii, plotted both for tension and compression cases. The results of a periodic simulation, representative of very thick samples are shown as dotted lines for comparison.

analysis because it is a deformation value clearly before necking or bulging behavior is initiated in any of the samples. The results in Figure 6.4 indicate a reversal of the tension-compression asymmetry as the wire radius is decreased. For the smallest radii tested, deformation is easier under compression than under tension.

To understand the size dependence of the flow stress under tension and compression, it can be assumed that the resolved shear stress for plastic deformation averaged over the interior of the nanowire has contributions from the external forces as well as an intrinsic compressive stress due to the surface stress [11]. For flow under compression, these two contributions have the same sign and are additive. The smaller the wire diameter, the larger the contribution from the surface-stress-induced intrinsic compressive stress and the smaller the external force necessary to make the nanowire yield. For plastic flow under tension, the two contributions from bulk and surface have opposite signs. The applied external stress must first overcome the surface induced compressive stress before the nanowire can yield under tension. The smaller the nanowire diameter, the larger the relative contribution of the compressive surface stress and the larger the external force is required to make the nanowire flow plastically. This effect implies that for smaller wires a tension-compression asymmetry is expected with flow stresses that are higher under tension. This can explain why single crystal wires present larger flow stresses under tension than under compression and why in our nanocrystalline nanowires of the smaller radii (< 9 nm) we also observe higher flow stresses under tension than under compression.

In addition to the effects of the compressive surface stress on the tension-compression asymmetry, grain boundary sliding is easier under tension than under compression. This effect can be seen in our results for periodic nanocrystalline deformation containing no free surfaces and exhibiting a flow stress under tension that is 6.0% lower than that in compression.

The behavior of nanocrystalline nanowires can then be understood as the interplay of these two tension-compression asymmetries of opposite signs. One asymmetry is due to the surface stress and the other is due to the nanoscale sizes of the grains and the corresponding deformation mechanism of grain boundary sliding. The former dominates overall behavior for the smallest wire diameters whereas the latter dominates for larger wire diameters. For the grain size studied here the cross over in the sign of the tension-compression asymmetry occurs for a wire radius of about 9 nm.

Necking and bulging behavior

In the previous section, we have limited our discussion to deformation levels that do not produce necking or bulging behavior. We have carried out the deformation studies up to 15% deformation and therefore can also study the process of necking under tension and bulging under compression. Figure 6.5 shows the stress strain behavior for the 8 nm radius wire deformed up to 15 %, under both tension and compression. In this small diameter wire the effects of necking can be clearly seen as a decrease in the flow stress as the deformation proceeds, whereas bulging results in an increase of the stress. A line was placed at 4.5% strain in Figure 6.5 to separate the initial deformation (Region I, discussed above) from the influence of the necking and bulging (Region II). These effects are not

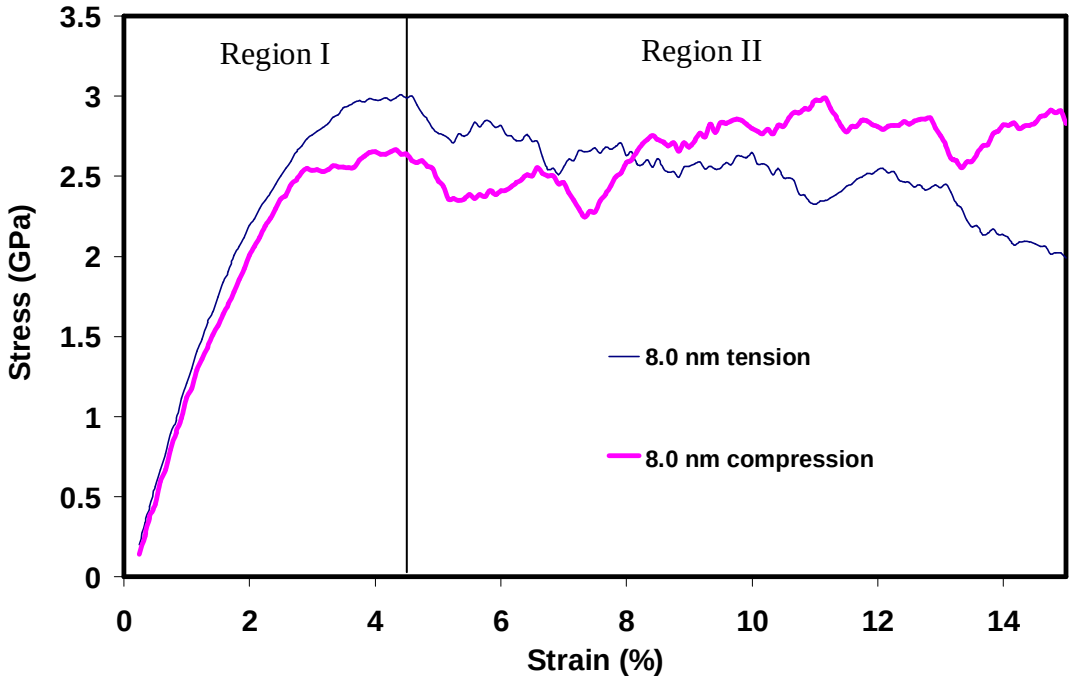

Fig. 6.5 Stress strain behavior for the 8 nm radius wire deformed up to 15 %, under both tension and compression.

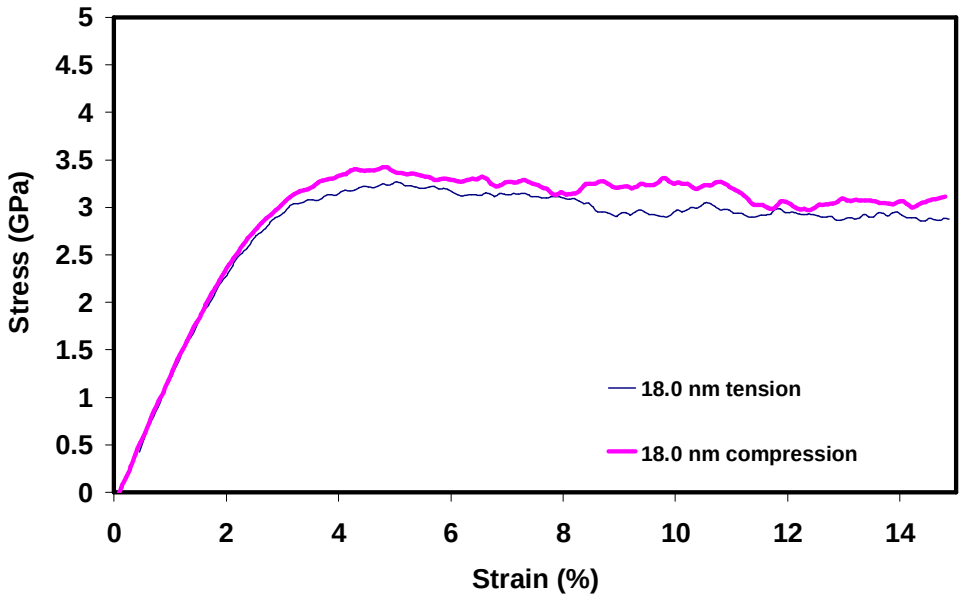

Fig. 6.6 Stress strain behavior for the 18 nm radius wire deformed up to 15 %, under both tension and compression.

significant for the larger diameter wires, as shown in Figure 6.6, where the stress strain behavior is shown for the 18 nm radius wire deformed up to 15 %, under both tension and compression.

To quantify the necking behavior, we have studied the cross sectional area of our samples at different points along the wire axis as the deformation proceeds. Figure 6.7 and 6.8 show the observed changes in cross sectional area at different points along the wire axis for tension (A) and compression (B) tests of wires of 8 and 18 nm radii. The curves represent changes at 3, 6, 9, 12 and 15 % deformation. In Figures 6.7 and 6.8 the changes in cross sectional area are shown as percent changes, with positive changes in the cross sectional area indicating bulging and negative changes indicating necking. It can be seen that at 3% deformation there is no evidence of necking or bulging, but by 6% there is a significant effect, as shown in Figure 6.7. Comparing Figures 6.7 and 6.8, it can be observed that the deformation for thicker wires is distributed evenly along the nanowire (Figure 6.8) whereas Figure 6.7 shows significant localized decreases and increases in cross sectional area, indicating necking and bulging, respectively.

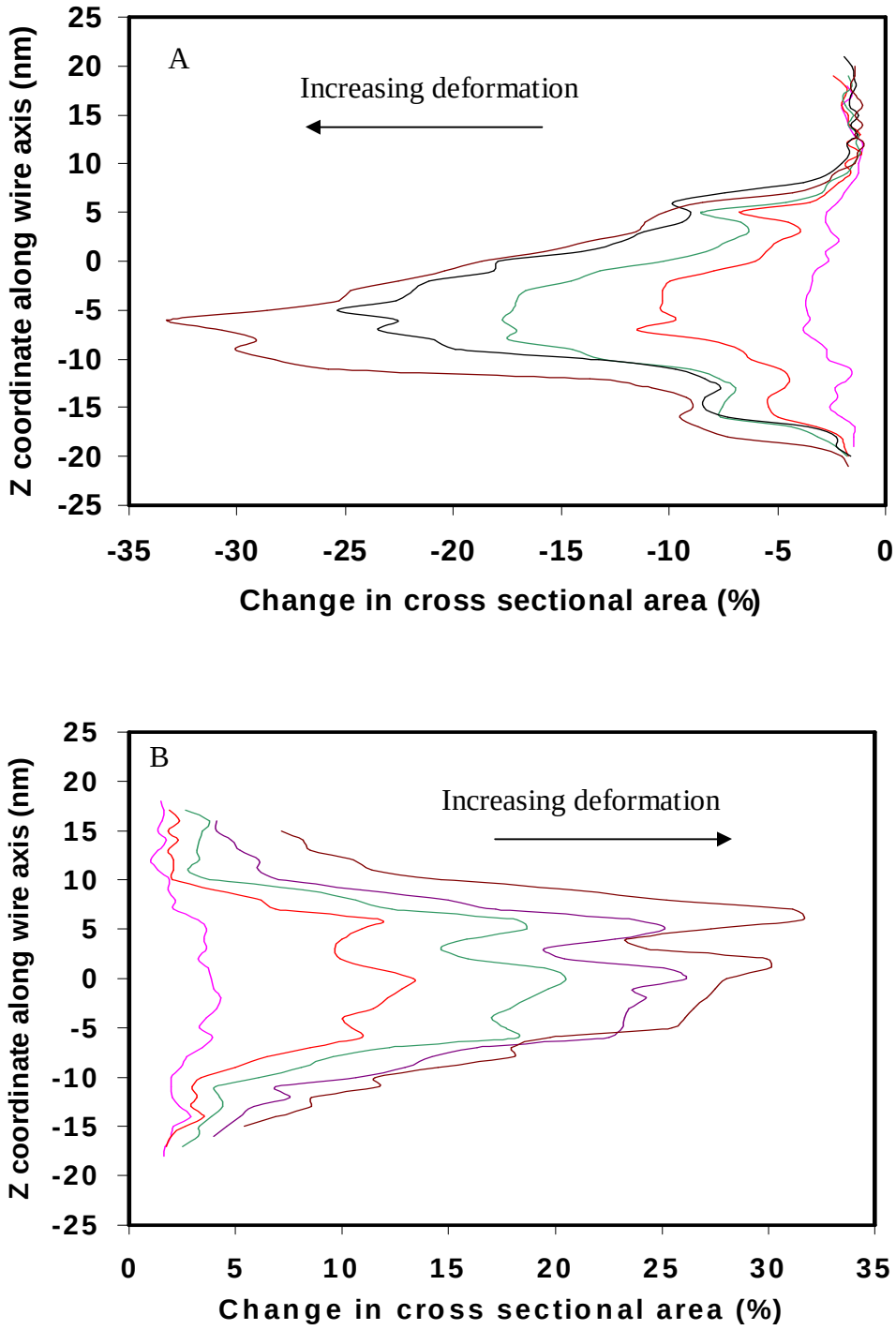

Fig. 6.7 Changes in cross sectional area at different points along the wire axis for A) tension and B) compression tests of wires of 8 nm radius. The curves represent changes at 3, 6, 9, 12 and 15 %.

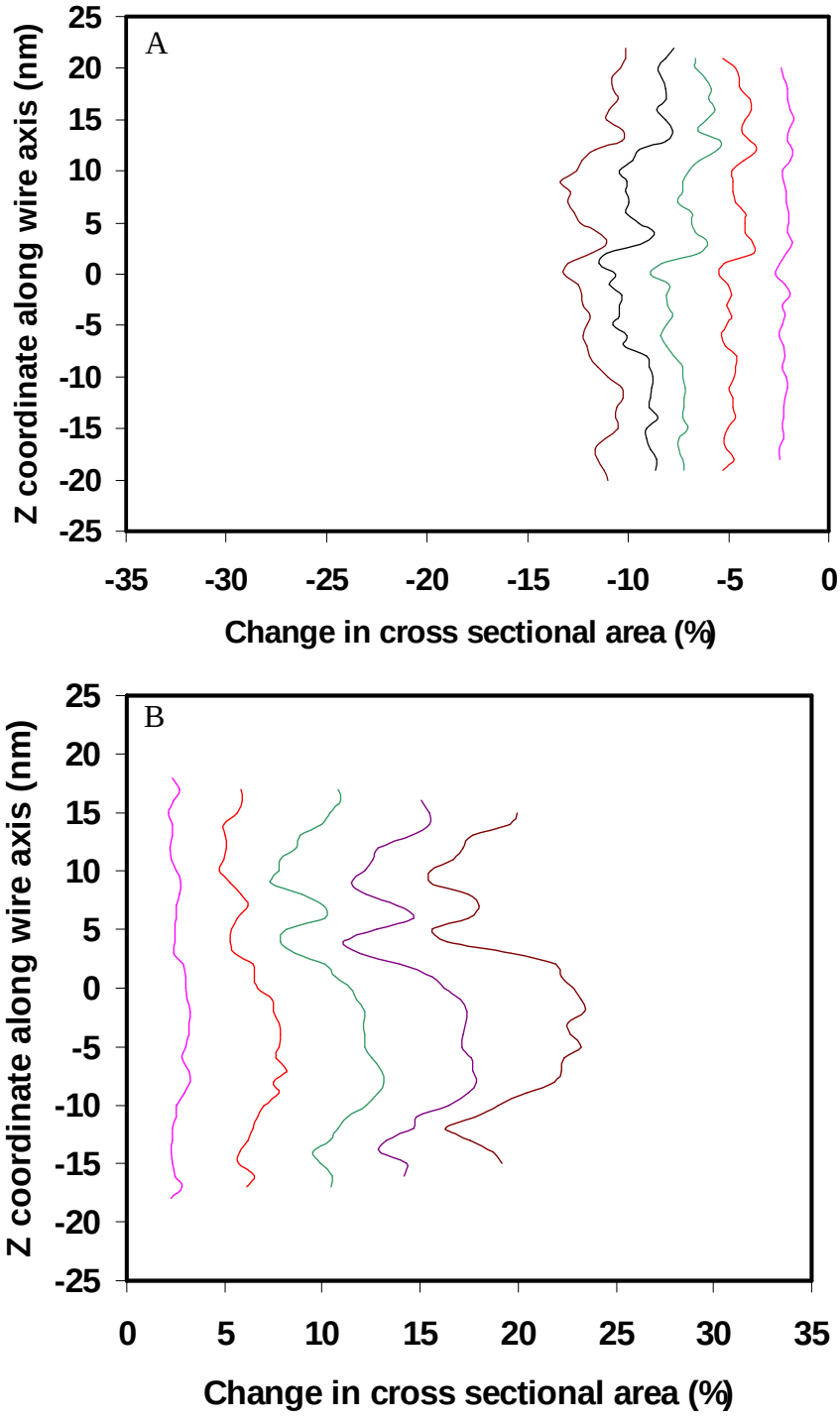

Fig. 6.8 Changes in cross sectional area at different points along the wire axis for A) tension and B) compression tests of wires of 18 nm radius. The curves represent changes at 3, 6, 9, 12 and 15 %.

6.4 Summary and Discussion

This paper presents MD simulations of nickel nanowires subjected to tensile and compressive deformation at a rate of 3.33×10^8 s^{-1}. The nanowire sizes varying from 5 nm to 18 nm radii show evidence of size effects in the stress strain curves as well as in the deformation mechanics. The stress strain curves obtained were analyzed for two regions: Region I below 4.5% strain to avoid interference in the studies of initial deformation of the nanowire and Region II dealing with strains above 4.5%. In this region significant bulging and necking was observed for the smaller radii samples.

To study the deformation mechanisms, the samples were visualized and the dislocations were observed for tensile and compressive deformation. As in previous studies of the plastic deformation of nanocrystalline samples of similar grain sizes, we observed both dislocation activity and grain boundary accommodation of plasticity through grain boundary sliding [23]. The dislocation mediated plasticity is clearly seen in Figure 6.2 and two trends can be identified: 1) there are more dislocations emitted under compression than under tension, and 2) there are more dislocations emitted for the wires of larger radii.

The first observed trend is consistent with the expectation that grain boundary sliding requires larger stresses at high pressures, as shown by recent work studying nanocrystalline metals under shock loading conditions [27]. Under compression, grain boundary sliding is more difficult and a larger fraction of the deformation occurs through dislocation activity.

The second trend points out the effects of the free surfaces on plasticity, indicating that the presence of the surface and there in the surface stress promotes plasticity that is non-dislocation mediated. Indeed, previous studies have shown that there is increased grain boundary sliding in nanocrystalline metallic samples with a free surface [25]. Since the effects of the free surfaces will be dominating at the smallest wire radii, these samples will deform more through grain boundary sliding and there will be fewer dislocations emitted. These two trends give rise to a tension-compression asymmetry where large radii samples result in higher flow stresses for compression than tension. This effect decreases as the wire radius decreases and is actually reversed for wires below 9 nm.

For small diameter samples, the amount of dislocations seen in the compressed and tensile samples can be explained by the ease of grain boundary sliding. In the tensile example, the free surfaces help the grain boundaries slide and thus they present fewer dislocations. As the wire radius increases, the contribution of free surfaces that increased the possibility of grain boundary sliding decreases and therefore increased dislocation activity is seen for thicker tensile samples. For compressed samples the pressure applied makes grain boundary sliding more difficult and thus emitted dislocations contribute more to the overall deformation, which explains the larger number of dislocations in the compressed samples with the same radius as well as the tension-compression asymmetry observed for the thicker wires. For the smaller radii tensile samples, surface-stress-induced compressive stress is large and requires more external stress to yield. Whereas in the small radius compression samples these stresses are additive and a lower external stress is required for yielding. The smallest radii samples tensile samples present a higher flow stress than compressed samples, in a reversal of the sign of the tension-

compression asymmetry of bulk nanocrystalline materials. In the large nanowire cases the amount of surface-stress-induced compressive stress is much lower than the smaller diameters and therefore does not greatly affect the flow stress.

As the deformation proceeds necking or bulging develops in Region II having a significant effect on the flow stresses for samples with the smallest radii. The tensile wire samples that began to neck had a decreased flow stress, whereas the compressed wire samples began to bulge increasing the flow stress as deformation proceeds. For the grain sizes studied here, these effects start to be negligible for wires with a 18 nm radius.

The great interest of nanocrystalline materials is partly due to their strength and hardness caused by the increased grain boundaries and their hindrance of dislocation movement. Grain boundary sliding as a deformation mechanism introduces a limit to the attainable increase in hardness. Furthermore, as we find in the present study, when one introduces high surface to volume ratios, this effect is greatly increased, and the surface induced compressive stress causes a reversal of the sign on the tension/compression asymmetry typical of nano-scaled hardening.

6.5 Acknowledgements

This work was supported by NSF, Materials Theory program. The simulations were performed using System X, Virginia Tech's Supercomputer. We are grateful to Steve Plimpton for providing and maintaining the LAMMPS simulation code.

6.6 References

[1] J. Monk and D. Farkas. Phil Mag. **87**, 14 (2007)
[2] H. Mehrez and S. Ciraci, Phys. Rev. B **56** 12632 (1997)
[3] G.M. Finbow, R.M. LyndenBell and I.R. McDonald, Molecular Physics **92** 705 (1997)
[4] P. Walsh, W. Li, R.K. Kalia, et al., APL **78** 3328 (2001)
[5] H.S. Park and J.A. Zimmerman, Phys. Rev. B **72** 054106 (2003)
[6] K. Gall, J.K. Diao and M.L. Dunn, Nano Letters **4** 2431 (2004)
[7] B. Hyde, H.D. Espinosa and D. Farkas, JOM **62** (2005)
[8] S.J.A. Koh and H.P. Lee, Nanotechnology **17** 3451 (2006)
[9] H.S. Park, K. Gall and J.A. Zimmerman, Journal of the Mechanics and Physics of Solids **54** 1862 (2006)
[10] J.K. Diao, K. Gall and M.L. Dunn, Nano Letters **4** 1863 (2004)
[11] J.K. Diao, K. Gall, M.L. Dunn, and J.A. Zimmerman, Acta Materialia **54** 643 (2006)
[12] J.R. Weertman, D. Farkas, K. Hemker, H. Kung, M. Mayo, R. Mitra, and H. Van Swygenhoven., MRS Bulletin **24** 44 (1999)
[13] J. Schiotz, T. Vegge, F. Tolla, et al. Phys. Rev. B **60** 19711 (1999)
[14] H. Van Swygenhoven, M. Spaczer, A. Caro, and D. Farkas, Physical Review B **60** 22 (1999)
[15] H. Van Swygenhoven and P. M. Derlet, Phys. Rev. B **64** 224105 (2001)
[16] J. Schiotz and K. Jacobsen, Science **301** 1357 (2003)
[17] J. Schiotz, Scripta Mater. **51** 837 (2004)
[18] D. Farkas and W.A. Curtin, Materials Science and Engineering A **412** 316 (2005)
[19] S. Cheng, J.A. Spencer and W.W Milligan, Acta Materialia **51** 4505 (2003)
[20] A.C. Lund, T.G. Nieh and C.A. Schuh, Phys. Rev. B **69** 012101 (2004)
[21] A.F Voter and S. F. Chen, MRS Symposia Proceedings **82** 175 (1987)
[22] S. J. Plimpton, J Comp Phys **117** 1 (1995)
[23] H. Van Swygenhoven, A. Caro and D. Farkas, Materials Science and Engineering A **309-310** 440 (2001)
[24] C.L. Kelchner, S.J. Plimpton and J.C. Hamilton, Phys. Rev. B **58** 119085 (1998)
[25] P.M. Derlet and H. Van Swygenhoven, Philosophical Magazine A **82** 1 (2002)
[26] B.E. Schuster, Q. Wei and H. Zhang, APL **88** 103112 (2006)
[27] E. M. Bringa, A. Caro, Y. M. Wang, M. Victoria, J.M. McNaney, B.A. Remington, R.F. Smith, B.R. Torralva, and H. Van Swygenhoven, Science **309** 1838 (2005)

CHAPTER 7: Meta-Stability of Multi-Twinned Ag Nanorods

Nanoscale rods have been shown to exhibit a multiple twinned structure. The rods grow along a [110] type crystallographic direction and have a pentagonal cross section with five (111) twins connecting the wire center to the corners of the pentagon. Here, we use molecular dynamics simulations with an embedded atom method (EAM) interatomic potential for Ag to compute the ground state energies of the multi-twinned rods and compare with the bulk equilibrium crystal shape, as estimated from a Wulff construction. The excess energy of the non-twinned equilibrium nanorods and the multi-twinned nanorods was obtained as a function of the wire length (L) as well as the cross sectional area (A_{cs}). Various contributions to the total energy, such as twin boundary energy and surface energies, are discussed and included in an analytical model that compares favorably with the simulation results. Our results show that, for infinitely long nanowires with A_{cs}<1000 nm^2, the non-twinned structure is always energetically favorable. However, if the energy of the dipyramidal atomic structure at the nanorod ends is included in the model then the twinned nanorods are stable with respect to the non-twinned rods below a critical aspect ratio ($L/\sqrt{A_{cs}}$).

7.1 Introduction

In recent years, interest in metallic nanowires has grown because of the possible application to nanomechanical and nanoelectronic devices. Metal nanowires exhibit desirable properties such as superior strength [1,2], excellent conductivity [3] and good optical properties [4-6]. The current study focuses on Silver (Ag) nanowires, which have great potential for higher strengths due to the existence of multiple twinned structures [7-

11]. The increased strength in the multi-twinned nanorods has been attributed to the twinned structure's ability to hinder dislocation motion and generate work hardening in the material [11,12].

Multi-Twinned Particulates (MTP), are used as seeds to grow multi-twinned nanorods (MTR) and have been observed for over half a century starting with their discovery by Ino in 1966 [13]. However, the growth mechanisms of MTRs were poorly understood until recent years [14-21]. The MTR which is the focus of the present work is the five-fold "star" nanorod, which, in cross section, consists of five (111) twins connecting the corners of the pentagon to the center of the wire. The unique characteristics of these five-fold twinned nanorods are not seen at the micrometer scale as the rods require extra elastic energy to produce the pentagonal shape. Elastic strain (energy) is generated from the small difference in a twin boundary angle of 70.5° and the 72° angle required to create a pentagon from the five twins. Previously, it has been assumed that the elastic energy resulting from the total 7.5^{o} gap plus the boundary energy from the five twins of the "star" is offset by the lower (100) surface energy of the pentagon, such that the twinned structure becomes energetically stable with respect to the Wulff shape at sufficiently small sizes. Recent studies, however, have questioned this interpretation.

Hofmeister et al. have used X-Ray diffraction to study the atomic distribution of the elastic strain in silver and gold MTRs [9,10]. In addition, Ding et al. [22] has introduced an analytic model using a simple geometry of the nanorods and the excess energy of the system to determine what displacements occurred in the microstructure to accommodate

for the gap [22]. The authors concluded from their analytical model that the elastic, surface and twin boundary energies required for the formation of the pentagon nanorods was sufficiently high such that the MTR's are meta-stable. Thus, it is not fully understood why MTR's are observed experimentally.

Our study incorporates experimental and analytical results for the microstructure of the MTRs and builds upon their findings to discover what factors affect the stability of the MTRs. For this purpose, we used molecular statics and dynamics simulations in combination with an analytical model to study the stability of five-fold "star" nanorods in comparison to the non-twinned "bulk" shape defined by a Wulff construction [23], for various lengths and cross sectional areas. Based on the atomistic results, we designed an analytical model similar to Ding et al. [22] which accounts for the geometry, surface, twin, and elastic energies of the nanorods. The analytical model was developed for the twinned and non-twinned nanorods with and without considering the atomic structure at the rod ends. We use the analytical model and simulation output to describe the relative stability of the rods and find a critical aspect ratio, defined as $L/\sqrt{A_{cs}}$, below which the multi-twinned nanorods are stable.

7.2 Generation of MD Simulation Cells

7.2.1 Wulff Construction for the Non-Twinned Nanorods

The non-twinned bulk equilibrium microstructure was determined using a Wulff construction, as shown in Figure 7.1. The silver nanorods observed in experiments grow along the <110> type axis and therefore, the surfaces included in the Wulff plot are all

perpendicular to the [110] axis. We expect an equilibrium shape similar to the structure produced by Marks [23] in 1984.

For each surface, Table 7.1 shows the angles θ_{hkl} of the surface normal with respect to the $[1\bar{1}0]$ direction, and the corresponding surface energies calculated using the interatomic potential of Voter and Chen [24] selected for our simulation. Based on these values, the Wulff construction indicates that the bulk equilibrium nanostructure has six surfaces made up of four low energy (111) planes and two (001) plane surfaces. The surface energies for the Voter and Chen EAM Potential, γ, are shown in Table 7.1 and the cusps in the Wulff plot correspond to the {111} and {001} type surfaces, are shown in **bold** in Table 7.1. The surface energy of the lowest energy plane {111} is 1.6055 J/m^2 and {001} has a surface energy of 1.7593 J/m^2.

Table 7.1 Surface energies γ (J/m^2) for various orientations observed for the Voter-Chen Potential. Theta angles are taken with respect to [1-10]

[hkl]	θ(hkl) (radians)	Silver $\gamma_{(hkl)}$
[0 0 1]	**1.57**	**1.7593**
[1 -1 5]	1.85	1.8975
[1 -1 4]	1.91	1.9126
[-1 1 3]	2.01	1.9209
[-1 1 2]	2.19	1.8642
[-2 2 -3]	2.33	1.7810
[-3 3 4]	2.39	1.7360
[-4 4 -5]	2.42	1.7090
[-1 1 -1]	**2.53**	**1.6055**
[-4 4 -3]	2.65	1.7281
[-3 3 -2]	2.70	1.7663
[-2 2 -1]	2.80	1.8353
[3 -3 1]	2.91	1.8901
[-5 5 -1]	3.00	1.9190
[-1 1 0]	3.14	1.9342

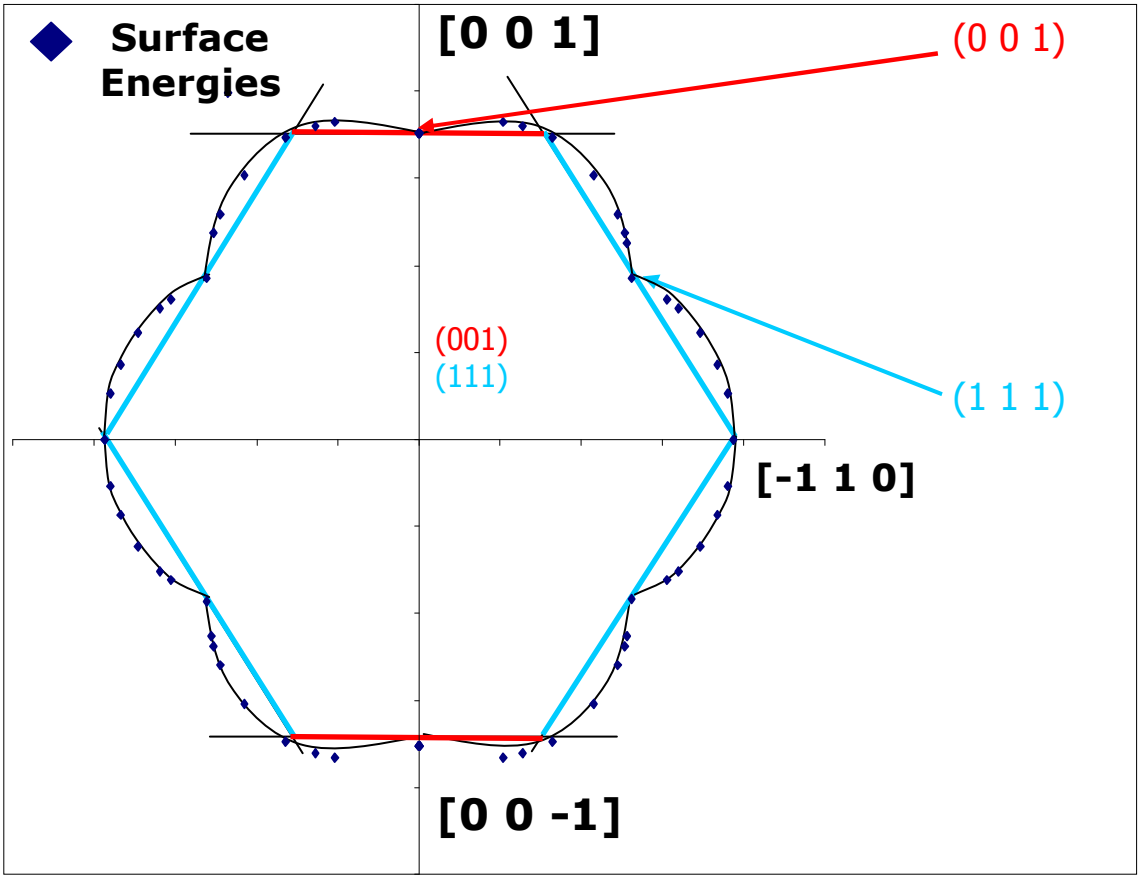

Fig. 7.1. Wulff Construction for Silver Voter-Chen EAM Potential

7.2.2 Multi-Twinned structure

The multi-twinned nanorods observed by Yacaman et al. exhibited a pentagonal shape with five twins in a star formation [11]. A model of the fivefold nanorods is shown in Figure 7.2. As discussed above, there exists a 7.5° gap produced by the difference in the (111) twin boundary angle and the geometric constraint of a pentagon and the mismatch introduces elastic energy in the system. The existence of this elastic strain implies an upper size limit of the MTR. There have been a few hypotheses for how the MTR system distributes the elastic strain in the nanorod to accommodate for the 7.5° [12,20]. To generate the initial nanorod geometry in our studies, we have chosen to strain the atoms along the x-axis as seen in Figure 7.2. Confining the elastic strain in one direction allows us to simplify the equations used to define the strain in the system. The strain is defined as $\frac{b-b_o}{b_o}$, where b_o is the base of the 35.25° triangle and b is the base of the 36° triangle. The relationship between the base of the 35.25° triangle and the 36° triangle is:

$$b = \frac{\tan(36°)}{\tan(35.25°)} b_o \qquad \textbf{Equation 7.1}$$

The atomic displacement of each atom is shown in Figure 7.2 and given by:

$$X = \left[\left(1 - \frac{b_o - \Delta X}{b_o} \right) * (b - b_o) \right] X_o \qquad \textbf{Equation 7.2}$$

where X is the atomic displacement of each atom, ΔX is the distance in the x-axis from the center of the pentagon, and X_o is the initial position of the atom in the x-axis. Note that central atoms (X_c) are located at $X_c = 0$ and $\Delta X = (X_o - X_c) = X_o$. . Equation 7.2

shows that atoms further away from central atoms will have more displacement, those closer to central atoms will have small displacements, generating a ‘stretched’ triangle. The maximum amount an atom will be displaced is $X = b_o$, thus resulting in a distance of (0.028*X).

The ‘stretched’ triangle obtained by this method is then rotated about point A as in Figure 7.2 until the full pentagon is created and all overlapping atoms are removed. The radius can easily be increased to create larger MTR with different cross sectional areas. The cross sections of the twinned and non-twinned nanorods are shown in Figure 7.3.

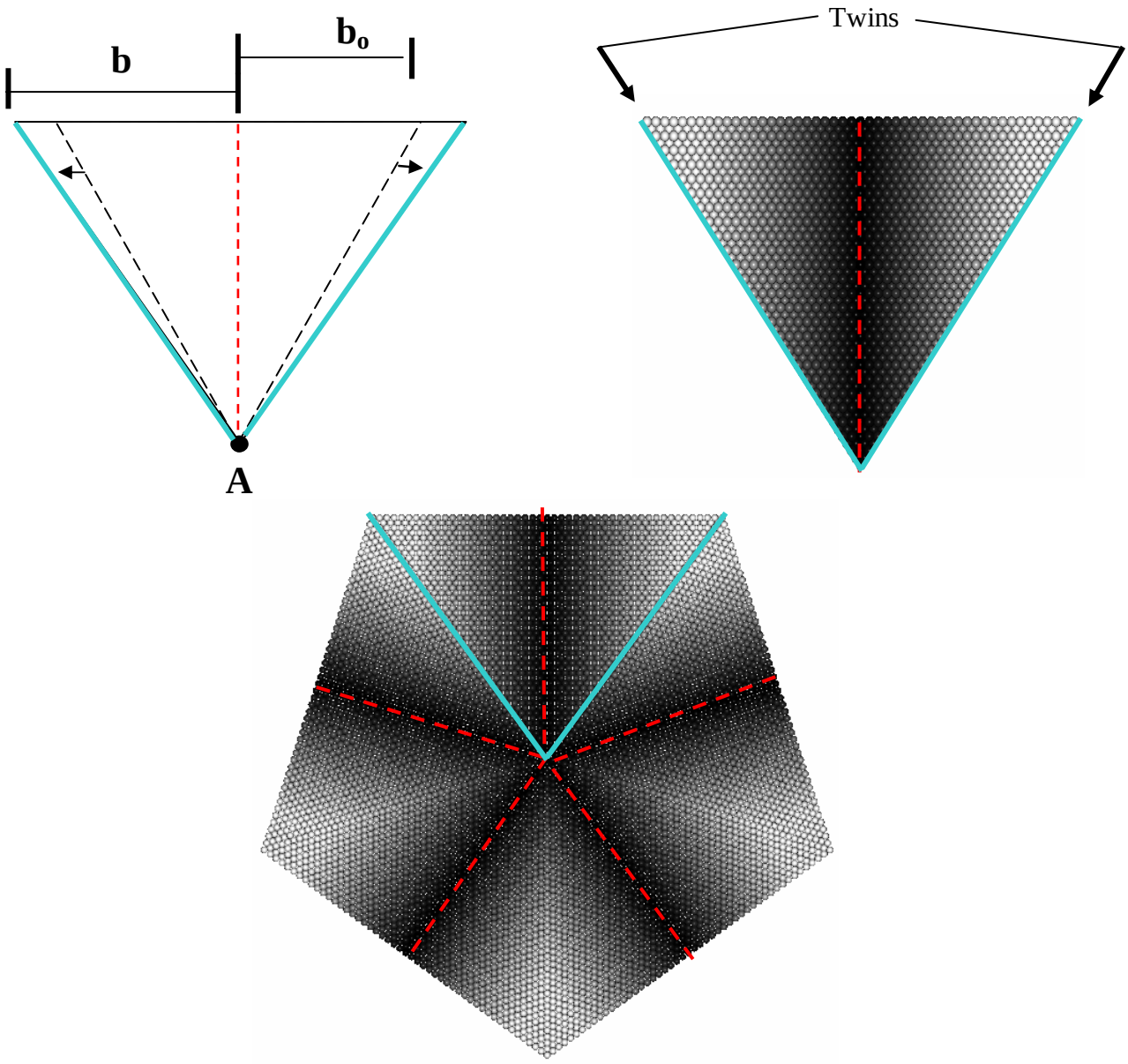

Fig. 7.2 The process for creating the five-twinned nanorod. a) Shows the compensation for the 7.5 degrees. The dashed triangle is the initial triangle, 70.5°. The solid triangle has 72°. The top right shows the displacement of each atom, atoms displaced 0.15 nm are white, atoms displaced 0.0 nm are black. Arrows indicate the twin boundaries. The bottom figure shows the triangle rotated $2\pi/5$ about Point A, this creates a pentagon with displacement coloring. The dashed lines are central atoms with no displacement (red).

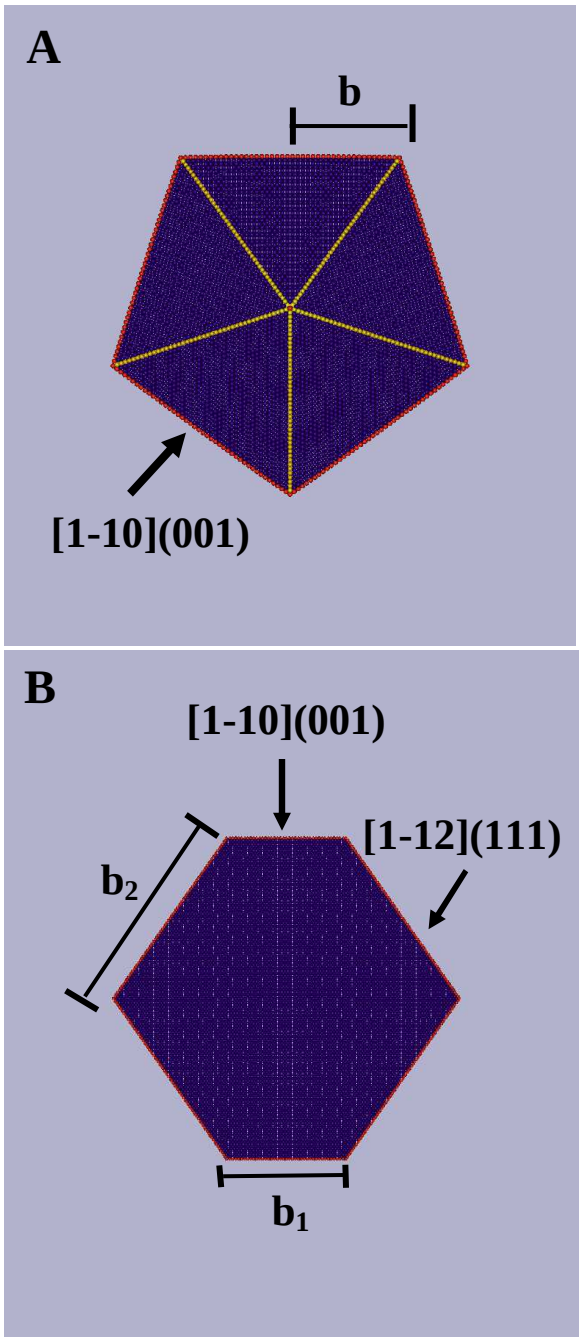

Fig. 7.3 The microstructures for the A) multi-twinned nanorods and B) non-twinned nanorods. Coloring by CSP, gold lines are twin boundaries.

7.3 Simulation Techniquies

The atomic interactions of the virtual Ag samples were governed by a Voter-Chen EAM potential [24] (the Discussion and Conclusions section briefly describes results from two additional Ag EAM potentials). Simulations to find the energy of the nanorod structures were performed using the multi-processor molecular statics and dynamics software LAMMPS created by S. Plimpton [25]. As explained in more detail below the ground state energy of the larger nanorods was determined by first performing dynamics simulations at high temperatures and subsequently cooling the system. For the dynamics runs under NPT conditions, the temperature and pressure were controlled by a Nose-Hoover thermostat and a standard Parinello-Rahman barostat respectively; these conditions allowed atomic movement at the surfaces, and periodic and zero pressure boundaries applied along the nanorod length allowed for stress relaxation due to Poisson contraction. Molecular statics simulations used the conjugate gradient method, which allowed the system to find the minima in the energy functional [26].

A series of MD simulations were run at 1K for 5 ps for each nanorod to allow for relaxation at the surfaces and periodic boundaries. After the molecular dynamics were completed, the system underwent an energy minimization and the total energy of the nanorod was obtained for the minimum configuration. The excess energy for each nanorod was determined by subtracting the ground state energy of the bulk material with the same number of atoms from the atomic energies calculated in the simulations. As expected the higher energy atoms for the MTRs were located at the surface and twins, whereas the non-twinned nanorods contained only high energy surface atoms which

contributed to the excess energy of the system. The excess energy was found for the MTR and the non-twinned nanorods of different cross sections, while the length was kept constant at 3.32 nm (periodic). The cross sectional areas varied from 7.12 nm^2 to 1460 nm^2.

It is important to stress that the surface, twin boundary and elastic energies obtained from molecular statics correspond to the ground state (T=0K). Therefore the conclusions drawn from this study may change slightly at the actual growth temperatures of nanorods. However, if we invoke the reasonable assumption that all the surface and twin boundaries decrease with temperature in approximately the same manner, then the ground state results will provide an accurate description for all growth temperatures.

7.4 Analytical Model of Periodic Nanorods Without Consideration of the Rod Ends

7.4.1 Multi-Twinned nanorods

The equation for the excess energy of the multi-twinned nanorod must take into account the five (100) surfaces, the five twin boundaries, and the elastic energy due to the strain that compensates for the 7.5° gap. We first calculated the cross sectional area as a function of the triangle base length.

$$A_{cs} = 5\frac{b^2}{\tan(\theta_1)} \qquad \textbf{Equation 7.3}$$

A_{cs} is the cross sectional area, b is the base length of the pentagon, and θ_1 = 36° or 0.628 radians. Equation 7.3 is simply the geometric calculation of the area of a pentagon. An analytical representation of the excess energy of the multi-twinned nanorods, Equation 4,

was determined from the surface, twin, and elastic energies and the size dimensions of the rod.

$$\Delta E_{MTR} = \left(\frac{1}{5}\tan(\theta_1)\right)^{1/2}\left(10\gamma_2 + \frac{5\gamma_t}{\sin(\theta_1)}\right)L(A_{cs})^{1/2} + 2U_M LA_{cs} \qquad \textbf{Equation 7.4}$$

where L is length, A_{cs} is cross sectional area, U_M is the elastic energy, γ_2 is the (001) surface energy and γ_t is the twin energy of the system and $\theta_1 = 0.628$. The first energy term in Equation 7.4 identifies the five free surfaces along (001) planes found for the pentagon shape. The surface energy for the (001) plane is given in Table 7.1 as $\gamma_2 = \gamma_{001} = 1.76$ J/m^2. The surface energy is multiplied by the surface area, excluding the periodic ends. The twin boundary energy was found to be $\gamma_t = 0.108$ J/m^2 for the Voter-Chen EAM potential [24] and is multiplied by the cross sectional area and length. The final term is the contribution of the elastic strain in the multi-twinned structures. This elastic term is negligible for very small cross sectional areas and increases in importance as the cross sectional areas increase. In the present analytical model we restrict ourselves to small cross sectional areas and we neglect the elastic energy term. The fact that the elastic energy is indeed negligible for $A_{cs} < 1500$ nm^2 was confirmed by the agreement in the energies given by the atomistic simulation and the analytical model, as shown below. We therefore calculate the excess energy of the multi-twinned nanorods without the elastic energy term as:

$$\Delta E_{MTR} = \left(\frac{1}{5}\tan(\theta_1)\right)^{1/2}\left(5\gamma_2 + \frac{5\gamma_t}{\sin(\theta_1)}\right)L(A_{cs})^{1/2} \qquad \textbf{Equation 7.5(a)}$$

Equation 7.5(a) illustrates the dependence of the energy on the length (L) and the cross sectional area (A_{cs}) with the relationship, L $(A_{cs})^{1/.2}$. A constant K_1 can be defined as:

$$K_1 = \left(\frac{1}{5}\tan(\theta_1)\right)^{1/2}\left(5\gamma_2 + \frac{5\gamma_t}{\sin(\theta_1)}\right) \qquad \textbf{Equation 7.5(b)}$$

such that

$$\Delta E_{MTR} = K_1 L\left(A_{cs}\right)^{1/2} \qquad \textbf{Equation 7.5(c)}$$

where $K_1 = 7.05$ when $\gamma_2 = \gamma_{001} = 1.76$ J/m^2 and $\theta_1 = 0.628$ as defined by the Wulff plot.

7.4.2 Non-Twinned Nanorods

To develop the analytical model for the non-twinned nanorods, we calculated the cross sectional area as a function of the (001) plane length, b_1, and (111) plane length, b_2 (the lengths b_1 and b_2 are shown schematically in Fig. 7.3B). The area is given by:

$$A_{cs} = 2\left|\cos(\theta_3)\right| b_1 b_2 + 2\left|\cos(\theta_3)\sin(\theta_3)\right| b_2^{\,2} \qquad \textbf{Equation 7.6}$$

Equation 7.6 shows the relationship of the cross sectional area, A_{cs}, θ_{111}, and the surface lengths, b_1 and b_2. $\theta_3 = \theta_{111} = 2.53$ radians is given in Table 7.1 and is taken with respect to the $[1\bar{1}0]$ orientation.

The analytical model for the non-twinned nanorods introduces two excess energies from the (001) and (111) surfaces as given in Equations 7.7(a,b). The excess energy for a non-twinned nanorod of length L is:

$$\Delta E_{HEX} = K_2 L A_{cs}^{1/2} \qquad \textbf{Equation 7.7(a)}$$

where a second constant K_2 has been introduced and is defined as:

$$K_2 = \frac{2\gamma_2\left((\cos(\theta_2)+\sin(\theta_3)\tan(\theta_3))\gamma_3 - \sin(\theta_2)\tan(\theta_3)\,\gamma_2\right)+4\gamma_3\left(\frac{\sin(\theta_2)}{\cos(\theta_3)}\gamma_2\right)}{\left(\gamma_2\sin(\theta_2)\left(4\gamma_3\sin(\theta_3)\tan(\theta_3)+4\gamma_3\cos(\theta_3)\right)-2\gamma_2^2\left(\sin(\theta_2)\right)^2\tan(\theta_3)\right)^{1/2}} \qquad \textbf{Equation 7.7(b)}$$

With the values $\theta_2 = \theta_{001} = 1.57$, $\theta_3 = \theta_{111} = 2.53$, and the surface energies found from the Wulff plot $\gamma_2 = \gamma_{001} = 1.7593$, $\gamma_3 = \gamma_{111} = 1.6055$ we obtain $K_2 = 8.15$.

The final relationship between the excess energy of the non-twinned nanorods seen in Equation 7.7(a) exhibits the same, $L\,(A_{cs})^{1/2}$ dependence seen in the multi-twinned nanorods as shown in Equation 7.5(c). When comparing the constants K_1 and K_2 we find that because $K_1 > K_2$, the excess energy of the multi-twinned nanorods will *always* be larger than the non-twinned nanorods. This result of the analytical model can be compared with the simulations of the twinned and non-twinned nanorods as shown in the following section.

7.5 Simulation Results

Atomistic simulations were performed for a series of cross sectional areas and periodic boundary conditions applied along the length of the rod. To find the excess energy of the system we subtracted the energy of the perfect bulk crystal material (-2.85 eV per atom for the VC potential) from the total energy of the structure obtained in the simulation. The excess energy is produced by the higher energy atoms, such as the surface, twin boundary, and elastically strained atoms. The excess energy of the system was found for each simulation run by using the combination of molecular dynamics and conjugate gradient minimization techniques to calculate the atomic energies for each rod.

Molecular statics and dynamics simulations were run for the MTR and non-twinned nanorods with increasing cross sectional areas. The length of the nanorods was kept constant with periodic boundary conditions for the ends. The simulation results are consistent with the analytical models in the dependence on the square root of the cross sectional area, A_{cs}. From the simulation data the excess energies of the multi-twinned nanorods are higher than the non-twinned nanorods for all cross sectional areas, again in agreement with the analytical model. The simulation and model results are summarized in Fig. 7.5 where the excellent agreement is clearly seen.

To ensure the system finds the true global minimum energy in the simulations we annealed the samples for 300 ps just below the melting temperature. The system is then cooled to 1K in 350 ps and finally we take the conjugate gradient. We observed that for small cross sectional areas below 450 nm^2 the structure on the far left of Figure 7.4 is similar to the non-annealed sample shown in Figure 7.3(A). However, when the nanorod area was greater than 450 nm^2 the potential energy caused by the elastic strain of 7.5° was large enough for a Shockley partial dislocation to be emitted, thus relieving the excess strain. As the cross sectional area increased further we observed a larger number of partial dislocations, as shown in the sequence of structures shown in Figure 7.4. We note that the presence of dislocations in the MTR microstructures has also been observed in experimental studies [12,17].

The excess energy was calculated in the same way for the annealed and the non-annealed samples. The results of the simulations are shown in Figure 7.5 including both the annealed and the non-annealed simulation excess energies as a function of cross sectional area.

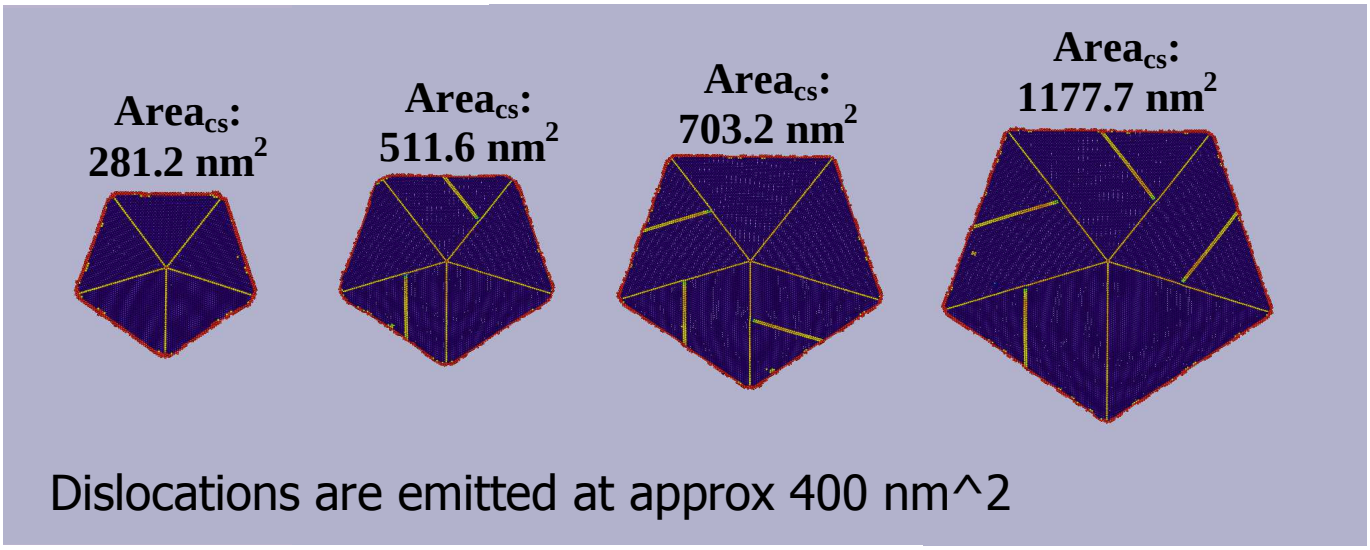

Fig. 7.4 The increase of temperature on the twinned structures shows how the system deals with the increasing elastic strain.

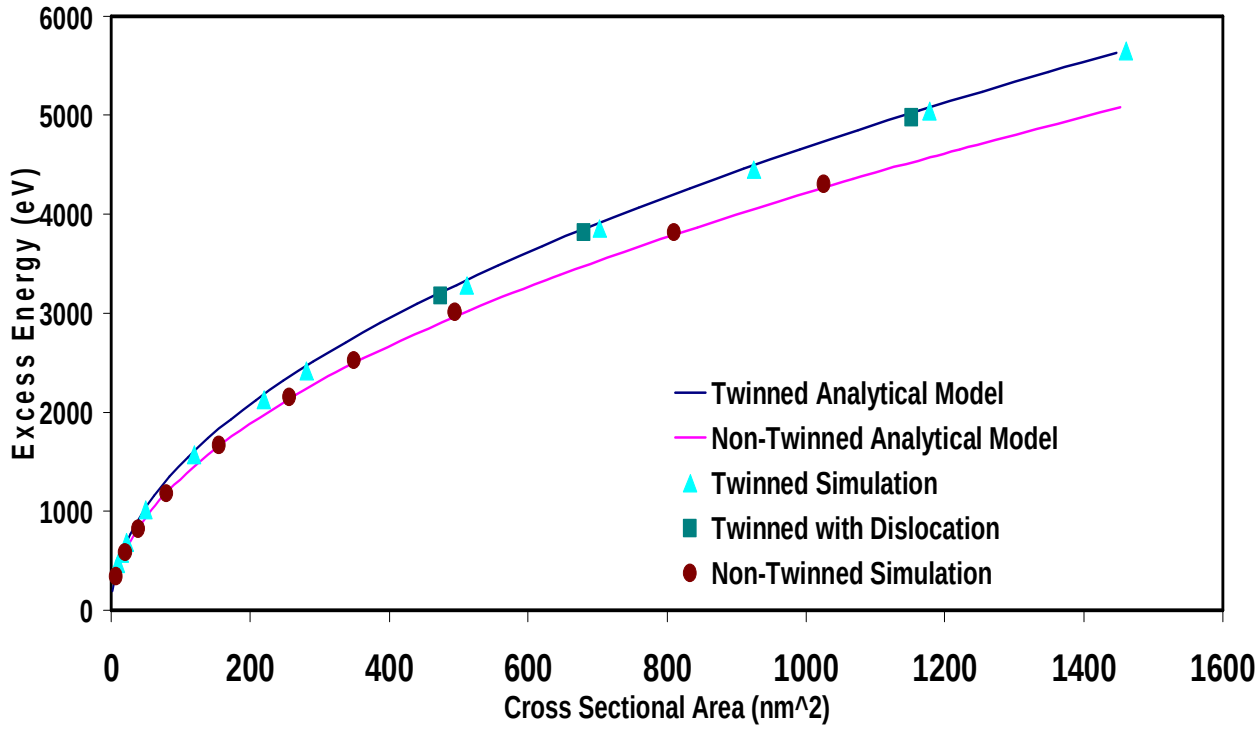

Fig. 7.5 Twinned and non-twinned periodic nanorods excess energy as a function of the cross sectional area. The analytical models are represented by thick lines. The sample's axial length is 3.35 nm.

The results do not exhibit a significant change in the excess energy upon emission of the dislocations for this range of cross sectional areas. We hypothesize that at larger sizes (A_{cs} > 2000 nm^2), the emission of dislocations will most likely be essential to the compensation of the high elastic strain and will play a larger role in the stability of the multi-twinned nanorods. Note that neither the elastic or dislocation excess energy are included in the analytical model. The fact that the analytical model and the simulation results show excellent agreement confirms that the elastic energy term is indeed negligible for these cross sectional areas, since it is by definition included in the simulations. The results of Figure 7.5 confirm that the multi-twinned periodic nanorods, without consideration of the energy due to the atomic structure of the end caps, are not stable at any size or aspect ratio. In the next section, we modify our analytical model to incorporate the energetic contributions of the ends for both the multi-twinned and non-twinned nanorods.

7.6 Analytical Model for the Nanorods Including the Ends

Having established the validity of our analytical model by comparison with the simulation results we extend the analytical framework to incorporate the ends for the MTR and non-twinned structures. No new surface energy values are required in the extended model, all values are the same as those used in the Wulff construction and in the prior analytical model.

To determine the end structures of the multi-twinned nanorods we focused on experimental data. In particular, we choose the structure observed by Yacaman et al [11] using TEM. The structures of the ends were found to be dipyramidal. The dipyramidal

ends are made up of five (111) low energy facets with a 30° slant as shown in Figure 7.6(A) [11]. The analytical model includes the energy of the dipyramidal structure at both ends of the nanowire because the majority of experimental studies show growth along two dipyramidal ends [17,9,12,20].

The ends are also considered for the non-twinned nanorod, which was assumed to be a truncated octahedron, consistent with the Wulff construction. The end structures for the non-twinned nanorod are shown in Figure 7.6(B) and consist of 2 (001) square facets, 2 (111) hexagon facets, and four (111) triangle facets. The modified analytical model accounts for the geometry and surface energy of the nanorod ends.

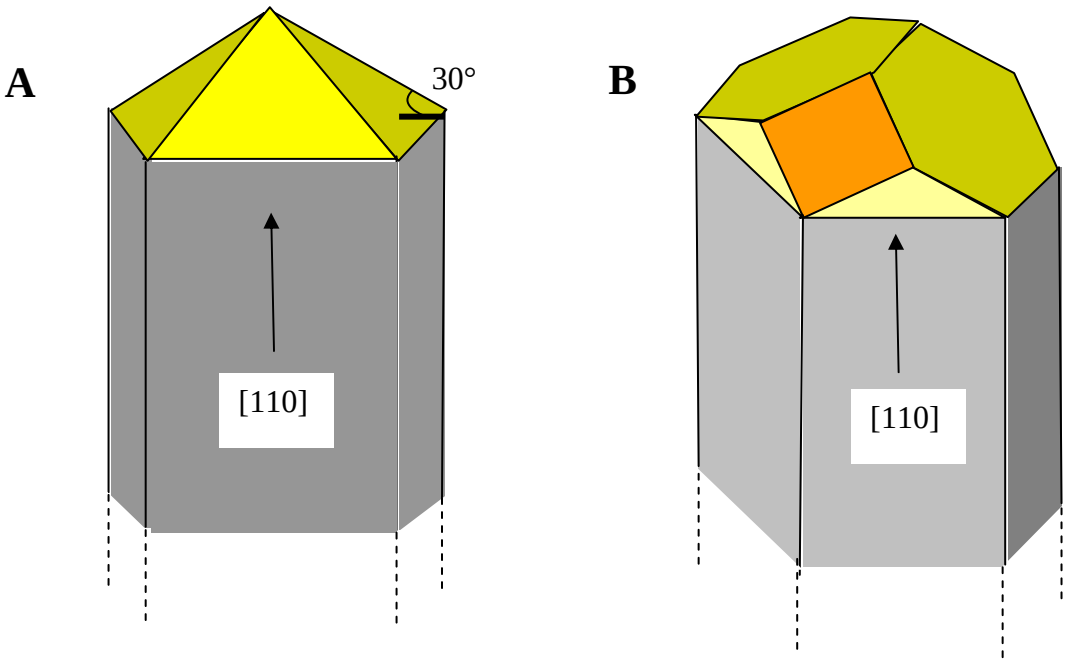

Fig. 7.6 A) Dipyramidal end of the multi-twinned nanorod [11]. B) The non-twinned nanorods with an end. Hexagons and triangles (Yellow) are [111] planes. Squares (Orange) are [001] planes.

The analytical excess energy of the ends of the MTR structures is given as a function of the cross sectional area, A_{cs} as shown:

$$\Delta E_{MTR}^{END} = K_3 A_{cs} \qquad \textbf{Equation 7.8(a)}$$

Where the constant K_3 is be defined as:

$$K_3 = \frac{\gamma_3 \tan(\theta_1)}{\sin(\theta_1)\cos(\theta_4)} \qquad \textbf{Equation 7.8(b)}$$

With $\theta_1 = 0.628$, $\theta_4 = 0.523$, and the surface energy found from the Wulff plot $\gamma_3 = \gamma_{111}$ = 1.6055, we calculate the value $K_3 = 2.29$. Notice the excess energy of the multi-twinned ends are linear with the cross sectional area, A_{cs}.

The excess energy of the ends for the non-twinned nanorods is as follows:

$$\Delta E_{HEX}^{End} = K_4 A_{cs} \qquad \textbf{Equation 7.9(a)}$$

We define K4 as:

$$K_4 = \frac{\gamma_2\gamma_3\sin(\theta_2)}{(\cos(\theta_3))^2}\left(\frac{\tan(\theta_4)+(\cos(\theta_4))^{-3}(\tan(\theta_4))^{-1}-2\cos(\theta_3)(\cos(\theta_4))^{-2}}{2\gamma_3\sin(\theta_3)\tan(\theta_3)+2\gamma_3\cos(\theta_3)-\gamma_2\sin(\theta_2)\tan(\theta_3)}\right)$$

$$+\frac{4\gamma_3^2}{\cos(\theta_3)(\cos(\theta_4))^2}\left(\frac{\cos(\theta_3)+\sin(\theta_3)\tan(\theta_3)}{4\gamma_3\sin(\theta_3)\tan(\theta_3)+4\gamma_3\cos(\theta_3)-2\gamma_2\sin(\theta_2)\tan(\theta_3)}\right)$$

$$+\frac{\gamma_2^2\sin(\theta_2)}{(\cos(\theta_3))^2\cos(\theta_4)}\left(\frac{1}{2\gamma_3\sin(\theta_3)\tan(\theta_3)+2\gamma_3\cos(\theta_3)-\gamma_2\sin(\theta_2)\tan(\theta_3)}\right) \qquad \textbf{Equation 7.9(b)}$$

The surface energies $\gamma_3 = \gamma_{111}$ and $\gamma_2 = \gamma_{001}$ are given in Table 7.1. θ_2 and θ_3 are also defined in Table 7.1 and $\theta_4 = 30°$ is a geometric angle for the non-twinned nanorods, as

seen in experiments. The calculated value for the constant K_4 when $\theta_2 = 1.57$, $\theta_3 = 2.53$, $\theta_4 = 0.523$ with the surface energies equal to $\gamma_2 = \gamma_{001} = 1.7593$ $\gamma_3 = \gamma_{111} = 1.6055$ is found to be $K_4 = 8.15$. A comparison of the constants K_3 and K_4 shows that $K_3 = 2.29$ is significantly lower than $K_4 = 8.15$ which indicates the contribution of the ends strongly favors the twinned nanorods. Figure 7.7 compares the excess energies of the multi-twinned nanorods and non-twinned nanorods with and without ends for a total length of nanorod equal to 3.35nm. When we include the influence of the ends on the system we see a dramatic difference in the energies of the system. The energy contribution of the ends increases linearly with the cross sectional area and, as discussed below, the relative importance of the contribution from the ends to the total energy balance depends on the aspect ratio of the rods.

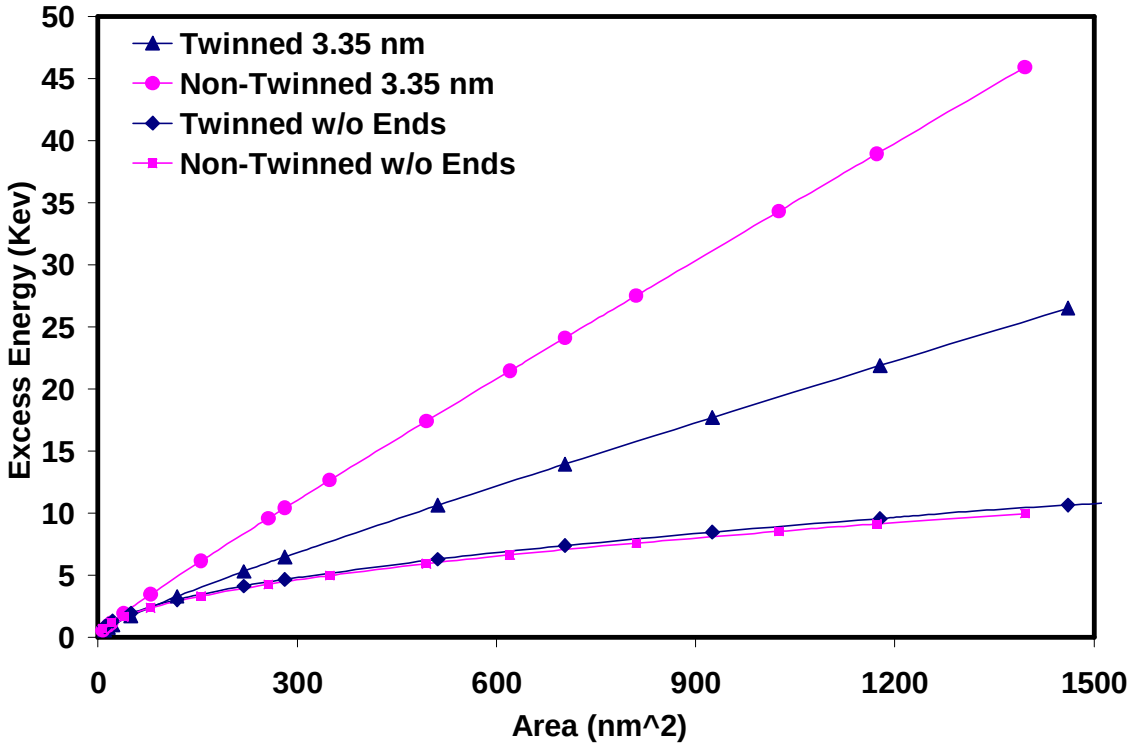

Fig. 7.7 Shows the analytical model with and without the ends. The lengths of the nanorods are 3.35 nm. The data for the nanorods w/o ends are the same as Figure 7.5.

A critical aspect ratio for the stability of the multi-twinned structure can be calculated from the energetic condition, $[\Delta E_{hex} + \Delta E_{hex}(End)] \geq [\Delta E_{MTR} + \Delta E_{MTR}(End)]$. The equation for $\Delta E_{hex}(Tot) = \Delta E_{MTR}(Tot)$ is plotted in Figure 7.8. The energy balance equation for the critical aspect ratio is given as:

$$L = \frac{K_4 - K_3}{K_1 - K_2} A_{cs}^{1/2} \qquad \textbf{Equation 7.10}$$

The critical aspect ratio, C can be defined as the length divided by the square root of the cross sectional area. When the aspect ratio is below the critical value C, the MTRs are stable. The critical aspect ratio can be determined from the constants K_1, K_2, K_3, and K_4 given by Equations 7.5(b), 7.7(b), 7.8(b), and 7.9(b). These in turn depend on the various surface energies and the twin energy. To reiterate, the values found in our studies for the Voter-Chen potential are $K_1 = 7.05$, $K_2 = 5.32$, $K_3 = 2.29$, and $K_4 = 8.15$. The critical aspect ratio is calculated to be $C = (K_4 - K_3)/(K_1 - K_2) = 3.38$. Figure 7.8 shows this condition in terms of a stability map, where length and cross sectional area combinations lying below the curve represent energetically stable MTR configurations.

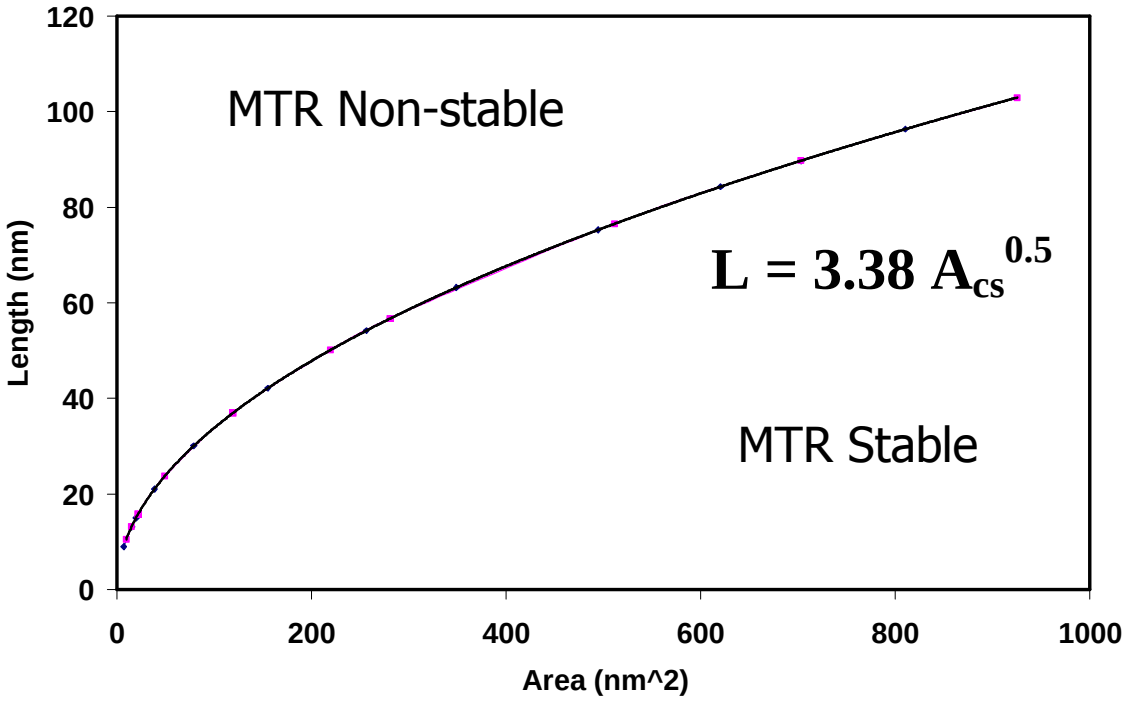

Fig. 7.8 Plotted the relationship between the length and the cross sectional area, when $\Delta E_{MTR} = \Delta E_{HEX.}$

7.7 Discussion and Conclusions

Through a combination of molecular dynamics, molecular statics, and an analytical model we concluded that if the rod ends are not considered, (i.e. periodic, infinite wires) multi-twinned nanorods are not stable at any cross sectional area. There was excellent agreement between the simulations and the analytical model developed, indicating that the model is indeed correct and that the elastic energy, not considered in the analytical model, is negligible for the cross sectional areas studied here ($A_{cs} < 1000$ nm^2). The analytical model was extended to include the ends of the nanorods. When the ends were introduced it was found that the existence of the ends was a major influence in the stability of the multi-twinned nanorods. The energetics of the surfaced energy of the ends strongly favors the multi-twinned structure, leading to a critical aspect ratio below which the MTR structure is stable.

Experientially long nanorods have been produced through a number of growth mechanisms that focus on seed mediated growth [8,12,14]. These long nanorods start as small seeds, with aspect ratios below the critical value. As the rods grow in length and surpass the critical value they become metastable. A transformation of a supercritical long multi-twinned rod to the equilibrium structure given by the Wulff construction would clearly involve a large energy barrier.

The critical aspect ratio of 3.38 obtained in the present work is dependent on the particular values of the various surface energies given by the interatomic potential used here. Using the surface energies from a different interatomic potential, such as the Foiles-Baskes-Daw Ag EAM potential [27] in our analytical model, we obtained a critical aspect ratio of 4.16. Similarly, using the values given by the potential of Jiang-

Min et al. [28] we calculated a critical aspect ratio of 4.45. The experimental critical aspect ratio may vary slightly from these values.

In this study we focused on small cross sectional areas for which the elastic energy may be neglected when considering the overall stability. These are the sizes relevant to the initial stages of growth of the nanorods from seeds, and the relative stability of the rods is entirely controlled by the surface and twin energies. The stability of the MTR for cross sectional areas larger than ≈1000 nm^2 would require a more complex analytical model that incorporated the elastic energy and the presence of dislocations. In our studies we showed that dislocations can begin to form for cross sectional areas above 500 nm^2 although for these sizes their energetic contribution is still negligible when compared to the surface energy effects.

7.8 Acknowledgements

This work was supported by NSF, Materials Theory program and Sandia National Laboratories. The simulations were performed using System X, Virginia Tech's Supercomputer. We are grateful to Steve Plimpton for providing and maintaining the LAMMPS simulation code.

7.9 References

[1] B. Wu, A. Heidelberg, and J. Boland, Nature Materials **4**, 525 (2005)
[2] B. Wu, A. Heidelberg, J.J. Boland, J. Sader, X.Sun, and Y. Li, Nano Letters **6**, 468 (2006)
[3] J.T. Hu, T.W. Odom, and C.M. Leiber, Acc. Chem. Res. **32**, 45 (1999)
[4] Y.Y. Yu, S.S. Chang, C.L. Lee, C.R.C. Wang, Journal of Physical Chemistry B **101**, 6111 (1997)
[5] M.B. Mohamed, V. Volkov, S. Link, M.A. El-Sayed, Chem. Phys. Lett. **317**, 517 (2000)
[6] C.J. Murphy and N.R. Jana, Advanced Materials **14,** 80 (2002)
[7] Z.L. Wang, M.B. Mohammed, S. Link, M.A. El-Sayed, Surace Science Letters **440**, L809 (1999)
[8] M. J. Yacaman, J.A. Ascencio, and G. Canizal, Surface Science **486**, L449 (2001).
[9] H. Hofmeister, S.A. Nepijko, D.N. Ievlev, W. Schulze, and G. Ertl, Journal of Crystal Growth **234,** 773 (2002)
[10] H. Chen, Y. Gao, H. Zhang, L. Liu, H. Yu, H. Tian, S. Xie, and J. Li, J. Phys. Chem B **108**, 120238 (2004)
[11] J. Reyes-Gasga, J.L. Elechiguerra, C. Liu, A. Camacho-Bragado, J.M. Montejano-Carrizales, and M. Jose Yacaman, Journal of Crystal Growth **286**, 162 (2006)
[12] H. Petrova, J. Perez-Juste, Z. Zhang, J. Zhang, T. Kosel, and G.V. Hartland, Journal of Materials Chemistry **16**, 3957 (2006)
[13] S. Ino, J. Phys. Soc. Jpn. **21**, 346 (1966)
[14] Y. Sun and Y. Xia, Science **298**, 2176 (2002)
[15] Y. Sun and Y. Xia, Adv. Mater. **14,** 833 (2002)
[16] Y. Sun, B. Mayers, T. Herricks, and Y. Xia, Nano Letters **3**, 955 (2003).
[17] Y. Gao, P. Jiang, L. Song, L. Liu, X. Yan, Z. Zhou, D. Liu, J. Wang, H. Yuan, Z. Zhang, X. Zhao, X. Dou, W. Zhou, G. Wang, and S. Xie, J. Phys. D: Appl. Phys. **38**, 1061 (2005)
[18] B. Wiley, Y. Sun, and Y. Xia, Langmuir **21**, 8077 (2005)
[19] C. Ni, P.A. Hassan, and E.W. Kaler, Langmuir **21**, 3334 (2005)
[20] J.Q. Hu, Q. Chen, Z.X. Xie, G.B. Han, R.H. Wang, B. Ren, Y. Zhang, Z.L. Yang, and Z.Q. Tian, Advanced Fuctional Materials **14** 183 (2004)
[21] M. Liu and P. Guyot-Sionnest, J. Phys. Chem B **109**, 22192 (2005)
[22] F. Ding, H. Li, J. Wang, W. Shen, and G. Wang, J. Phys: Condens. Matter **14**, 113 (2002)
[23] L.D. Marks, Phil. Mag. A **49**, 81 (1984).
[24] A.F. Voter and S.P. Chen, edited by RW Seigel, JR Weertman and R Sinclair. Mater. Res. Soc. Symp. Proc. **82,** 175 (1978)
[25] S. J. Plimpton, J Comp Phys **117** 1 (1995)
[26] V.V. Bulatov and W. Cai, *Computer Simulations of Dislocations* 1st ed. 2006, Oxford University Press.
[27] S.M. Foiles, M.I. Baskes, and M.S. Daw, Phys. Rev. B **33**, 7983 (1986)
[28] Z. Jiang-Min, M. Fei, and X. Ke-Wei, Chinese Physics **13**, 1082 (2004)